

**NASA
Technical
Paper
2250**

March 1984

Investigation of Trailing- Edge-Flap Spanwise-Blowing Concepts on an Advanced Fighter Configuration

John W. Paulson, Jr.,
P. Frank Quinto,
and Daniel W. Banks

LOAN COPY: RETURN TO
AFWL TECHNICAL LIBRARY
KIRTLAND AFB, N.M. 87117

NASA
TP
2250
c.1



NASA



0068003

**NASA
Technical
Paper
2250**

1984

**Investigation of Trailing-
Edge-Flap Spanwise-Blowing
Concepts on an Advanced
Fighter Configuration**

John W. Paulson, Jr.,
P. Frank Quinto,
and Daniel W. Banks

*Langley Research Center
Hampton, Virginia*



National Aeronautics
and Space Administration

Scientific and Technical
Information Branch

SUMMARY

An investigation was conducted in the Langley 4- by 7-Meter Tunnel to determine the aerodynamic effects of spanwise blowing on the trailing-edge flap of an advanced fighter-aircraft configuration. This investigation encompassed two spanwise-blowing concepts. One was a high mass-flow jet (cascade) located below the wing and just ahead of the trailing-edge flap which was intended to turn the spanwise flow downward with the flap and generate induced lift in a manner similar to that of an externally blown flap. The second was a relatively low mass-flow jet (port) located above the wing just aft of the flap hinge line which was intended to provide spanwise jet flow over the flap in order to maintain attached flow over the highly deflected upper surface to improve flap effectiveness. These spanwise-blowing concepts are quite different from the more conventional leading-edge spanwise blowing used for leading-edge vortex control or enhancement.

A series of tests were conducted with variations in spanwise-blowing vector angle, nozzle exit area, thrust coefficient, and flap deflection in order to determine a superior configuration for each concept. This screening phase of the testing was conducted at a nominal-approach angle of attack from 12° to 16° , and then the superior configurations were tested over a more complete angle-of-attack range from 0° to 20° . Data were obtained at tunnel free-stream dynamic pressures from 20 to 40 lbf/ft² at total ideal thrust coefficients from 0 to 2.

The results of the investigation indicate that the superior configurations for both the port and cascade concepts can produce significant induced-lift increments when the proper vector angle and nozzle exit area are used. However, the superior cascade concept generated greater induced lift at a lower thrust coefficient than did the superior port concept, which was more in keeping with what would be available from engines at takeoff and landing.

INTRODUCTION

There has been an increased interest in short takeoff and landing (STOL) performance for fighter aircraft because of emphasis on potential runway-denial problems and the potential need to operate aircraft out of bomb-damaged airfields where usable runway lengths may be reduced. The Langley Research Center has undertaken a program to help define and develop the technologies required for low-speed flight by emphasizing the STOL operations for fighter aircraft that can take off and land in 1500 ft or less. The overall program includes research on advanced high-lift systems using mechanical flaps, thrust vectoring, thrust-induced effects, methods for obtaining longitudinal trim when using powered lift, and thrust reversing for decreased ground rolls. Portions of this program are complete and have been reported in references 1 to 12.

One of the ongoing efforts is a joint research program involving the National Aeronautics and Space Administration (NASA), the U.S. Air Force Wright Aeronautical Laboratories (AFWAL), and Grumman Aerospace Corporation to develop engine-exhaust nozzles with vectoring and reversing capabilities for advanced STOL fighter aircraft. (See ref. 13.) NASA is supporting this research through low-speed wind-tunnel testing and analysis of powered-lift concepts. A previous study (ref. 14) defined the

basic aerodynamic configuration. During the current study, it was proposed that one method of increasing the lifting capability of a fighter-type wing might be to direct a portion of the engine-exhaust flow in the spanwise direction over or under the trailing-edge flap system. There were data from previous investigations which showed that spanwise blowing on the upper surface of a flap could improve flap effectiveness. (See refs. 15 and 16.) This concept uses blowing over the upper surface of the trailing-edge flap from a low mass-flow spanwise jet in order to maintain attached flow on the upper surface of the highly deflected flap. There were, however, no data to support an alternative approach of blowing in the spanwise direction on the lower surface of the wing and flap system. This concept, shown in figure 1, uses blowing under the wing and trailing-edge flap system from a high mass-flow spanwise jet. The jet would be turned in a streamwise direction by mixing with the free-stream flow and then be turned downward by the flap and shed as a jet sheet to produce induced lift in a manner similar to that of an externally blown flap.

Since the upper-surface spanwise-blowing investigation had involved the F-8 aircraft, which differed significantly from the baseline configuration of reference 14, and there was no information to support the underwing concept, it was proposed that these concepts be evaluated in a wind-tunnel investigation before either idea was incorporated in a major wind-tunnel model. An existing NASA wing-canard fighter model (ref. 1), with a planform similar to that of the configuration of reference 14, was modified to allow for investigations of both the upper- and lower-surface spanwise-blowing concepts (ports and cascades, respectively). The purpose of this investigation was to determine the extent to which either or both concepts might increase the lifting capability for a fighter-type wing and flap system.

Parametric investigations were conducted at typical approach angles of attack (i.e., $\alpha = 12^\circ$ to 16°) for both the port and cascade concepts to determine the effects of spanwise-blowing vector angle, nozzle-exit size, nozzle location, and thrust coefficient on the thrust-induced aerodynamics and to determine the superior configurations of those tested. These superior configurations were defined to be the nozzle which produced the largest increment in induced lift relative to the baseline configurations with primary nozzles alone. These superior configurations were then tested over a complete angle-of-attack range (0° to 20°) with several trailing-edge-flap deflections (0° to 45°) at various thrust coefficients (0 to 2) and primary-nozzle deflections of 45° in order to provide detailed information on the effects of spanwise blowing on the flap system of an advanced fighter wing.

The Langley Research Center would like to acknowledge the contributions of William C. Schnell, James G. Doonan, and Warren H. Davis, Jr., of the Grumman Aerospace Corporation, Bethpage, New York, in supporting the wind-tunnel testing, data reduction, and analysis of the final data.

SYMBOLS

All data have been reduced to coefficient form and are presented in the stability-axis system.

- A aspect ratio, b^2/S
- A_e nozzle exit area, ft^2
- b wing span, ft

C_A	axial-force coefficient, $F_A/q_\infty S$
$C_{A,T}$	static-thrust axial-force coefficient, $[(F_{A,S}/p_a)p_\infty]/q_\infty S$
$C_{A,TR}$	thrust-removed axial-force coefficient, $C_A - C_{A,T}$
C_D	drag coefficient, $C_A \cos \alpha + C_N \sin \alpha$
$C_{D,i}$	induced-drag coefficient, $C_L^2/\pi A e$
$C_{D,TR}$	thrust-removed drag coefficient, $C_{A,TR} \cos \alpha + C_{N,TR} \sin \alpha$
C_L	lift coefficient, $C_N \cos \alpha - C_A \sin \alpha$
$C_{L,TR}$	thrust-removed lift coefficient, $C_{N,TR} \cos \alpha - C_{A,TR} \sin \alpha$
C_m	pitching-moment coefficient, $M_Y/q_\infty S \bar{c}$
$C_{m,T}$	static-thrust pitching-moment coefficient, $[(M_{Y,S}/p_a)p_\infty]/q_\infty S \bar{c}$
$C_{m,TR}$	thrust-removed pitching-moment coefficient, $C_m - C_{m,T}$
C_N	normal-force coefficient, $F_N/q_\infty S$
$C_{N,T}$	static-thrust normal-force coefficient, $[(F_{N,S}/p_a)p_\infty]/q_\infty S$
$C_{N,TR}$	thrust-removed normal-force coefficient, $C_N - C_{N,T}$
C_p	pressure coefficient, $(p - p_\infty)/q_\infty$
C_μ	ideal thrust coefficient for total configuration, subscript indicates thrust coefficient for a particular nozzle (i.e., primary, port, or cascade), $m\dot{V}_j/q_\infty S$
c	local wing chord, ft
c_l	section lift coefficient
\bar{c}	wing mean aerodynamic chord, ft
e	span efficiency factor
F	measured nozzle thrust force, lbf
F_A	axial force, $F_{A,B} - F_{A,PT} - F_{A,FT}$, lbf
F_i	ideal nozzle thrust force, lbf
F_N	normal force, $F_{N,B} - F_{N,PT} - F_{N,FT}$, lbf
M_Y	pitching moment, $M_{Y,B} - M_{Y,PT} - M_{Y,FT}$, ft-lb
\dot{m}	measured nozzle mass-flow rate, slugs/sec
NPR	nozzle pressure ratio, p_t/p_∞

p	surface static pressure, lbf/ft ²
p_a	ambient barometric pressure, lbf/ft ²
p_{plenum}	model plenum pressure, lbf/ft ²
p_t	nozzle total pressure, lbf/ft ²
p_{∞}	free-stream static pressure, lbf/ft ²
q_{∞}	free-stream dynamic pressure, lbf/ft ²
S	wing surface area, ft ²
t	thickness, ft
V_j	ideal jet velocity, ft/sec
x, y	distances along body axes
α	angle of attack, deg
γ	flight-path angle, deg
Δ	difference between thrust-removed and power-off data
δ_f	inboard/outboard-flap deflection, deg (e.g., 45°/26° signifies an inboard-flap deflection of 45° and an outboard-flap deflection of 26°)
δ_{PRI}	primary-nozzle deflection angle, deg
η	nondimensional semispan station, $y/\frac{b}{2}$
Λ	sweep or vector angle, deg

Subscripts:

B	balance measurement
C	cascade
FT	flowing tare
f	flap
i	inboard
LE	leading edge
o	outboard
P	port
PRI	primary nozzle

PT pressure tare
 S static data
 TE trailing edge

Abbreviations:

B.L. buttline, in.
 CD convergent-divergent
 F.S. fuselage station, in.
 MOD modified
 W.L. waterline, in.
 2-D two-dimensional

MODEL DESCRIPTION

In order to conduct an investigation of the effectiveness of spanwise blowing, an existing NASA wing-canard model, very similar to the configuration of reference 14, was modified to accommodate the important design features. A sketch of the NASA model indicating the modifications is shown in figure 2. For this investigation, a small-area canard and underwing nacelles with 2-D/CD vectoring nozzles with $\delta_{PRI} = 0^\circ$ and 45° were added (see fig. 3), and the existing simple trailing-edge flap system was removed and replaced by a slotted flap system. The trailing-edge flap (fig. 4) was split in two sections (inboard and outboard) which could be deflected independently from 0° to 45° with a cove slot opened (fig. 4(b)) or closed. Table I also gives a complete set of model configurations (i.e., nozzle type and flap deflection) investigated during the test. A photograph of the complete set of new and modified parts for the NASA model is shown in figure 5, and pertinent geometric data are presented in table II.

Two sets of spanwise-blowing nozzles were constructed for this model. The first was a port spanwise-blowing nozzle which was designed to blow a relatively low mass-flow jet over the upper surface of the trailing-edge flap system. As shown in the sketch in figure 6 and in the following table, two port locations (A and B), two different nozzle area ratios ($A_{e,P}/A_{e,PRI}$), and three vector angles (Λ_P) were investigated to determine the aerodynamic effects of spanwise blowing through these ports on this configuration. A description of the seven ports is given in table I, and photographs showing the individual ports and the installation of port 7 on the model are shown in figure 7.

$A_{e,P}/A_{e,PRI}$	Type of port nozzle used at angles Λ_P of -		
	30°	45°	60°
0.05	A, B	A	A
.10	B	B	B

The second set of cascade spanwise nozzles for the underwing spanwise-blowing concept were designed to blow a larger mass-flow jet under the trailing-edge flap system. As shown in the sketches in figure 8 and in the following table, a sizable matrix of parametric variables were investigated to determine the effects of cascade spanwise blowing on the aerodynamics of the configuration. It should be noted that

$A_{e,C}/A_{e,PRI}$	Type of cascade nozzle used at angles Λ_C of -		
	-30°	0°	30°
0.20	Basic	Basic	Basic
.30		↓	
.45			Basic
.60	Alternate		Alternate

there were two types of cascades constructed: (1) a flush-mounted basic nozzle (figs. 9(a) and (b)), and (2) a large-area nozzle (fig. 9(c)) which would be representative of an operational system that protruded out from the side of the nacelle (alternate) in an effort to improve flow turning in the nozzle. This alternate nozzle is not really representative of a likely operational nozzle system because of the high drag that would be produced as the nozzle protruded into the free-stream flow. A detailed description of the nine cascades is given in table I, and photographs of some of the individual cascade nozzles and of the installation of cascades 8 and 9 are shown in figure 9.

The air-line system (see fig. 10) in the model was constructed such that the primary nozzles could be operated alone or in combination with either the port or cascade nozzles. In addition, if the primary nozzles were blocked off, either the port or cascade nozzles could be operated by themselves. This was possible since the port nozzles were supplied high-pressure air through a secondary air line from the model plenum where the cascade was simply a nozzle placed in the side of the nacelle which bled or diverted mass flow from the primary nozzles (or the primary air line). Thus, it was actually possible to operate all three nozzles at once, although the only configurations tested were the primary nozzle, the cascade or port nozzles alone, and the primary nozzle in combination with either the cascade or port nozzles.

For these tests, the jet flow was simulated by using high-pressure air provided to the model through a NASA air sting. (See ref. 17). The nozzles were statically calibrated as discussed later in the section entitled "Static-Thrust Calibration." Force and moment data and angle of attack were measured by using an internally mounted six-component strain-gage balance and an internally mounted attitude indicator, respectively.

Other model instrumentation included pressure transducers to measure nozzle and internal piping pressures in order to determine nozzle pressure ratios and mass flows during both static and wind-on power-on testing. Wing-surface static pressures (see fig. 11 for position of static taps) were measured on internally mounted scanning valves.

Transition strips of No. 80 carborundum grit were placed on all lifting surfaces as well as on the model nose. The canard was installed at 0° incidence relative to the fuselage waterlines for all testing.

TEST CONDITIONS

The test was conducted in the Langley 4- by 7-Meter Tunnel in two basic phases: (1) a screening phase in which port and cascade parametrics were investigated to determine the superior port and cascade configuration, and (2) a detailed study of the superior configurations. During the first phase, the angle-of-attack range was limited to a nominal-approach condition of 12° to 16° over a tunnel dynamic-pressure range from 20 to 40 lbf/ft² to investigate thrust coefficients from 0 to 2 for the main nozzles, from 0 to 0.8 for the cascades, and from 0 to 0.2 for the ports. During the second phase, the angle-of-attack range was expanded to 0° to 20° while dynamic-pressure and thrust-coefficient ranges similar to the screening-phase conditions were maintained.

STATIC-THRUST CALIBRATION

Previous to the static-thrust calibration, the air-line/balance combination was calibrated in order to determine the effects of bridging the balance with the air line. These effects are then included in the balance-interaction equations.

During the static calibration, two tares or corrections were measured which were removed from the data under power-on conditions. The first is a sting pressure tare due to pressurizing the air-supply system, and the second is a flowing tare due to the mass passing through the air-supply system under power-on conditions. The pressure tare is caused by the coil in the air line expanding under pressure and pushing on the balance. These pressure tares are presented in figure 12 as a function of model plenum pressure. Thus, when testing with power on, the correction to the pressurized air line could be removed since model plenum pressure is known.

The flowing tare appears to be caused by the momentum of the air flowing to the model, and a normal procedure for measuring the tare is to use a calibrated axisymmetric nozzle and compare the predicted and measured output; any difference is usually defined to be a momentum or flowing tare which is then used as a correction to the data. However, in the Langley 4- by 7-Meter Tunnel, the magnitude of this error is such that it is difficult to determine whether the error is, in fact, caused by the mass flow through the air system or by the possible uncertainties in the known thrust due to installation of the calibrated nozzle on the rectangular flow tubes used on this model. In this test, since the primary nozzles were rectangular 2-D/CD nozzles (see fig. 3), it was felt that the nozzle performance could be accurately predicted. Therefore, any differences between the predicted and measured nozzle output, after removal of the pressure tare, were attributed to a flowing-tare correction. Examples of predicted and measured normal and axial force for the 0° primary nozzle are shown in figures 13(a) and (b), respectively. These differences were felt to be repeatable and significant enough to be included as a correction to the power-on data. As just mentioned, since it was felt that the performance of these nozzles could be accurately predicted, the flowing-tare corrections as a function of the mass

flow through the system are shown in figure 14. These corrections, along with the sting pressure-tare correction, were removed from the power-on, wind-on data as follows:

$$C_A = (F_{A,B} - F_{A,PT} - F_{A,FT})/q_\infty S \quad (1)$$

$$C_N = (F_{N,B} - F_{N,PT} - F_{N,FT})/q_\infty S \quad (2)$$

$$C_m = (M_{Y,B} - M_{Y,PT} - M_{Y,FT})/q_\infty S \quad (3)$$

Each nozzle was statically calibrated to determine the direct-thrust force and moment components as a function of nozzle pressure ratio. These data (e.g., see fig. 15) were used to remove the direct-thrust forces and moments from the wind-on, power-on data obtained in the wind tunnel. The following outline indicates the exact procedure:

- (1) The static-thrust force and moment components ($F_{A,S}$, $F_{N,S}$, and $M_{Y,S}$) were divided by ambient barometric pressure p_a and were curve fit as a function of nozzle pressure ratio NPR.
- (2) During the wind-on, power-on testing at a given NPR, the static direct-thrust force and moment components were obtained from the curve-fit static data, and the wind-on force and moment coefficients were then calculated by scaling the static components to the tunnel static-pressure conditions by the following equations:

$$C_{A,T} = \left(\frac{F_{A,S}}{p_a} \frac{p_t}{p_\infty} p_\infty \right) / q_\infty S \quad (4)$$

$$C_{N,T} = \left(\frac{F_{N,S}}{p_a} \frac{p_t}{p_\infty} p_\infty \right) / q_\infty S \quad (5)$$

$$C_{m,T} = \left(\frac{M_{Y,S}}{p_a} \frac{p_t}{p_\infty} p_\infty \right) / q_\infty S \quad (6)$$

- (3) The components of direct-thrust force and moment coefficients could then be removed from the wind-on, power-on data to obtain thrust-removed coefficients as follows:

$$C_{A,TR} = C_A - C_{A,T} \quad (7)$$

$$C_{N,TR} = C_N - C_{N,T} \quad (8)$$

$$C_{m,TR} = C_m - C_{m,T} \quad (9)$$

DISCUSSION OF RESULTS

BASIC CONFIGURATION

The longitudinal aerodynamics of the basic configuration (i.e., without any spanwise blowing) with various flap and primary-nozzle deflections and thrust coefficients are presented in figures 16 and 17. The induced aerodynamics for these configurations are presented in figures 18 and 19.

As expected, the effect of flap deflections from 0° to 26° (see fig. 16) was to increase lift, generate large nose-down pitching moments, and increase minimum drag. Flap effectiveness $\partial C_L / \partial \delta_f$ (at $\delta_f = 0^\circ$ to 26°) diminished from about 0.01 at low angles of attack to 0.005 at the higher angles of attack. Very little increase in lift is indicated when δ_f is increased from 26° to 45° because of the difficulty in maintaining attached flow at high flap deflections. As discussed in a later section of this report, both spanwise blowing and a slotted flap were used on this configuration in an effort to obtain better flap effectiveness by maintaining attached flow at $\delta_f = 45^\circ$. There is essentially no difference in flap effectiveness for primary-nozzle deflections of $\delta_{PRI} = 0^\circ$ or 45° . However, there is a small positive increment in C_L and C_D and a corresponding small negative increment in C_m due to the primary nozzle itself. This was expected since the external lines of the primary nozzle, when deflected 45° , act like a small inboard-flap element. (See fig. 3.)

The effect of power on the overall longitudinal aerodynamics (fig. 17) primarily reflects the addition of the vector components of the primary-nozzle thrust with essentially zero induced effects when $\delta_{PRI} = 0^\circ$ (fig. 18) and small induced effects (i.e., $\Delta C_{L,TR} \approx 0.1$) when $\delta_{PRI} = 45^\circ$. The effect of flap deflections on the induced aerodynamics (fig. 19) are small, particularly at flap deflections greater than $26^\circ/26^\circ$ (inboard/outboard). This indicates that the exhaust from the primary nozzle, located aft of the flap trailing edge, is unable to entrain flow over the flap system to improve flap effectiveness at the higher flap deflections. This can be seen in the wing pressure distributions (fig. 20) for several flap deflections. There are only slight changes in the pressure distribution between $C_{\mu, PRI} = 0$ and 0.93 when $\delta_f = 0^\circ/0^\circ$ and $\delta_{PRI} = 45^\circ$, thus indicating that the primary-nozzle flow has little effect on the rest of the configuration. When $\delta_f = 26^\circ/0^\circ$, the primary-nozzle flow does induce a reduced pressure on the inboard flap and on the wing leading edge at a station η of 0.42 (center of the inboard flap), thus indicating some entrainment over this flap element. The presence of these reduced pressures at $\eta = 0.42$ are, of course, felt at all points in a subsonic flow field as indicated by the slightly reduced pressures at all other stations on the wing. There are rather minor differences in the pressure distributions between $\delta_f = 26^\circ/0^\circ$ and higher flap deflections (i.e., $\delta_f = 26^\circ/26^\circ$, $45^\circ/26^\circ$, and $45^\circ/45^\circ$), which indicate that the primary-nozzle flow entrainment is insufficient either to affect the outboard-flap element or to improve flap effectiveness at flap deflections equal to 45° .

SELECTION OF SUPERIOR CASCADE AND PORT CONFIGURATIONS

The induced aerodynamics obtained for all cascade and port configurations with the primary nozzles deflected 45° and at an angle of attack of 14° are presented in figures 21 and 22, respectively. These data, representing the nominal-approach angle of attack of 14° for the fighter configuration under study, were the basis for the screening phase of the wind-tunnel test where the superior cascade and port configu-

rations were defined. The discussion of this selection process is given in the following sections of this report.

Cascade Configuration

In order to choose the superior cascade configuration, the effects of cascade-nozzle vector angle and exit area on the induced aerodynamics were examined to determine if one or more cascades would prove to be superior to the other configurations. In general, the definition of "superior" was taken to be that configuration which produced the highest level of thrust-induced lift $\Delta C_{L,TR}$ at a thrust coefficient representative of military-power settings (the maximum nonafterburning power settings).

Effect of cascade-nozzle vector angle.— The effect of the cascade-nozzle vector angle on the induced aerodynamics is presented in figure 23 for three cascade-nozzle exit areas. It can readily be seen that the cascades with $\Lambda_C = 30^\circ$ are the superior configurations since the cascades with $\Lambda_C = -30^\circ$ and 0° produced lift losses rather than lift increases. It should be noted that the cascades with $\Lambda_C = 30^\circ$ produced nose-down pitching moments indicative of the increased aft loading generated when the spanwise exhaust is turned by the trailing-edge flap system. The increases seen in $\Delta C_{D,TR}$ are of the same order of magnitude as would be expected from the increases in induced drag ($C_{D,i}$) generated by increasing lift coefficient. Therefore, from the data of figure 23, it appears that the superior cascade configurations are those with $\Lambda_C = 30^\circ$.

Effect of cascade-nozzle exit area.— For $\Lambda_C = 30^\circ$, the effect of cascade-nozzle exit area on the induced aerodynamics is presented in figure 24. Here, the size of the spanwise jet is varied at the superior-cascade-nozzle vector angle at two flap deflections, $\delta_f = 45^\circ/26^\circ$ and $45^\circ/45^\circ$. The data show that when $\delta_f = 45^\circ/26^\circ$, the thrust-induced lift increment $\Delta C_{L,TR}$ is greatest when the nozzle exit area is largest. Thus, it would seem that the cascade with $A_C/A_{PRI} = 0.6$ (cascade 9) would be selected as superior. However, when $\delta_f = 45^\circ/45^\circ$, this trend is not as well-defined. These data indicate that although the cascade with $A_{e,C}/A_{e,PRI} = 0.45$ (cascade 6) has a slightly higher maximum $\Delta C_{L,TR}$, cascade 9 has a greater useful $C_{u,C}$ range. That is, the drop-off in $\Delta C_{L,TR}$ seen at higher $C_{u,C}$ is not as rapid with cascade 9 as with cascade 6 when $\delta_f = 45^\circ/45^\circ$. Even the smallest cascade (cascade 3) with $A_{e,C}/A_{e,PRI} = 0.2$ was not clearly inferior to cascades 6 and 9 since the maximum $\Delta C_{L,TR}$ generated by cascade 3 was also greater than 0.4.

It appeared that another approach was necessary in order to choose the superior cascade. Comparisons of the thrust-removed lift at a value of C_u such that the configuration had $C_D = 0$ (i.e., unaccelerated flight) in figure 25 showed that only cascade 3 could clearly be eliminated. It was decided that both cascades 6 and 9 would be carried forward as superior configurations for detailed investigations.

Port Configurations

In order to choose a superior port configuration, the effects of port-nozzle location, vector angle, and exit area on thrust-induced aerodynamics were examined in a manner similar to the cascade-selection process.

Effect of port-nozzle location.— The effect of port-nozzle location on the induced longitudinal aerodynamics is presented in figure 26. It can be seen that

when $A_{e,p}/A_{e,PRI} = 0.05$ and $\Lambda_p = 30^\circ$, location B (the more aft location as shown in fig. 6) produced a greater increment in $\Delta C_{L,TR}$. The nose-down increments in $\Delta C_{m,TR}$ correspond to the aft loading expected when the effectiveness of the trailing-edge flap system is improved by the upper-surface spanwise jet. The $\Delta C_{D,TR}$ is approximately equal to the induced-drag ($C_{D,i}$) increase expected when lift coefficient is increased. Therefore, from the data of figure 26, location B appears preferable for the port-nozzle location.

Effect of port-nozzle vector angle.— The effect of port-nozzle vector angle on the induced longitudinal aerodynamics is presented in figure 27. These data show that with the flaps deflected $45^\circ/45^\circ$, the ports with $\Lambda_p = 60^\circ$ are clearly the poorest configuration. This result is not unexpected since the port at $\Lambda_p = 60^\circ$ is blowing so far aft that the spanwise jet has almost no chance of affecting the outboard-flap element.

The choice between the other two port vector angles, 45° and 30° , is not as clear. The ports with $\Lambda_p = 45^\circ$ show slightly higher $\Delta C_{L,TR}$ at low thrust coefficients, that is, $C_{\mu,p} < 0.1$. The $\Delta C_{m,TR}$ data indicate aft loading, and $\Delta C_{D,TR}$ is about equal to the increase in $C_{D,i}$ expected from increasing C_L . Since it was felt that the fighter aircraft in question would have $C_{\mu,p} > 0.1$ for an approach condition in military power, and since the ports with $\Lambda_p = 30^\circ$ showed a slightly higher $\Delta C_{L,TR}$ at $C_{\mu,p} > 0.1$, the port with $\Lambda_p = 30^\circ$ at location B (port 5) was chosen as the superior configuration.

Effect of port-nozzle exit area.— The effect of port-nozzle exit area at location B and $\Lambda_p = 30^\circ$ on the induced longitudinal aerodynamics is presented in figure 28. Here, again, there is no clearly superior configuration, with the small port ($A_{e,p}/A_{e,PRI} = 0.05$) showing a slightly higher $\Delta C_{L,TR}$ at low $C_{\mu,p}$ and with the large port ($A_{e,p}/A_{e,PRI} = 0.10$) seeming to show higher $\Delta C_{L,TR}$ at high $C_{\mu,p}$. As in the cascade selection, the data were also compared at $C_D = 0$, as shown in figure 29. For $C_D = 0$ and $C_{\mu} = 0.9$, both ports produce virtually equal increments in $\Delta C_{L,TR}$. The small port does begin to produce higher levels of $\Delta C_{L,TR}$ at higher C_{μ} , but since $C_D < 0$, this does not represent a reasonable landing thrust setting. An alternate comparison is shown in figure 29(b) for balanced drag ($C_D = 0$) at $NPR = 2.55$. This approximates the NPR that would be required for current engines at military power and is generally an upper limit for the landing thrust setting. At this thrust setting, the larger port shows a slightly higher total C_L which is, of course, what an actual aircraft would require rather than just the induced-lift increment. With this rather arbitrary selection procedure, port 5 (location B with $\Lambda_p = 30^\circ$ and $A_{e,p}/A_{e,PRI} = 0.10$) was chosen as the superior configuration for more detailed study.

SUPERIOR CASCADE AND PORT CONFIGURATIONS

The longitudinal aerodynamics for configurations using the superior cascade and port configurations (cascades 6 and 9 and port 5) are presented in figure 30 at low, medium, and high thrust levels as well as with power off. One major problem with these powered-lift concepts is not necessarily in obtaining lift and drag for the approach but rather in maintaining longitudinal trim. As discussed in reference 18, the need for an alternate means of obtaining trim can lead to a very complex aircraft. This configuration would require some direct force or a significantly larger canard to trim the configuration. The configuration with cascade 6 and $\delta_{PRI} = 45^\circ$ at $C_{\mu} = 0.8$ to 1.0 and $\alpha \approx 14^\circ$, which corresponds to a 100-knot approach in military power for a fighter aircraft similar to those of reference 14, would have

$C_L \approx 2.0$ and C_D such that $\gamma = -3^\circ$ to -6° . (See fig. 30(a).) This would be a reasonable set of approach parameters for the steep no-flare landings required for precision STOL operations. However, at these conditions, the corresponding range of C_m from approximately -0.75 to -0.85 greatly exceeds the trim capability of the canard on this configuration. (See ref. 18.) Therefore, this concept of generating additional lift would be of limited usefulness on this configuration. However, since the primary nozzle is deflected 45° and some 55 percent of the exhaust flow is still passing through this nozzle (i.e., $A_{e,C}/A_{e,PRI} = 0.45$), a great portion of the moment is due to direct jet forces and can be reduced by lowering the nozzle vector angle. This would, of course, also reduce C_L and C_D and change the approach condition; but unless the configuration can be trimmed, these values of lift and drag cannot be maintained anyway.

The powerful effect of the main nozzle is also shown in the data for port 5 (fig. 30(c)) where 90 percent of the exhaust flow was passing through the primary nozzles. For $C_\mu = 0.8$ to 1.0 (as in the cascade discussion), $C_L \approx 2.2$ and $C_m \approx -1.0$. However, because C_D is less than 0, the configuration will not descend. In this case, the only solution is to reduce engine thrust coefficient to provide $C_D > 0$, but this also reduces C_L and still does not reduce the nose-down pitching moment within the trim capability of the canard. It appears that although these spanwise-blowing concepts produce significant induced effects, as will be discussed in the following section, this configuration cannot be trimmed when these concepts are combined with the 45° primary nozzles.

In order to assess the usefulness of these concepts, it is helpful to separate out the induced effects so that large forces and, in particular, large pitching moments that are produced by direct-thrust deflection do not overwhelm the results. Based on the data for a particular configuration in the previous discussion, for example, the usefulness of the induced lift produced by spanwise blowing is completely negated by the extremely large nose-down pitching moments produced by the deflected primary nozzles. However, for a different basic configuration, it may be possible to reduce the large pitching moments caused by direct-thrust deflection by locating the primary nozzles closer to the configuration center of gravity and then take advantage of the induced aerodynamics.

A summary of the induced longitudinal aerodynamics for configurations with cascades 6 and 9 and port 5 are presented in figure 31 at various trailing-edge flap deflections. These data show that, generally, the induced effects for the cascade configurations increase with increasing flap deflection as more of the spanwise flow is turned at the higher deflection. This trend is similar to the induced-lift characteristics for an externally blown flap. The cascade configuration generates an induced-lift increment from about 0.40 to 0.43 at a value of C_μ between 0.8 and 1.0, which is representative of military-power settings. For both cascade configurations when $\delta_f = 45^\circ$, the induced pitching moment is less than half the level of C_m when the direct thrust is included, again indicating the powerful effect of the primary-nozzle exhaust.

The induced longitudinal aerodynamics for the port 5 configuration (fig. 31(c)) show a decidedly different trend with $\Delta C_{L,TR}$ decreasing with increased flap deflection. This indicates that the spanwise jet from the port is not able to maintain attached flow on the highly deflected flap. If it is surmised that the major effect of the spanwise jet is to maintain attached flow, rather than generate induced-circulation lift in the manner of a jet flap, then (from the photograph in fig. 32 where the outboard flap at 26° appears to be attached because of effects from the leading-edge vortex) no increased lift would be expected on the outboard flap even

though the flap is clearly affected by the spanwise jet (as shown in fig. 33). This is borne out where deflections of δ_f of $26^\circ/0^\circ$ and $26^\circ/26^\circ$ appear to have identical results for $\Delta C_{L,TR}$, thus indicating that the major effect of the spanwise jet (i.e., maintaining attached flow) occurs on the inboard flap which was separated since it was not affected by the leading-edge vortex.

A comparison of the induced lift for each of the selected configurations (cascades 6 and 9 and port 5) is shown in figure 34. The cascades are clearly superior in generating induced lift when compared with the port in the thrust-coefficient range at $C_u \approx 1.0$ (i.e., approximately military power on approach). There is not much difference in the two cascade configurations even though the induced lift for cascade 6 falls off more rapidly than the induced lift for cascade 9 at $C_u > 1.5$. This might be expected since cascade 6 was the flush-mounted nozzle which did not have quite the flow-turning performance of the alternate cascade 9. However, as mentioned before, cascade 9 protruded from the side of the nacelle and thus would have a much higher drag than that of cascade 6, especially at transonic or supersonic speeds. At $C_u \approx 2.0$, the port and cascade configurations have similar levels of induced lift ($C_{L,TR} \approx 0.30$ to 0.35); however, this thrust coefficient is beyond that available from engines at military power. It should be noted that although these data are presented as a function of C_u (or total engine mass flow), the actual split in thrust between cascade or port and primary nozzle is approximately equal to the ratio of secondary nozzle area to total nozzle area, as discussed in the section entitled "Static-Thrust Calibration."

A breakdown of the induced lift for cascade 9 and port 5 is given in figure 35. Here, the $\Delta C_{L,TR}$ for the complete configuration with cascade 9 and primary nozzles is significantly greater than the sum of the data for the primary nozzle alone and the cascade alone, thus indicating a beneficial interference between the primary and spanwise exhaust flows. This is not the case for the configuration with port 5 where the complete configuration shows that $\Delta C_{L,TR}$ is similar to that obtained from the sum of the data from the primary nozzle and port 5 alone. Since the port spanwise flow is above the wing and the primary flow is below the wing, it is not surprising that there is less beneficial interference on the configuration with port 5 than with cascade 9.

WING SURFACE PRESSURES

In order to determine the flow phenomena occurring on the configuration, an examination of the wing chordwise surface pressures, span loading, and flow visualization using oil flows is presented in figures 36 to 41.

The effect of flap deflection on the chordwise pressure distribution and the resulting span loading for the unpowered baseline configuration ($\delta_{PRI} = 0^\circ$) are shown in figure 36. It should be noted that the pressures at $\eta = 0.20$ are located on the nacelle centerline; those at $\eta = 0.42$, on the inboard-flap centerline; those at $\eta = 0.64$ and 0.73 , both on the outboard flap; and those at $\eta = 0.91$, near the wing tip (outboard of the trailing-edge flap system). (See fig. 11.) The effect of the trailing-edge flap is typical in that there is a pressure peak located at the knee of the flap and reduced pressures near the wing leading edge, which show the increased loadings produced by the flap. Also, there is not a significant change in the pressure distribution as flap deflection is increased from 26° to 45° , which indicates that the flow is separating on the flap upper surface at the higher deflection angle, as seen in the longitudinal data. The pressure field created by the flap in subsonic

flow is felt at all points on the wing, as shown by the reduced upper-surface pressures at stations inboard and outboard of the flap system ($\eta = 0.20$ and 0.91).

Integration of these chordwise pressure distributions (see ref. 13) gives the span-load distribution shown in figure 36(b). Not surprisingly, as flap deflection is increased, the span load increases even at $\delta_f = 45^\circ$, which shows that the pressure field over the wing integrates out to a slightly increased lift even though the flap is separating.

As mentioned previously, the exhaust from the primary nozzle alone ($\delta_{PRI} = 45^\circ$) induced a lift increment of about $\Delta C_{L,TR} = 0.10$. As shown in figure 37(a), the exhaust flow induced a lower pressure on the wing flap (i.e., $x/c > 0.70$) and reduced leading-edge pressures at $\eta = 0.42$. Since this station is outboard of the nozzle-exhaust location, it can be assumed that this increased loading is due to jet entrainment working the inboard-flap segment. As before, this pressure field influences the entire wing as shown by the slight reduction in pressure at all other stations. The increased loading is also readily apparent in the marked increase in $C_{l,c/\bar{c}}$ at $\eta = 0.42$ as shown in figure 37(b). The integrated span load and chord pressures give a center of pressure for the configuration at 75 percent of local chord (see fig. 41), thus indicating that the primary jet is in fact loading the inboard-flap segment.

The pressure and spanwise-loading distributions produced by the cascade concepts are compared in figure 38 with the data for the baseline primary nozzle alone ($\delta_{PRI} = 45^\circ$) of figure 36 in order to assess the effectiveness of the spanwise blowing on the trailing-edge flap. It can be seen that the major effect of the cascade spanwise blowing is greatly reduced pressures on the outboard flap and wing tip (see fig. 38(a)) with the combined primary and cascade nozzles generating the highest loadings, thus verifying the trends shown in the induced lift of figure 31. The pressures at a station η of 0.42 are actually increased from the primary-nozzle-alone levels when the primary nozzle is shut down and the cascade is blowing alone. Although this level is reduced from the baseline power-off ($C_\mu = 0$) case shown in figure 36, it would indicate that the spanwise jet is affecting the outboard flap to a much greater degree than the inboard flap. From the oil-flow photograph of figure 39, the path of the spanwise jet is clearly visible as it expands and impinges primarily on the lower surface of the outboard flap and wing tip. Where the jet impinges on the lower surface of the flap, a portion of the spanwise flow is being turned and shed as a jet sheet off the flap; the jet sheet should be generating circulation-type lift increments similar to an externally blown flap. The significant reduction in upper-surface pressure distribution and the location of the center of pressure would indicate that circulation-type lift is in fact being generated on this configuration with both primary and cascade nozzles (shown in fig. 41) near 45 percent of the local chord.

A similar analysis for the primary and port nozzles (see figs. 33 and 40) indicates that the effect of the spanwise jet on the outboard-flap pressures is essentially independent of the primary-nozzle flow. The effect of the primary-nozzle flow is still seen at $\eta = 0.42$ as the pressures are increased and local loading is reduced when either the port is run alone or the primary-nozzle C_μ is lowered from 0.473 to 0.351 .

The oil-flow photograph in figure 33 shows clearly the path of the spanwise jet over a portion of the inboard flap and over all the outboard flap ($\delta_f = 45^\circ/45^\circ$). It was felt that this concept would tend to act as a boundary-layer control device on the trailing-edge flaps, rather than as a generator of induced circulation. The

center of pressure for this configuration is at 63 percent of the local chord (fig. 41), which indicates an aft loading with lift on this flap rather than an induced circulation lift which should be centered more around 40 to 50 percent of the local chord. The center of pressure is moved inboard relative to the cascade configuration since the port seems to be affecting part of the inboard flap which was almost totally missed by the cascade concept.

SLOTTED FLAP

One of the purposes of this investigation was to find a means for further increasing thrust-induced lift by having the spanwise jet from the cascades blow on a single-slotted flap rather than on a plain flap. The intent was to have a portion of the spanwise flow pass through the slot and to maintain attached flow on the highly deflected ($\delta_f = 45^\circ$) upper surface of the flap system like on an externally blown flap.

The performance of the single-slotted flap is compared with that of the plain flap in figure 42 for both $\delta_f = 45^\circ/26^\circ$ and $45^\circ/45^\circ$. Even in power-off conditions, a highly deflected slotted flap should have better aerodynamics than a highly deflected plain flap. From the data of figure 42, it is apparent that this slotted flap did not perform as well as the plain flap. It is thought that the reason for this is that the sharp edge on the cove area of the slot (see fig. 4(b)) separated the flow on the lower surface so that little or no flow actually passed through the slot. This then has a twofold effect on flap effectiveness: (1) Without significant slot flow, the upper surface of the flap will remain separated, and (2) the open slot will vent lower-surface high pressures to the upper surface and reduce the already weakened performance of the flap.

This situation was not greatly improved when spanwise blowing from cascade 9 was used. The thrust-induced lift increments $\Delta C_{L,TR}$ are shown in figure 43 for both $\delta_f = 45^\circ/26^\circ$ and $45^\circ/45^\circ$ with and without the slotted flap. The flap with the lower outboard deflection ($\delta_f = 45^\circ/26^\circ$) does show a small improvement in $\Delta C_{L,TR}$ with the slotted flap indicating that some flow is passing through the slot. However, the flap with $\delta_f = 45^\circ/45^\circ$ shows no change in $\Delta C_{L,TR}$, and the slotted flap indicates that no flow is passing through the slots. In fact, the oil-flow photograph in figure 44 shows that some of the upper-surface oil was actually entrained backwards (upstream) through the outboard slot as the strong spanwise jet blew along the underside of the flap. For this case, it is surprising that the slotted flap did not have lower $\Delta C_{L,TR}$ than the plain flap. It would appear that a redesign of both the cove-slot area and the spanwise nozzle (to increase vector angle) are required if a slotted flap is to perform properly on this configuration.

CONCLUSIONS

A wind-tunnel investigation has been conducted in the Langley 4- by 7-Meter Tunnel to determine the longitudinal and induced aerodynamics of spanwise blowing on the trailing-edge flap system of a representative advanced fighter-aircraft configuration. This spanwise blowing on the trailing-edge flap contrasts with the more conventional leading-edge spanwise blowing used to enhance leading-edge vortex flows. This study encompassed two concepts: (1) a high mass-flow jet (cascade) located under the wing just ahead of the trailing-edge flap, and (2) a relatively low mass-flow jet (port) located above the wing just aft of the flap hinge line. Data were obtained at several spanwise-blowing vector angles, nozzle exit areas, thrust

coefficients, and flap deflections to determine the superior configuration for each concept. This screening phase of the test was conducted at nominal-approach angles of attack from 12° to 16° , and then the superior configurations were tested over a more complete angle-of-attack range from 0° to 20° . Data were obtained at tunnel free-stream dynamic pressures between 20 and 40 lbf/ft² at total ideal thrust coefficients from 0 to 2. The main conclusions from this study are summarized in the following comments. It should be noted that these conclusions apply for these configurations with the primary nozzles deflected 45° and that this precludes obtaining trimmed conditions with the existing canard.

1. The primary nozzles on the basic configurations produce rather small increments in thrust-induced lift, which seem to be the result of the exhaust flow entraining the flow over the inboard-flap element. It also appears that the entrainment is weak since the effect is not significant at high flap deflection or on the outboard-flap element.

2. The superior port configuration was effective in generating induced-lift increments from about 0.30 to 0.35; however, they occurred at total thrust coefficients from 1.5 to 2.0, which are above the range available for military power.

3. The superior port configuration is more effective in generating induced lift when the inboard-flap element is deflected 26° than when the flap is deflected 45° . This indicates that the spanwise jet, although covering most of the trailing-edge flap, is not maintaining attached flow at the high flap deflections. Also, when the outboard-flap element is deflected 26° , it appears that the flow is already attached because of leading-edge vortex effects and, therefore, no further effect would be expected since the major effect of the spanwise jet is to maintain attached flow.

4. The superior cascade configurations are very effective for generating untrimmed induced-lift increments from about 0.4 to 0.43, and these occurred at total ideal thrust coefficients from 0.8 to 1.0, which are representative of what would be available from engines at military power.

5. The superior cascade configurations are more effective in generating induced lift at the highest flap deflection of $45^\circ/45^\circ$. This concept was intended to produce thrust-induced lift by having the spanwise jet turned downward by the trailing-edge flap and shed as a jet sheet similar to that of an externally blown flap. From the pressure distribution and the trends in thrust-induced lift with flap deflection, it would appear that this concept was fairly effective in turning the spanwise flow and in generating the thrust-induced lift like that present on an externally blown flap.

Langley Research Center
National Aeronautics and Space Administration
Hampton, VA 23665
January 13, 1984

REFERENCES

1. Paulson, John W., Jr.; and Thomas, James L.: Summary of Low-Speed Longitudinal Aerodynamics of Two Powered Close-Coupled Wing-Canard Fighter Configurations. NASA TP-1535, 1979.
2. Paulson, John W., Jr.; and Thomas, James L.: Effect of Twist and Camber on the Low-Speed Aerodynamic Characteristics of a Powered Close-Coupled Wing-Canard Configuration. NASA TM-78722, 1978.
3. Paulson, John W., Jr.; Thomas, James L.; and Winston, Matthew M.: Transition Aerodynamics for Close-Coupled Wing-Canard Configuration. AIAA Paper 79-0336, Jan. 1979.
4. Paulson, J. W., Jr.: An Analysis of Thrust-Induced Effects on the Longitudinal Aerodynamics of STOL Fighter Configurations. AIAA-80-1879, Aug. 1980.
5. Paulson, John W., Jr.: Thrust-Induced Aerodynamics of STOL Fighter Configurations. Tactical Aircraft Research and Technology - Volume I, NASA CP-2162, Part 2, 1981, pp. 695-712.
6. Whitten, Perry D.: An Experimental Investigation of a Vectored-Engine-Over-Wing Powered-Lift Concept. Volume II - High Angle of Attack and STOL Tests. AFFDL-TR-76-92, Vol. II, U.S. Air Force, Mar. 1978. (Available from DTIC as AD B033 094L.)
7. Leavitt, Laurence D.; and Yip, Long P.: Effects of Spanwise Nozzle Geometry and Location on the Longitudinal Aerodynamic Characteristics of a Vectored-Engine-Over-Wing Configuration at Subsonic Speeds. NASA TP-1215, 1978.
8. Whitten, P. D.; and Howell, G. A.: Investigations of the VEO-Wing Concept in an Air-to-Ground Role. AFFDL-TR-79-3031, U.S. Air Force, Mar. 1979.
9. Quinto, P. Frank; and Paulson, John W., Jr.: Thrust-Induced Effects on Subsonic Longitudinal Aerodynamic Characteristics of a Vectored-Engine-Over-Wing Configuration. NASA TP-2228, 1983.
10. Stumpfl, Stephen C.: Vectored Engine-Over-Wing Concept Development. Proceedings of a Workshop on V/STOL Aircraft Aerodynamics - Volume II, C. Henderson and M. Platzler, eds., U.S. Navy, May 1979, pp. 850-875. (Available from DTIC as AD A078 909.)
11. Paulson, John W.; Whitten, Perry D.; and Stumpfl, Stephen C.: Wind-Tunnel Investigation of the Powered Low-Speed Longitudinal Aerodynamics of the Vectored-Engine-Over (VEO) Wing Fighter Configuration. NASA TM-83263, 1982.
12. Banks, Daniel W.; Quinto, P. Frank; and Paulson, John W., Jr.: Thrust-Induced Effects on Low-Speed Aerodynamics of Fighter Aircraft. NASA TM-83277, 1982.
13. Doonan, J. G.; and Davis, W. H., Jr.: Advanced Exhaust Nozzle Concepts Using Spanwise Blowing for Aerodynamic Lift Enhancement. AIAA-82-1132, June 1982.
14. Bavitz, Paul C.; et al.: Configuration Development of Advanced Fighters - Volume 1, Executive Summary. AFWAL-TR-80-3142, Volume 1, U.S. Air Force, Nov. 1980.


- 
15. Cornish, J. J., III: High Lift Applications of Spanwise Blowing. ICAS Paper No. 70-09, Sept. 1970.
 16. Dixon, C. J.: Lift and Control Augmentation by Spanwise Blowing Over Trailing Edge Flaps and Control Surfaces. AIAA Paper No. 72-781, Aug. 1972.
 17. Leavitt, Laurence D.: Longitudinal Aerodynamic Characteristics of a Vectored-Engine-Over-Wing Configuration at Subsonic Speeds. NASA TP-1533, 1979.
 18. Paulson, J. W., Jr.; Gatlin, G. M.; Quinto, P. F.; and Banks, D. W.: Trimming High Lift for STOL Fighters. AIAA-83-0168, Jan. 1983.

TABLE I.- DESCRIPTION OF CONFIGURATIONS TESTED

(a) Cascade configurations

Nozzle description			Configurations tested						
Cascade	$A_{e,C}/A_{e,PRI}$	Vector angle, deg	Cascade nozzle alone at δ_f of -		Cascade and primary nozzles at δ_f of -				
			45°/45°	45°/26°	45°/45°	45°/26°	26°/26°	26°/0°	0°/0°
1	0.20	-30				X			
2	.20	0		X		X			
3	.20	30	X		X	X			
4	.30	0		X		X			
5	.45	0		X		X			
6	.45	30	X		X	X	X	X	
7	.60	-30				X			
8	.60	0		X	X	X			X
9	.60	30	X	X	X	X	X		X

(b) Port configurations

Nozzle description				Configurations tested						
Port	$A_{e,P}/A_{e,PRI}$	Vector angle, deg	Location	Port nozzle alone at δ_f of -		Port and primary nozzles at δ_f of -				
				45°/45°	45°/26°	45°/45°	45°/26°	26°/26°	26°/0°	0°/0°
1	0.05	30	A			X				
2	.05	45	A			X				
3	.05	60	A			X				
4	.05	30	B			X				
5	.10	30	B	X	X	X	X	X	X	
6	.10	45	B			X				
7	.10	60	B			X				

TABLE II.- BASIC MODEL GEOMETRY

Body:	
Length, in.	91.20
Width, in.	7.20
Wing:	
A	2.79
S, ft	5.73
b, in.	48.0
\bar{c} , in.	19.11
c at root, in.	27.86
c at side of body (3.60), in.	24.66
c at tip, in.	6.52
Λ_{LE} , deg	50
Λ_{TE} , deg	27.86
Moment center, in.	F.S. 80.53
Airfoil:	
Section	6% aft cambered
t/c at root	0.06
t/c at tip	0.06
Twist at tip, deg	-6
Wing flaps:	
Inboard:	
$b_{f,i}$, in.	6.34
c_i (B.L. 7.0), in.	5.61
c_o (B.L. 13.34), in.	4.25
Outboard:	
$b_{f,o}$, in.	6.34
c_i (B.L. 13.34), in.	4.25
c_o (B.L. 19.68), in.	2.88
Hinge line	0.726c
Nacelle:	
Length, in.	24.56
Width, in.	3.9
Nozzle exit:	
Width, in.	2.57
Height, in.	0.74
Location:	
$\delta_{PRI} = 0^\circ$:	
F.S.	101.79
B.L.	5.04
W.L.	8.26
$\delta_{PRI} = 45^\circ$:	
F.S.	101.39
B.L.	5.04
W.L.	7.29
Canard:	
A (exposed)	2.76
S (exposed), ft ²	1.01
b/2 (exposed), in.	10.04
c at root (B.L. 3.6), in.	11.71
c at tip, in.	2.82
Canard airfoil:	
Section root	NACA 65A004 (MOD)
Section tip	NACA 65A003 (MOD)
t/c at root	0.04
t/c at tip	0.03
Twist, deg	0

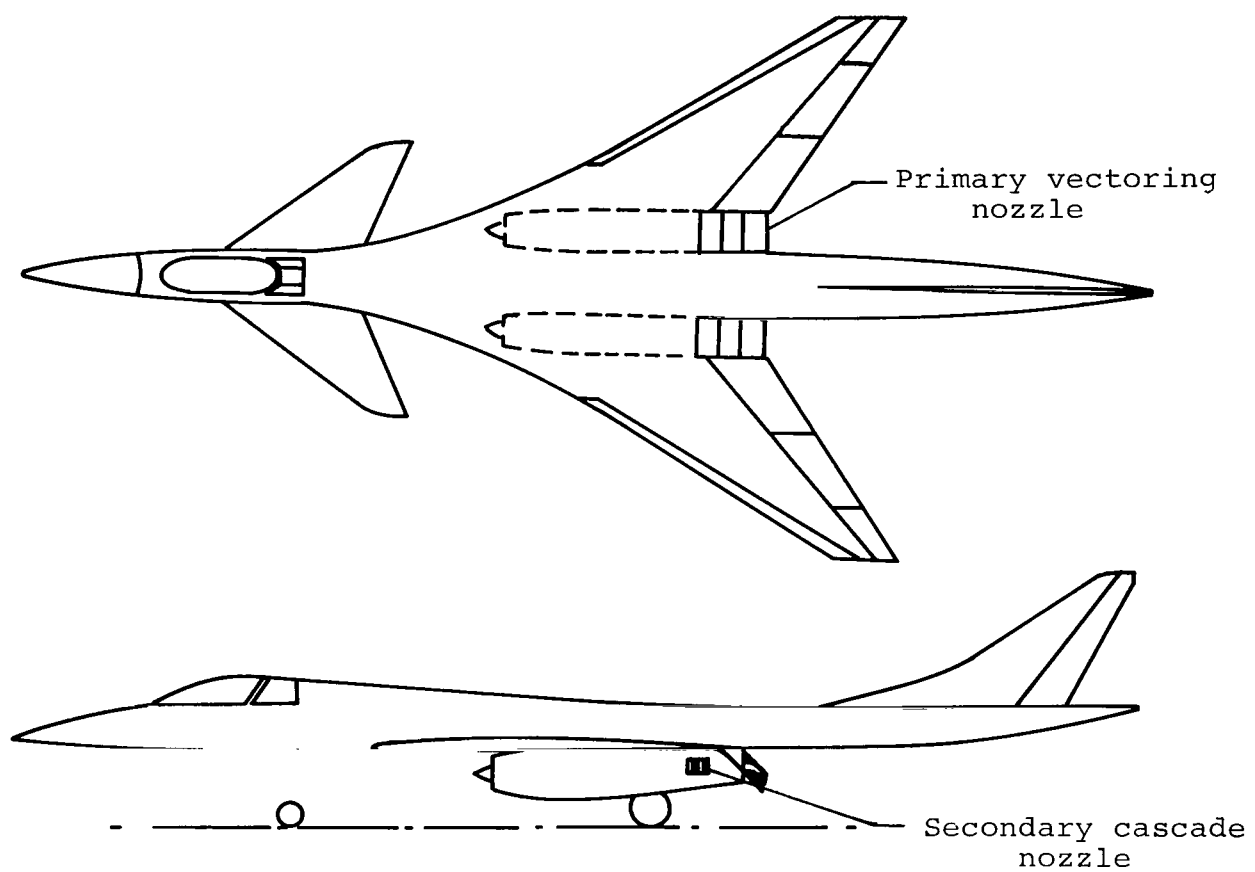


Figure 1.- Sketches of advanced fighter configuration with underwing spanwise blowing (cascade).

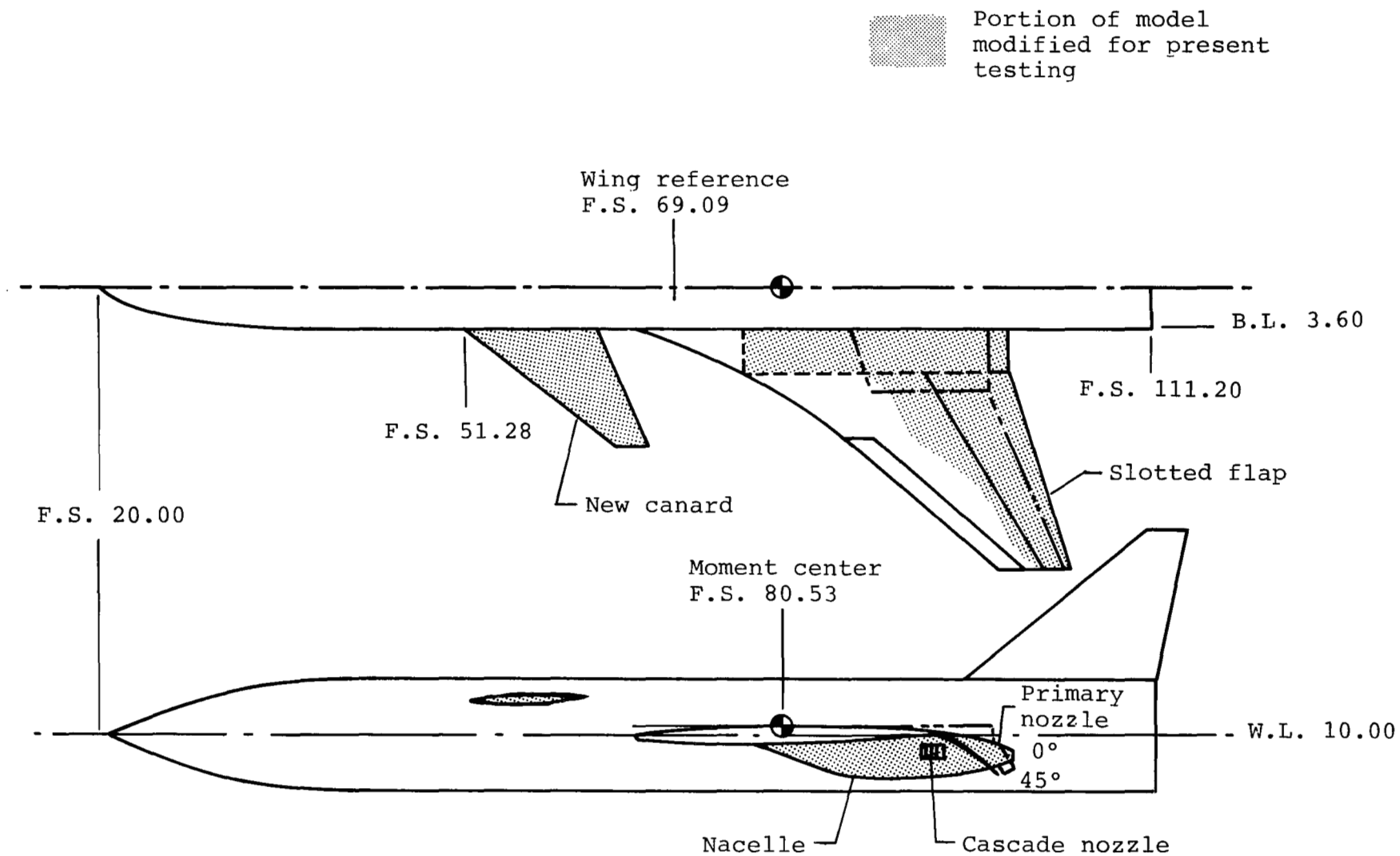


Figure 2.- Sketches of modified NASA wing-canard fighter model. Dimensions are given in inches unless otherwise specified.

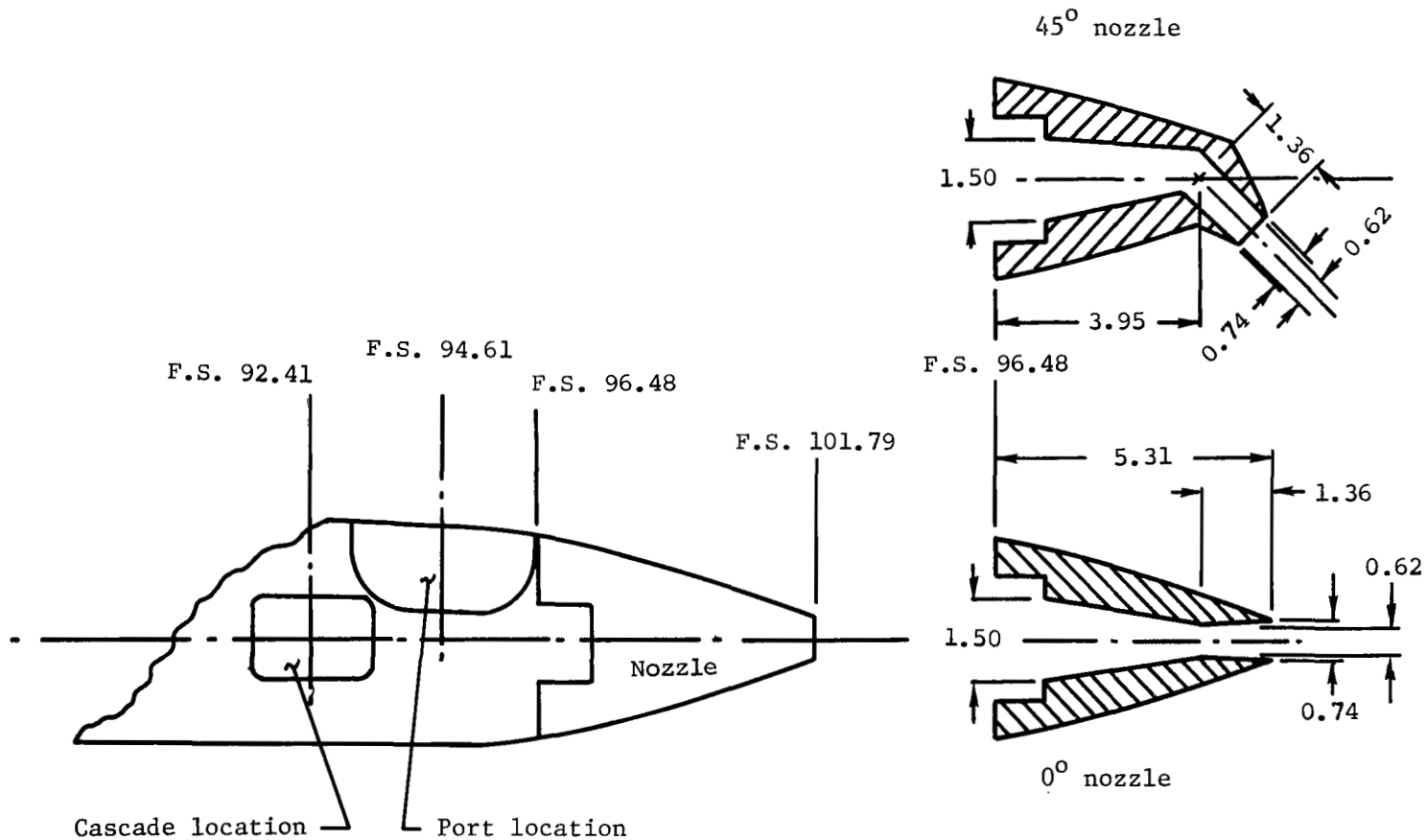
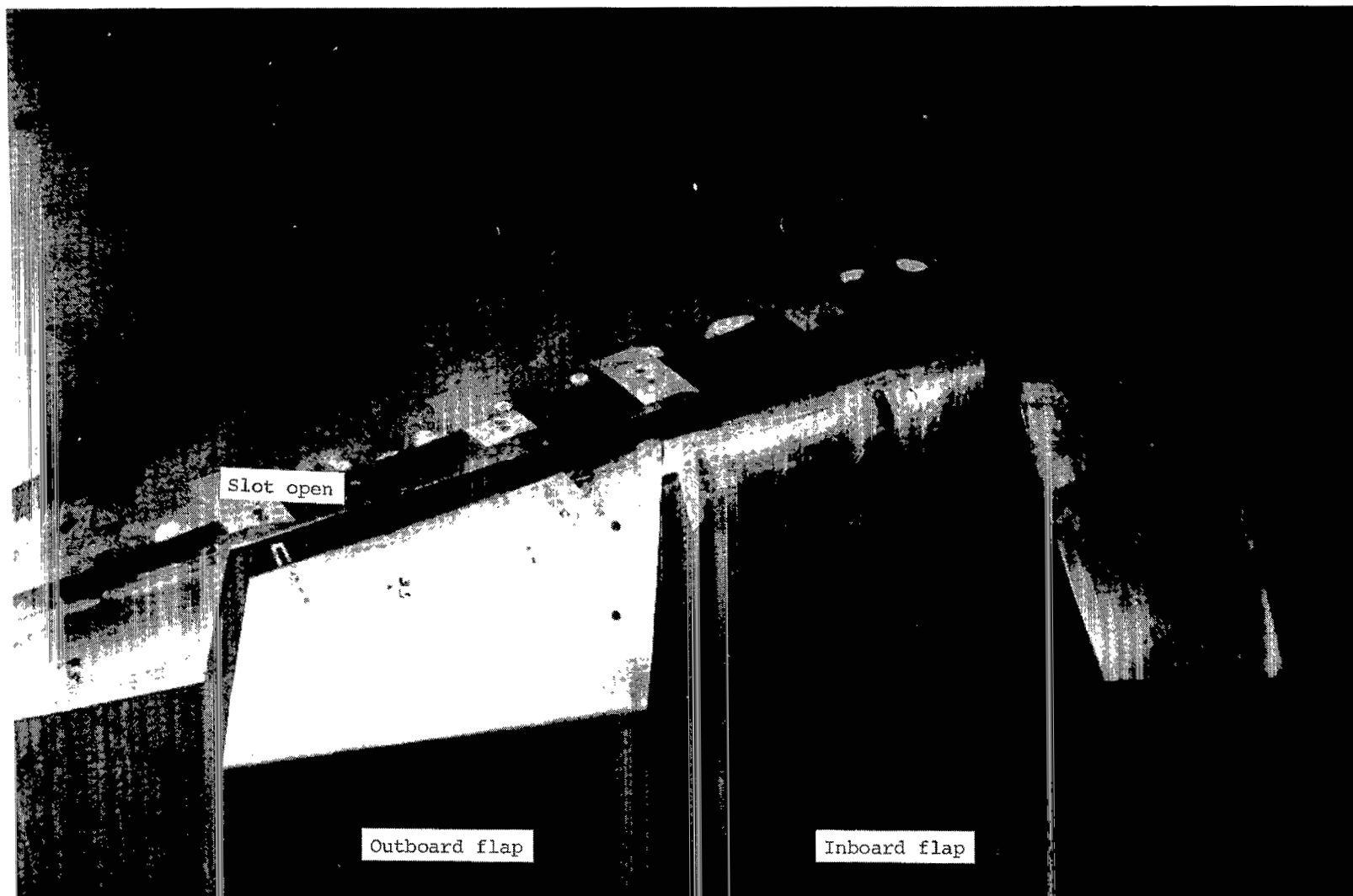


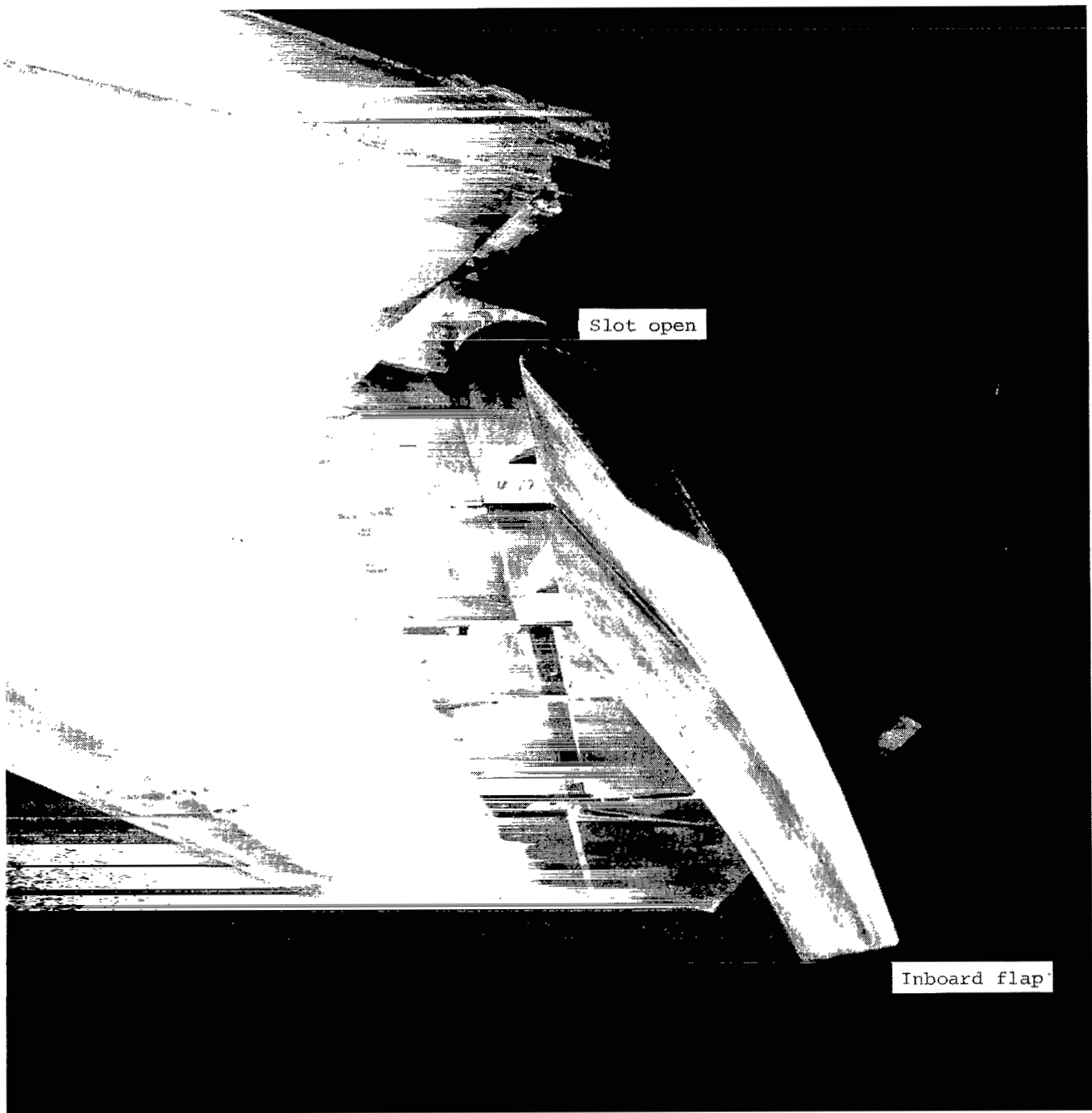
Figure 3.- Sketches of primary-nozzle geometry. Dimensions are given in inches unless otherwise specified.



L-83-137

(a) Top view of flap.

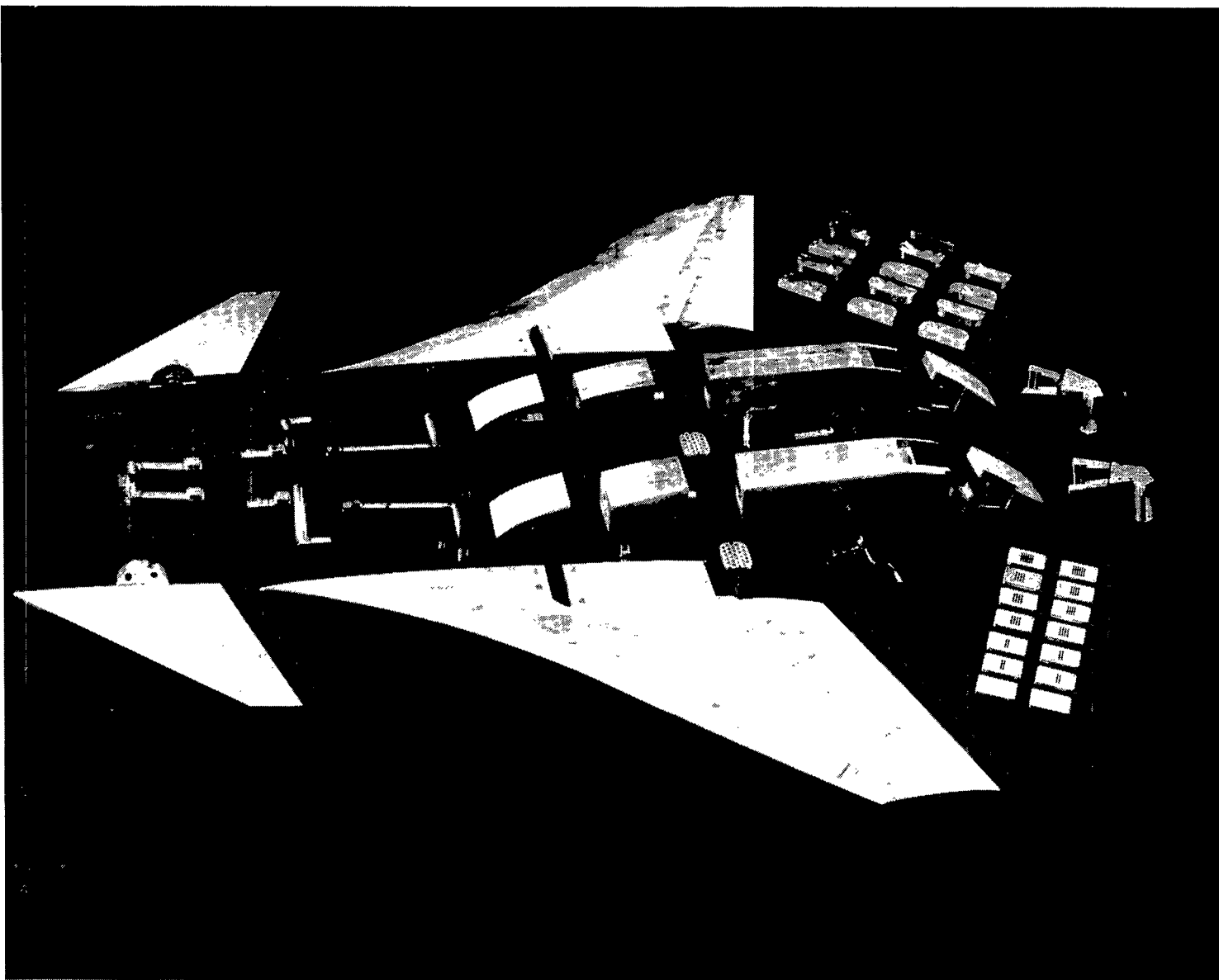
Figure 4.- Slotted trailing-edge flap.



L-83-138

(b) Bottom view of flap.

Figure 4.- Concluded.



L-83-139

Figure 5.- New and modified parts for NASA wing-canard fighter model.

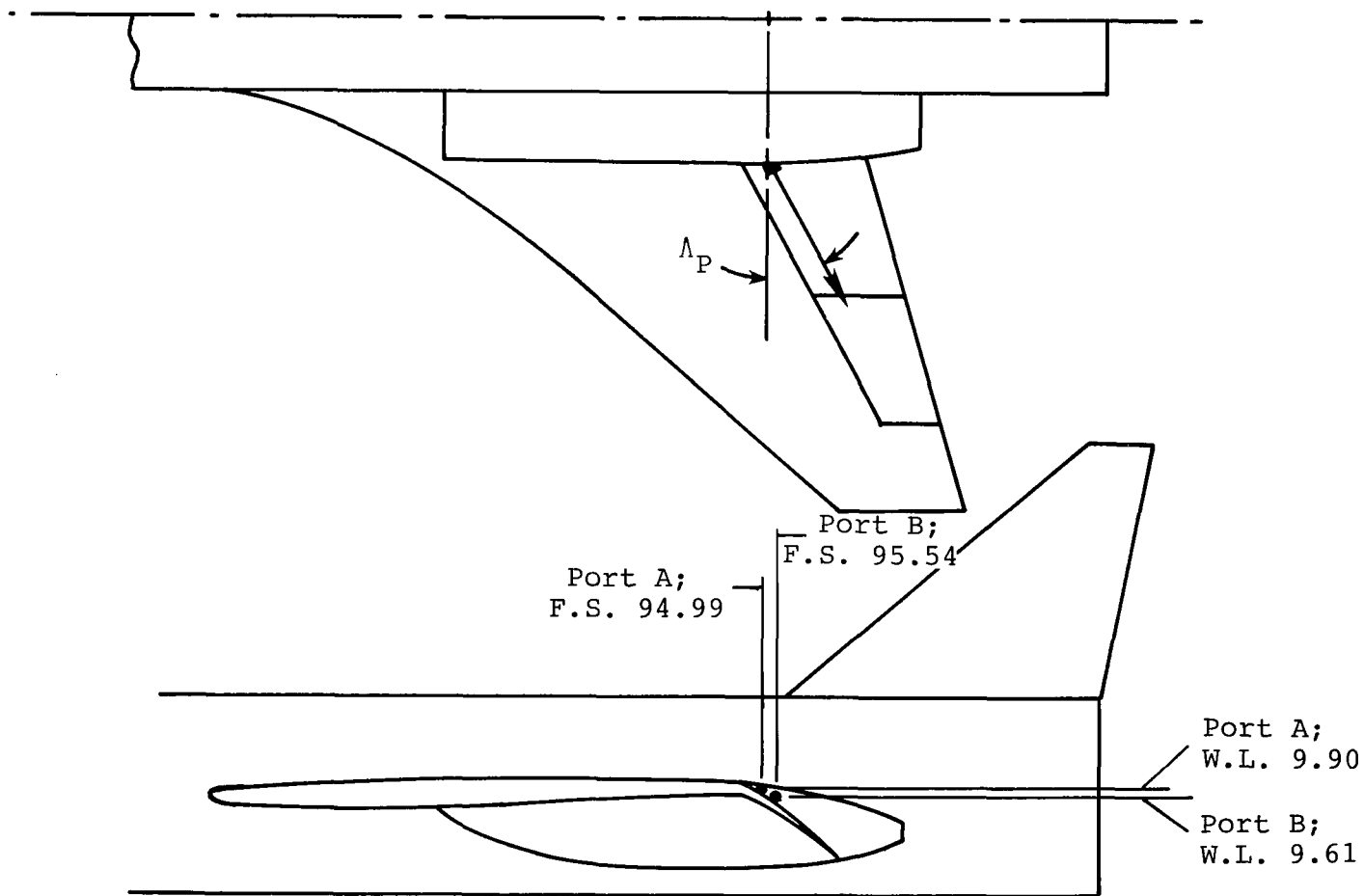


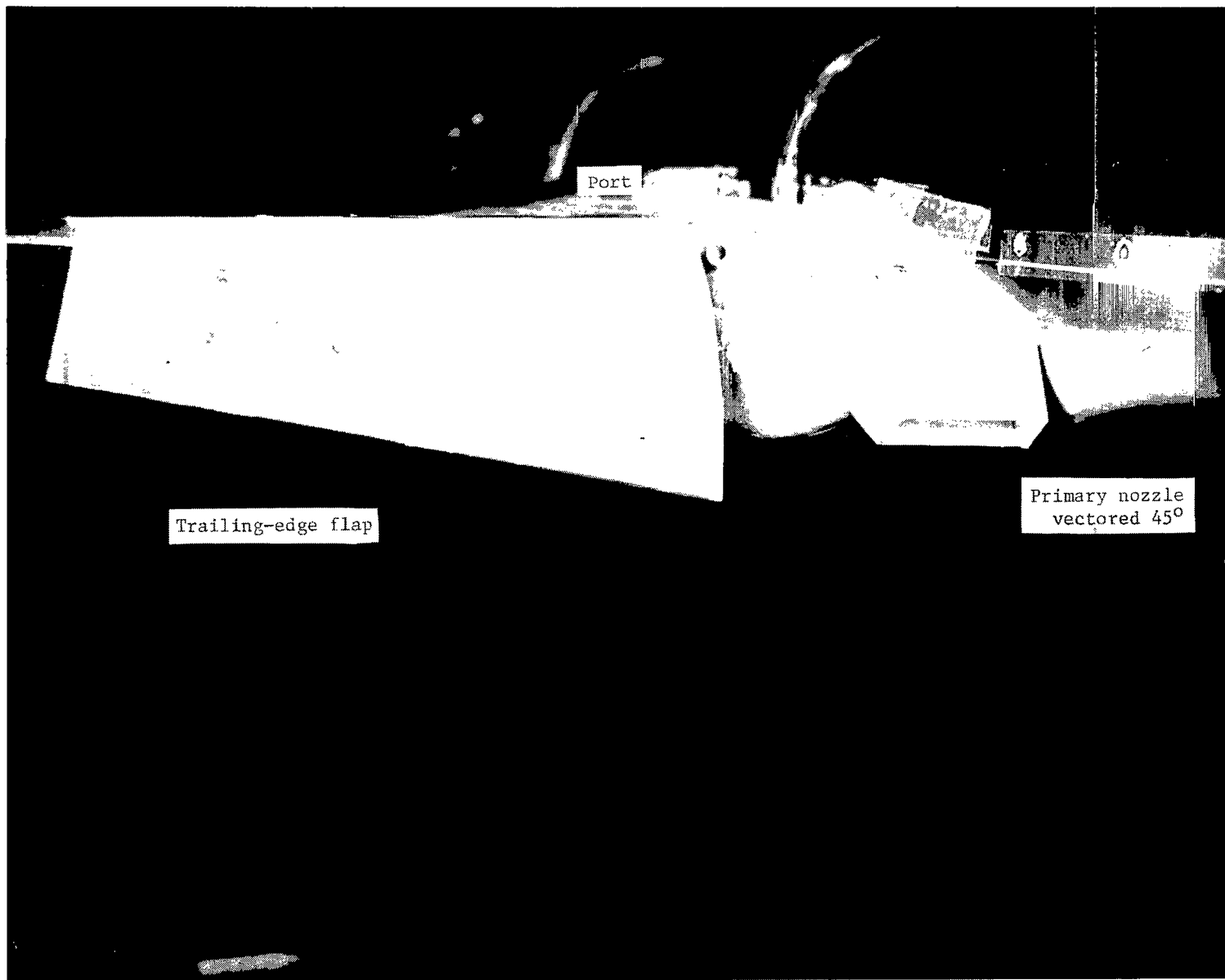
Figure 6.- Sketches showing location of ports A and B above trailing-edge flap on modified NASA wing-canard fighter model. Dimensions are given in inches.



L-83-140

(a) Six port configurations with blank.

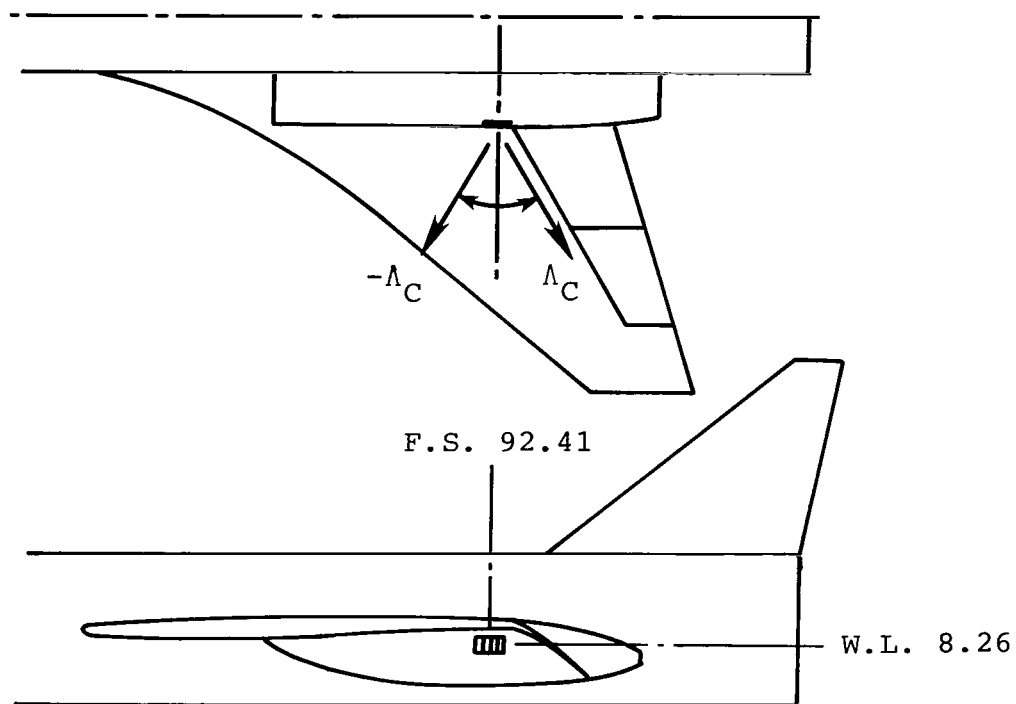
Figure 7.- Port hardware.



L-81-8585.1

(b) Location of port 7.

Figure 7.- Concluded.



Basic cascade nozzle

Alternate cascade nozzle

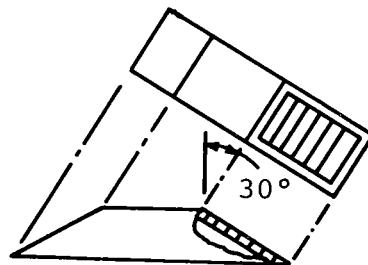
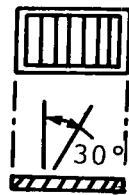
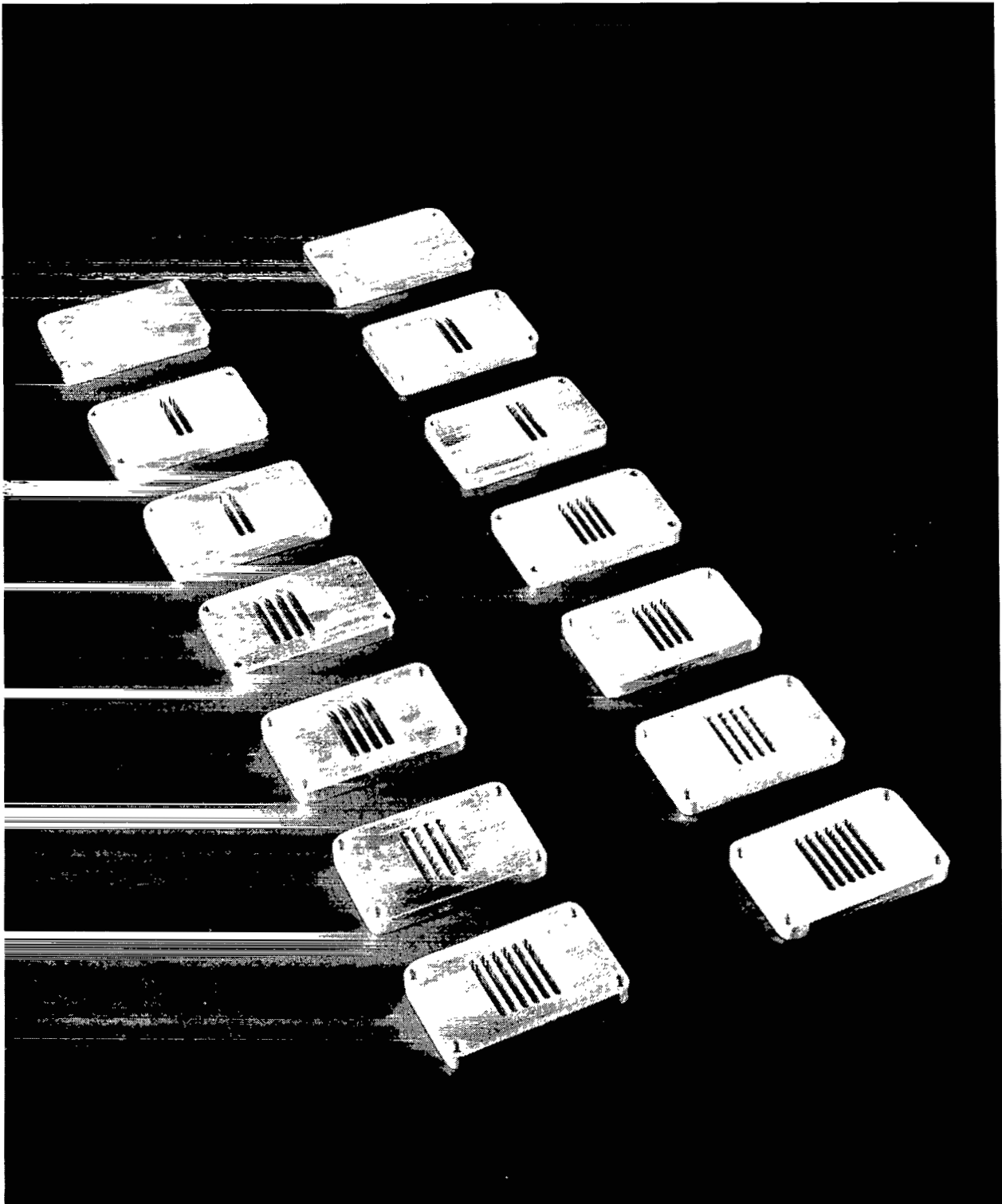


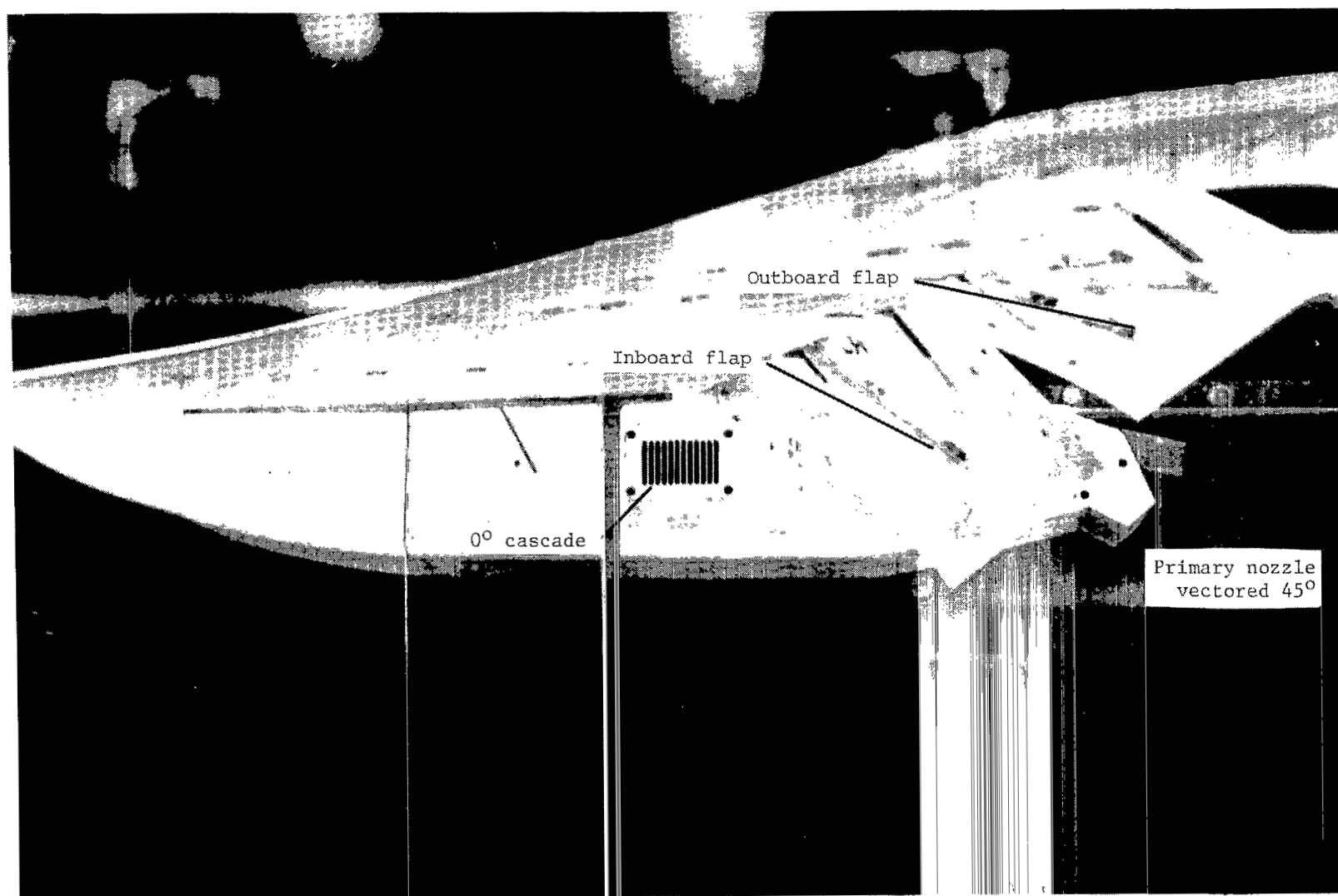
Figure 8.- Sketches showing location of cascades under trailing-edge flap on modified NASA wing-canard fighter model. Dimensions are given in inches unless otherwise specified.



L-83-141

(a) Six cascade configurations with blank.

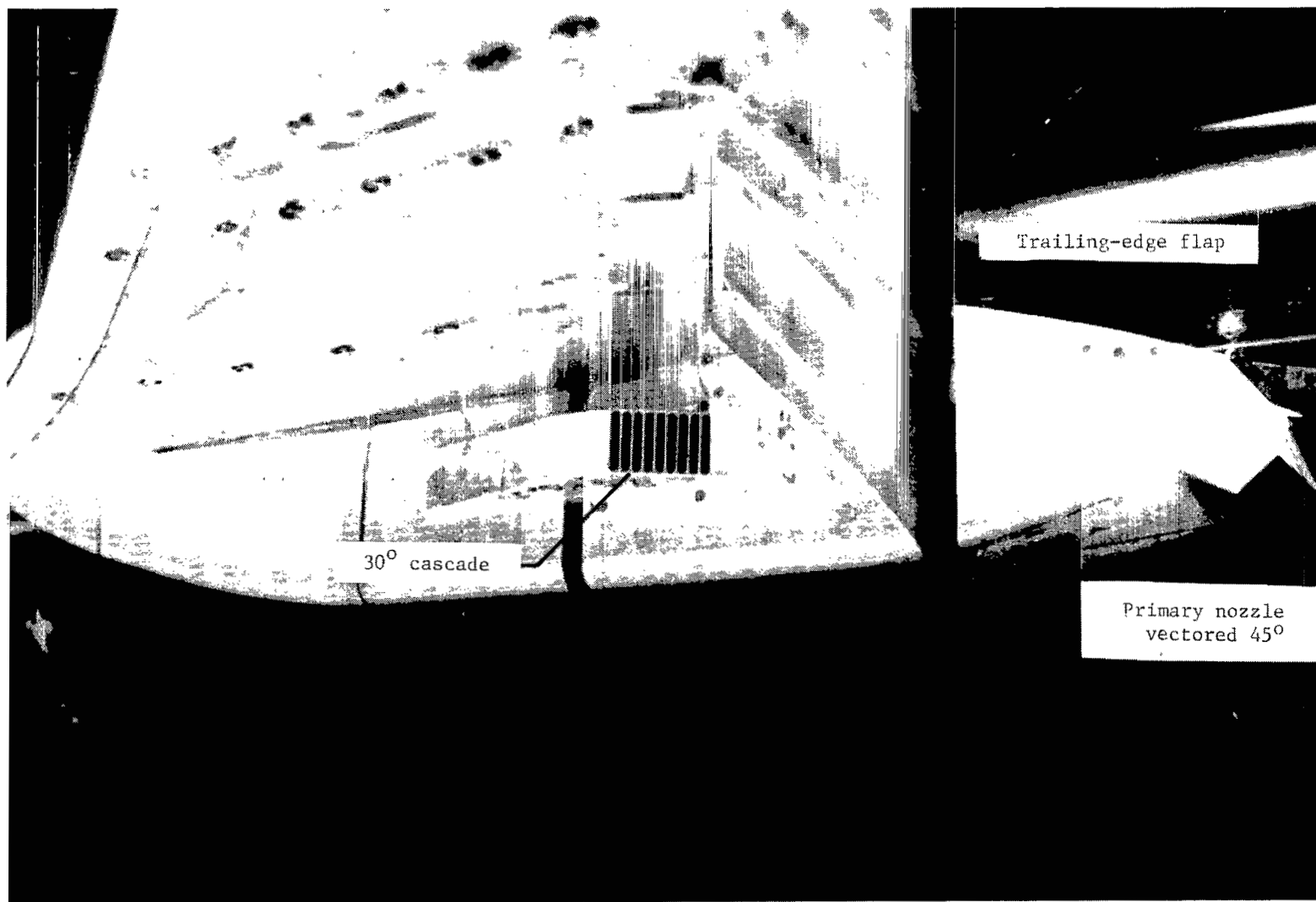
Figure 9.- Cascade hardware.



L-83-142

(b) Location of cascade 8.

Figure 9.- Continued.



L-83-143

(c) Location of cascade 9.

Figure 9.- Concluded.

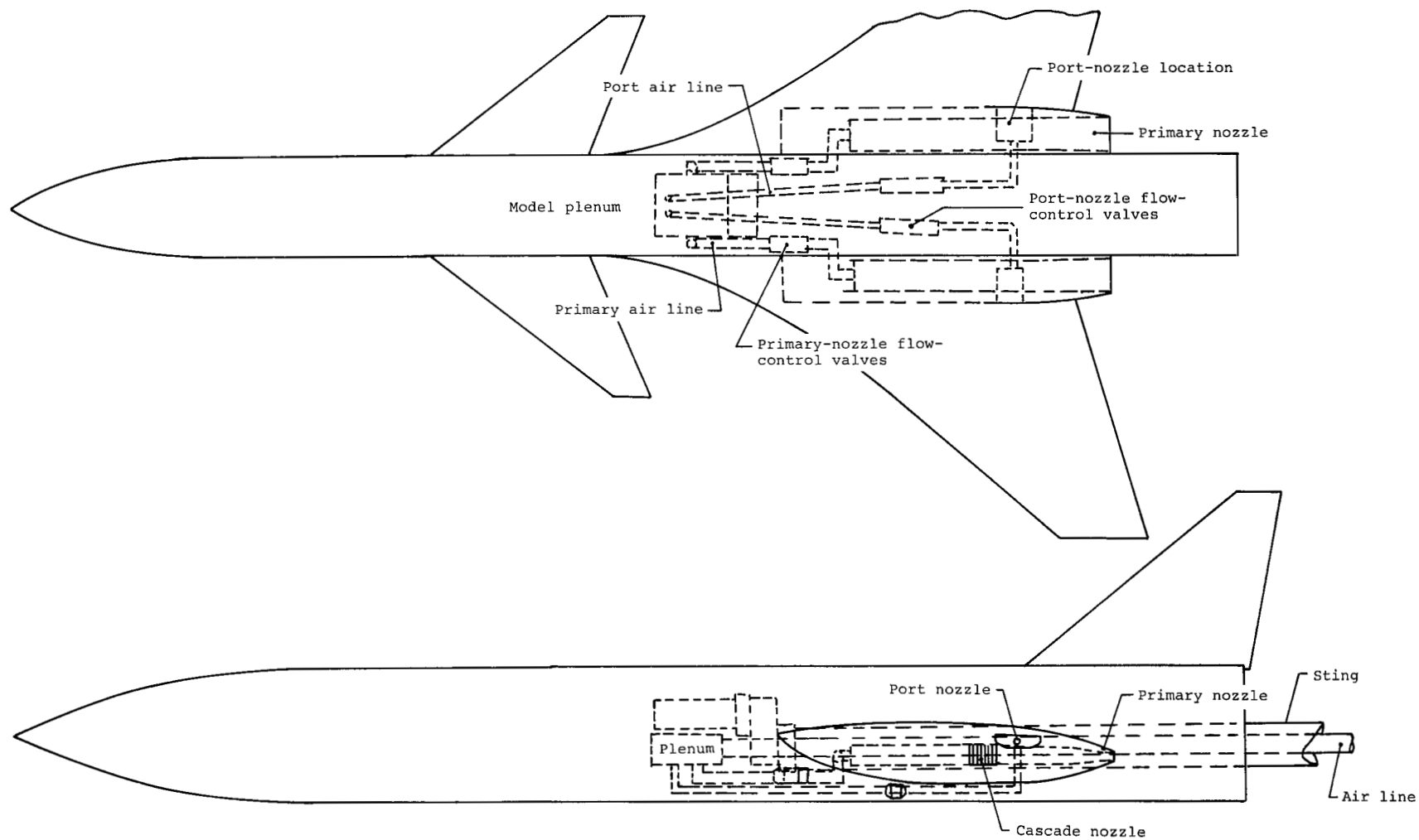


Figure 10.- Sketches of air-line system in model.

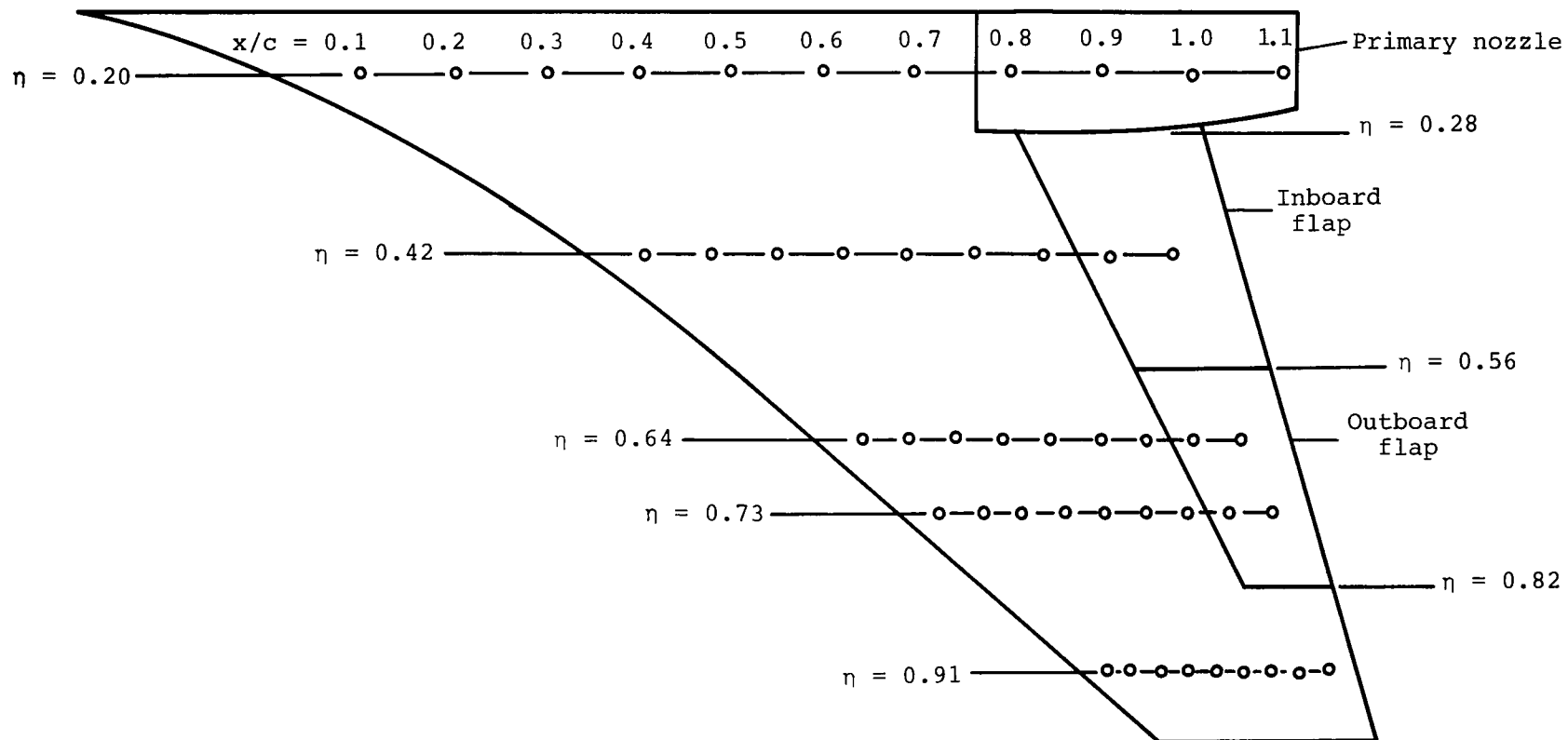


Figure 11.- Sketch of wing-surface pressure-tap locations on left wing. All rows have the same x/c station as $y/c = 0.20$ on both upper and lower surfaces.

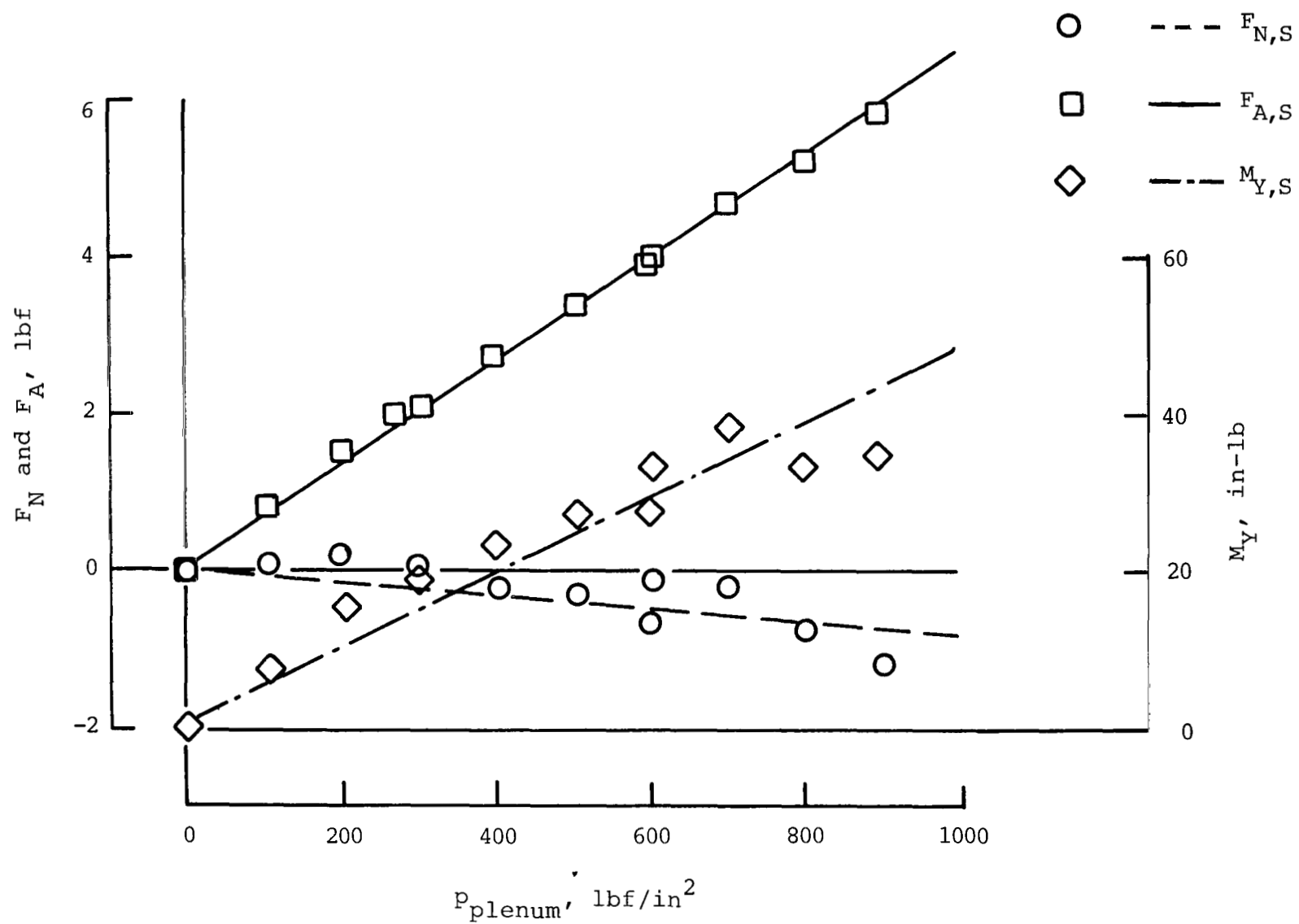
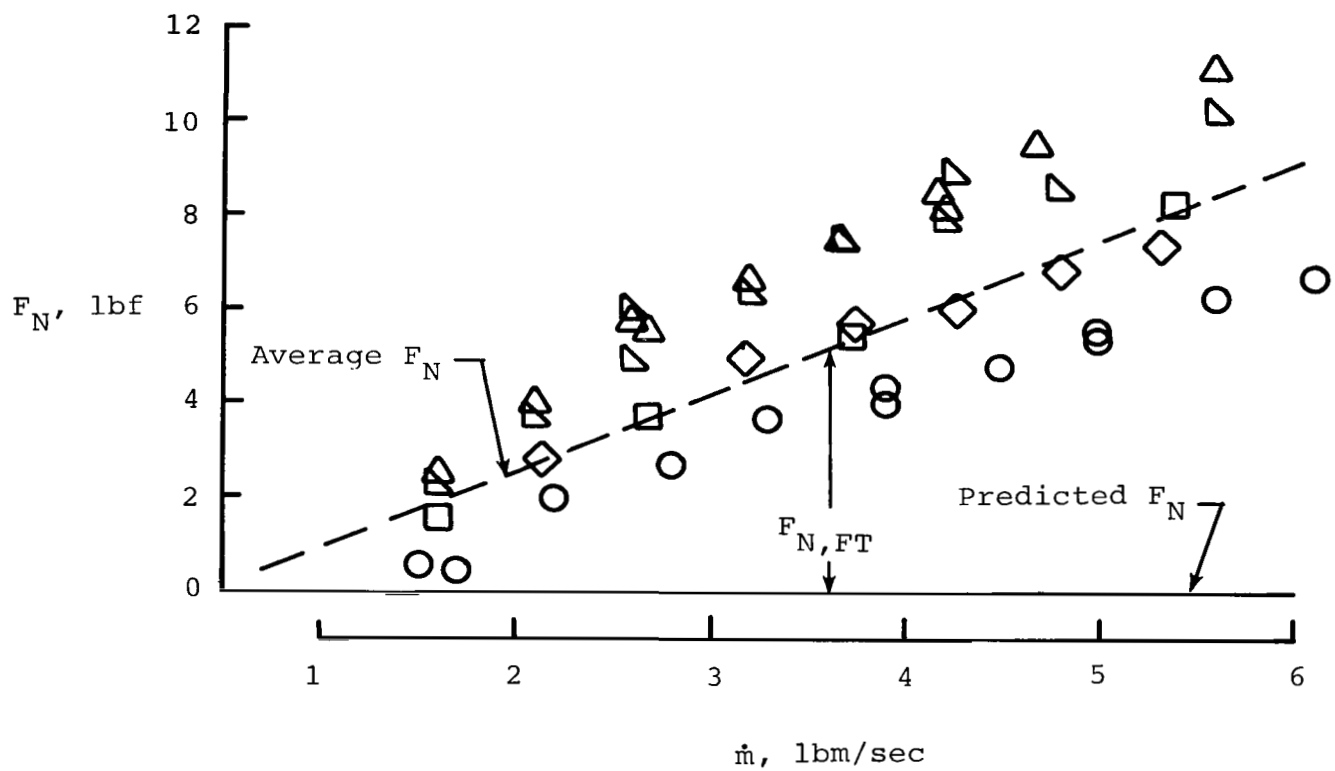
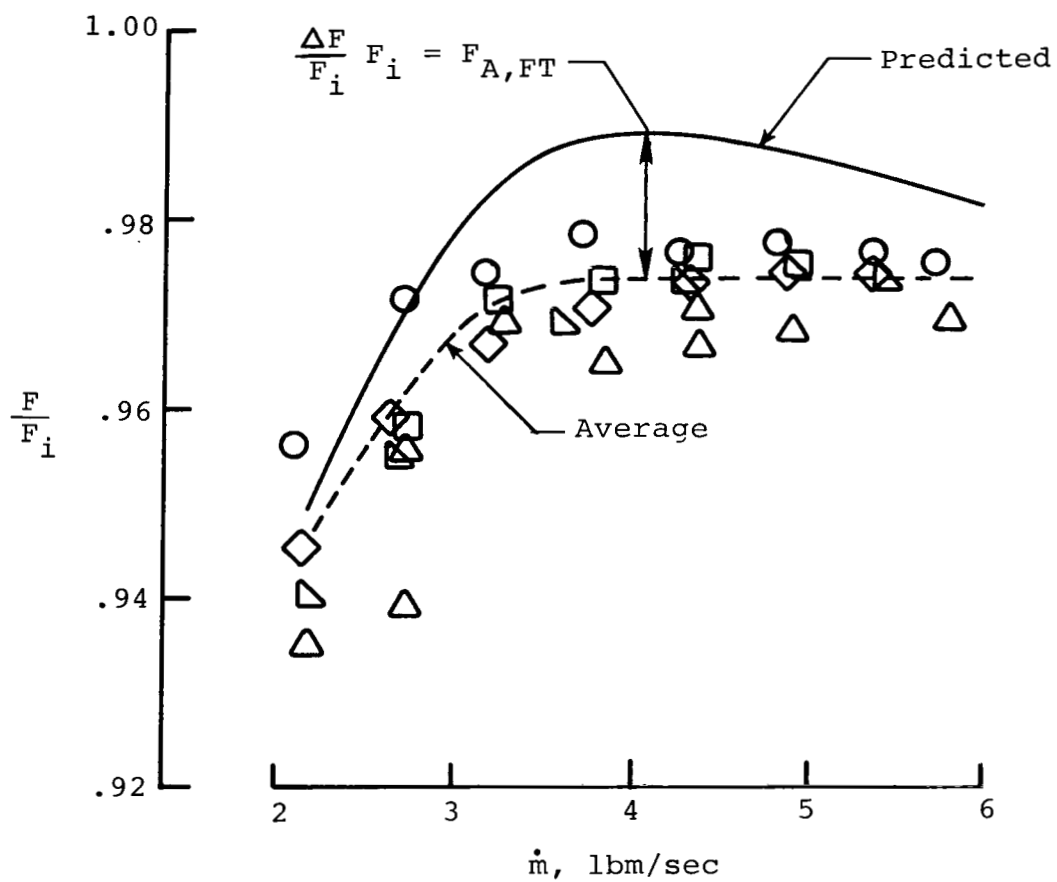


Figure 12.- Data for sting-pressure tare.



(a) Normal force plotted against mass flow.

Figure 13.- Example of data of typical flowing (power-on) tares. Symbols represent repeat runs.



(b) F/F_i plotted against mass flow.

Figure 13.- Concluded.

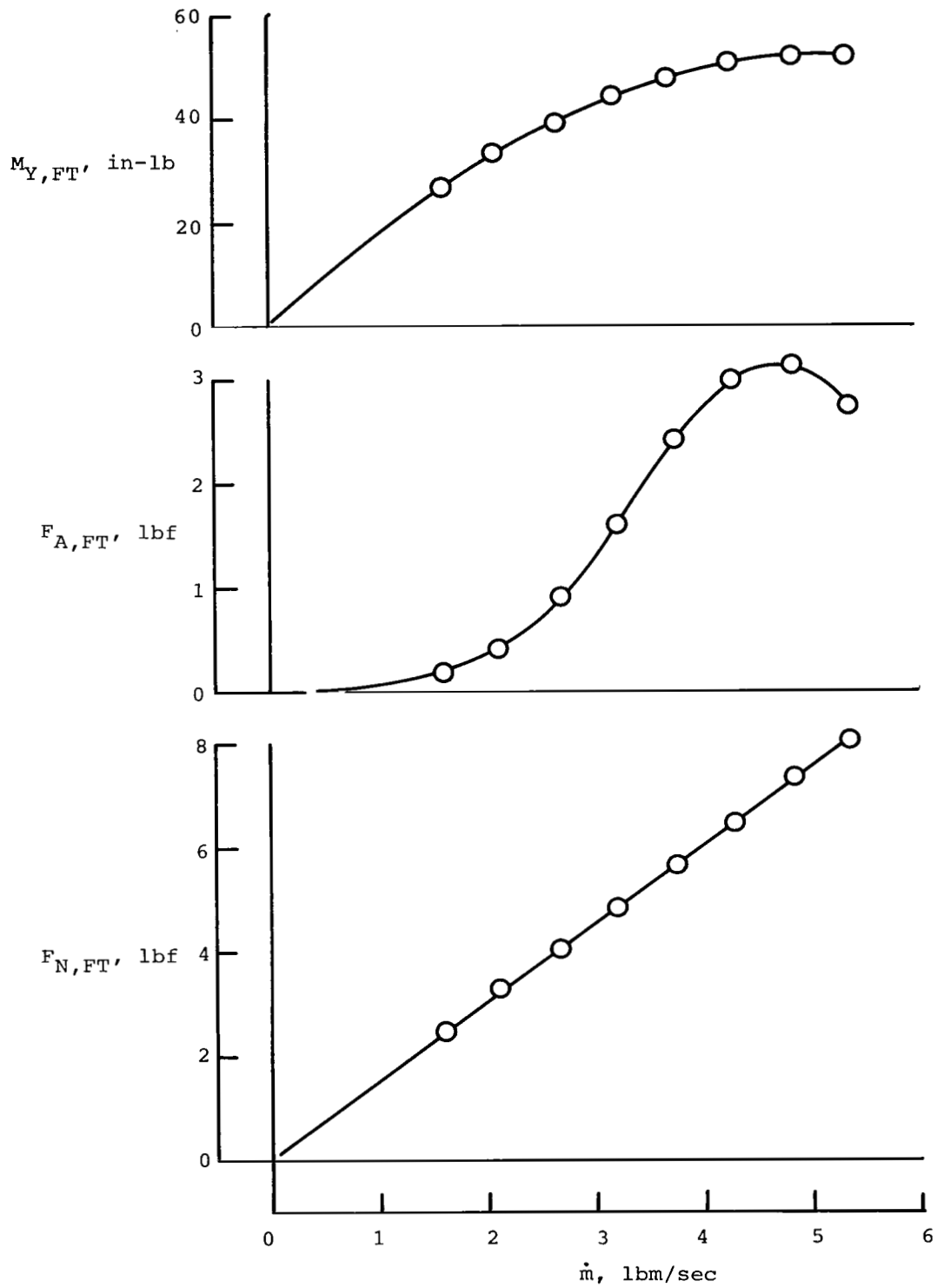


Figure 14.- Final normal-force, axial-force, and pitching-moment flowing (power-on) tares applied to wind-tunnel data.

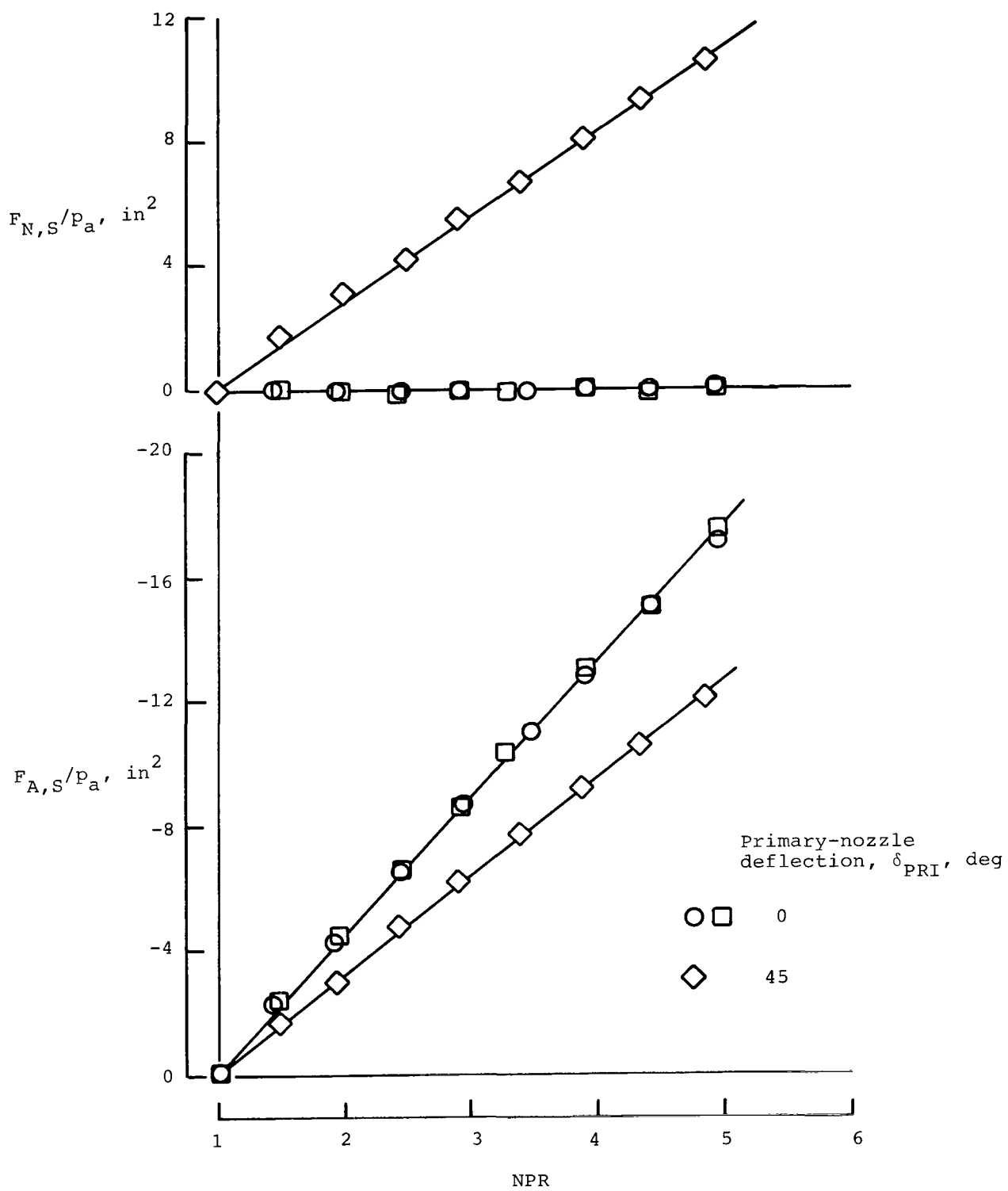
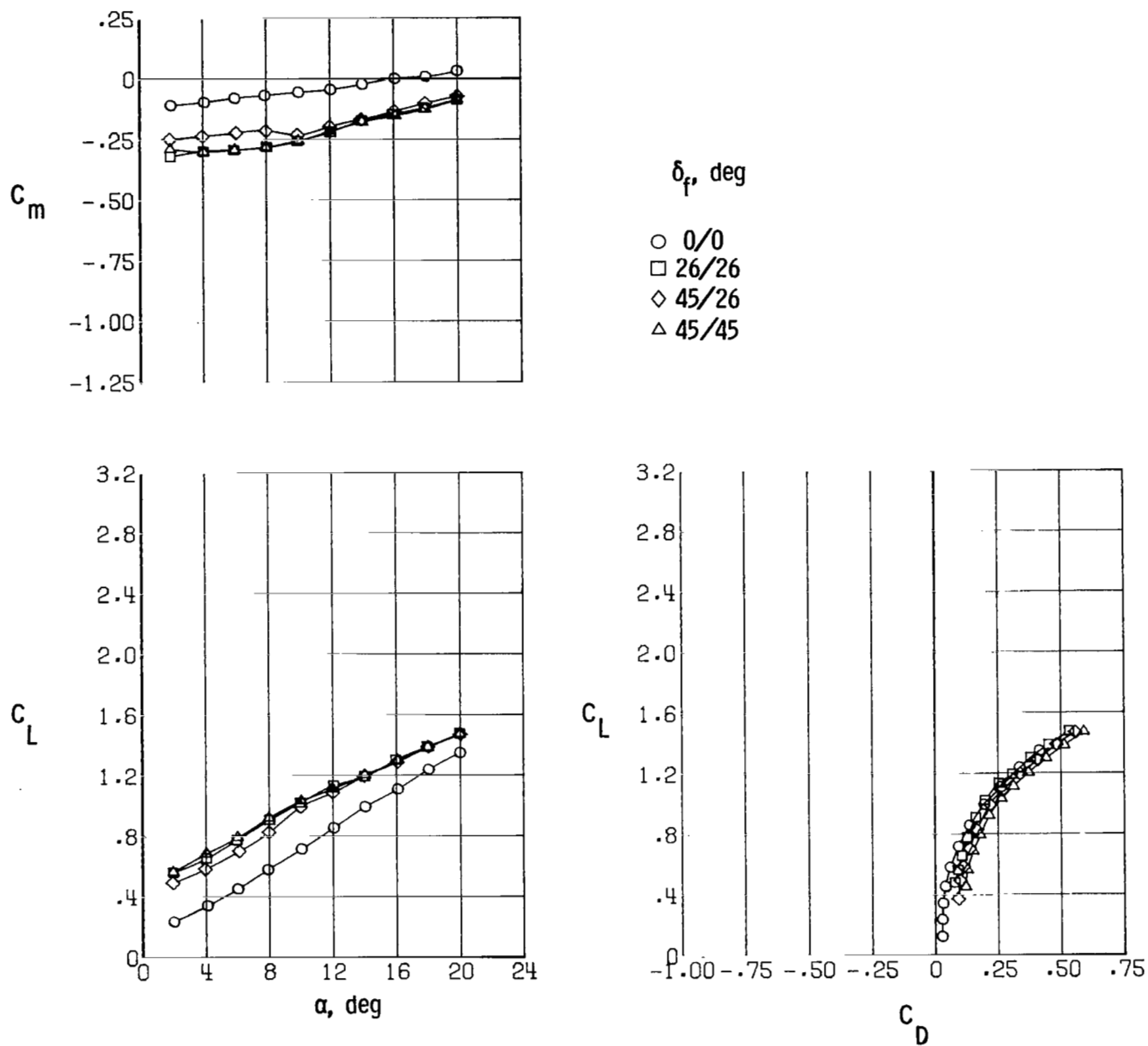
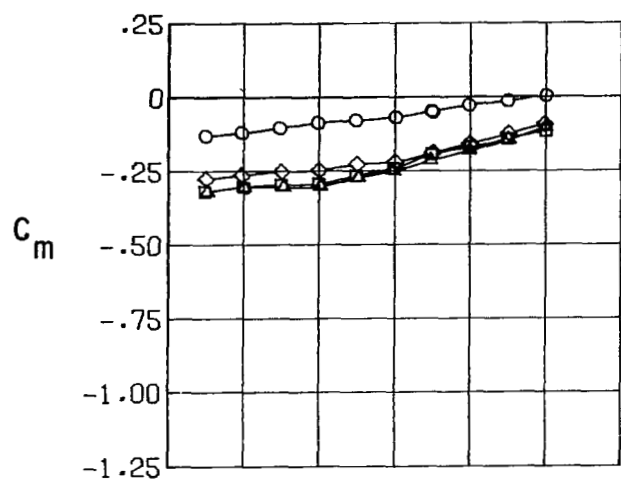


Figure 15.- Example of typical static-thrust calibration data.



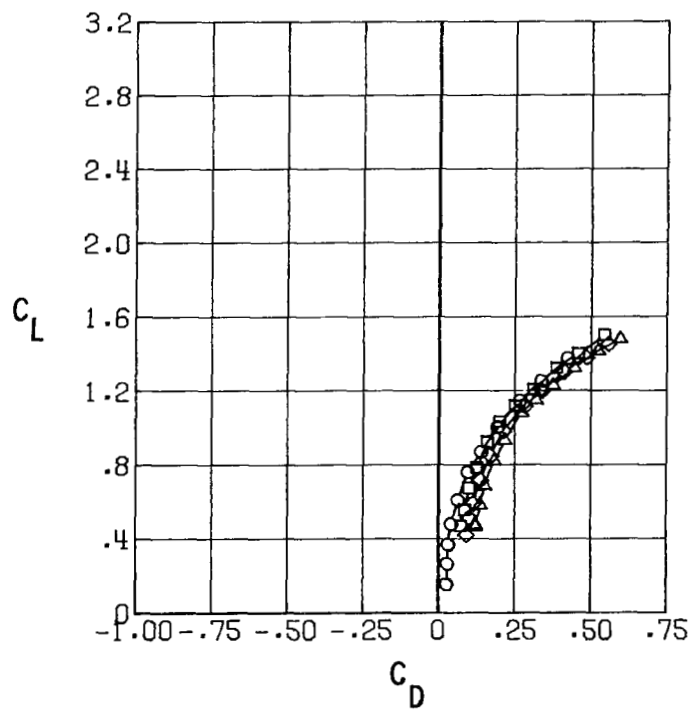
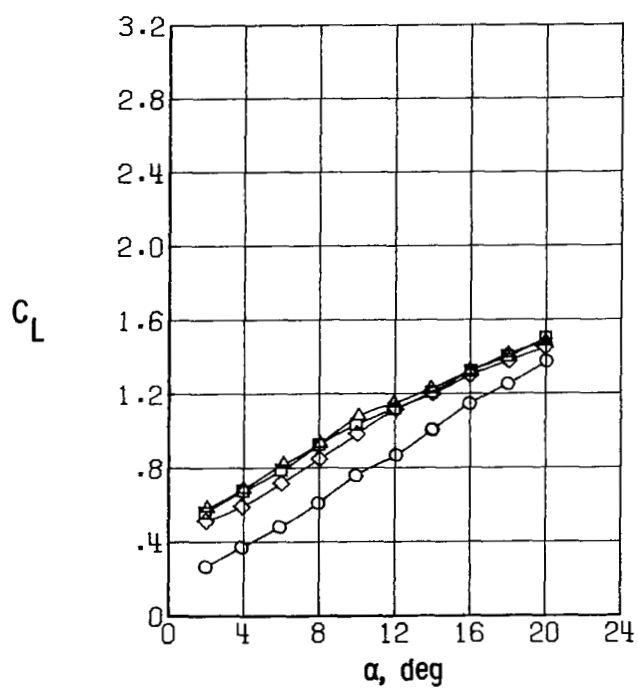
(a) $\delta_{PRI} = 0^\circ$.

Figure 16.- Effect of flap deflection on longitudinal aerodynamics of baseline modified fighter model. $C_\mu = 0$.



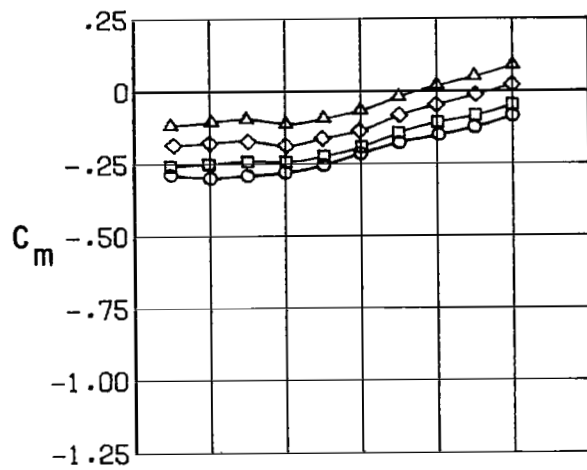
δ_f , deg

- 0/0
- 26/26
- ◇ 45/26
- △ 45/45



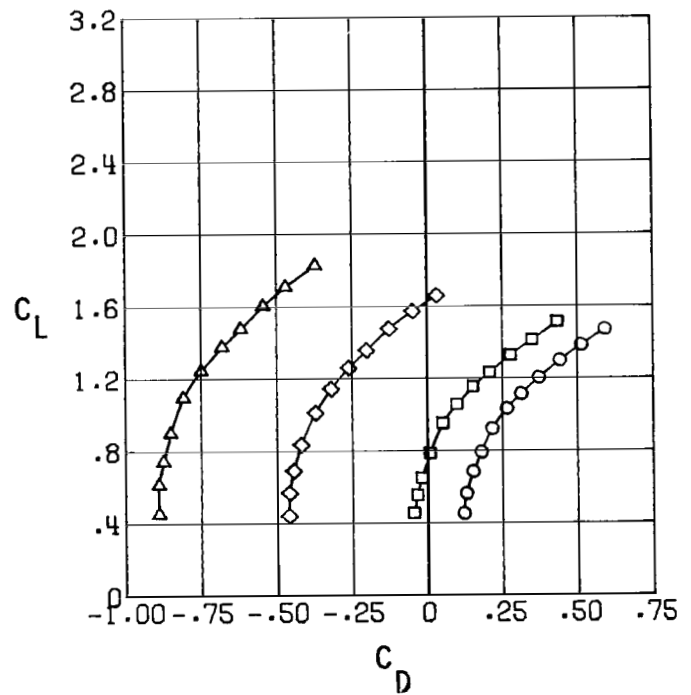
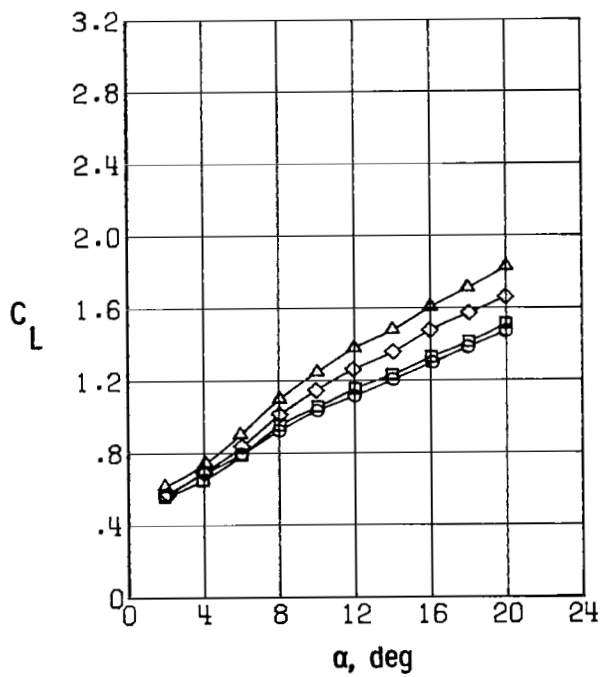
(b) $\delta_{PRI} = 45^\circ$.

Figure 16.- Concluded.



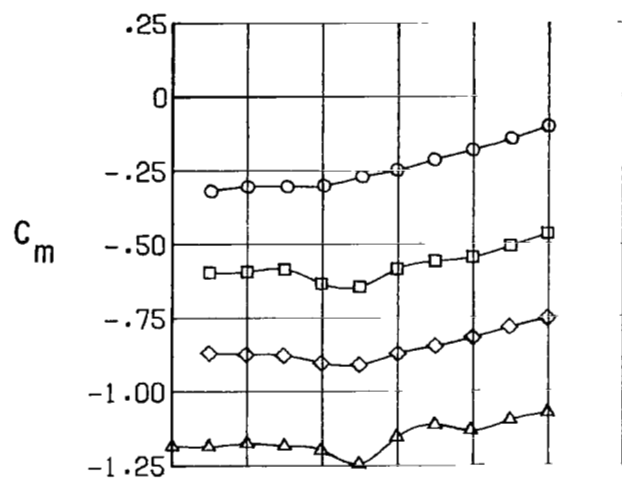
$C_{\mu, PRI}$

- 0
- .19
- ◇ .60
- △ 1.07



(a) $\delta_{PRI} = 0^\circ$.

Figure 17.- Effect of thrust coefficient on longitudinal aerodynamics of baseline modified fighter model. $\delta_f = 45^\circ/45^\circ$.



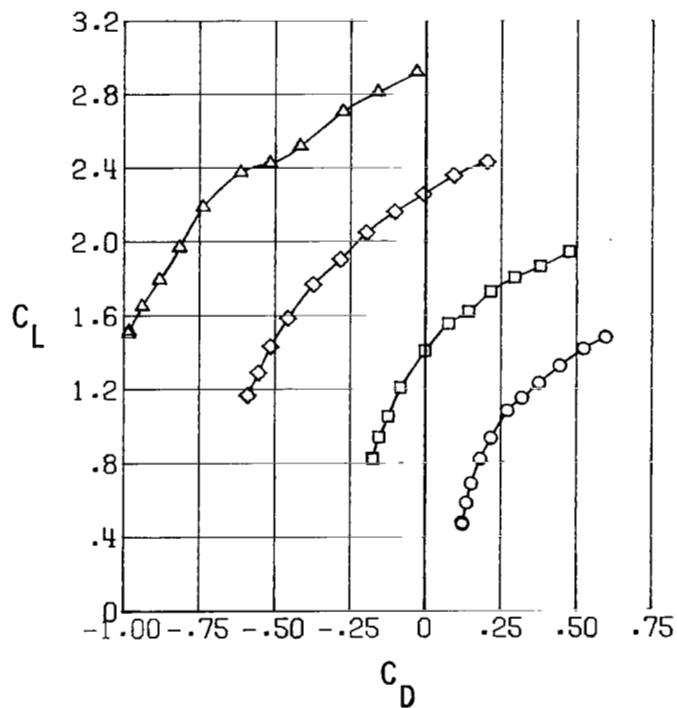
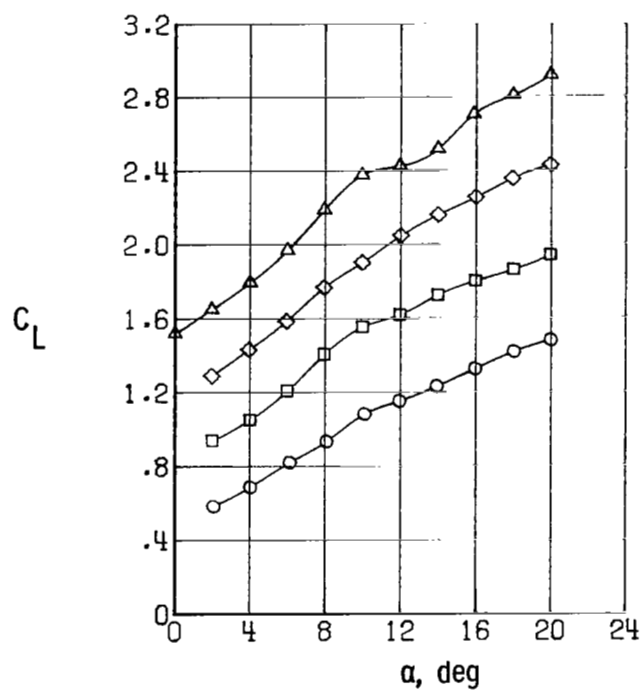
$C_{\mu, PRI}$

\circ 0

\square .48

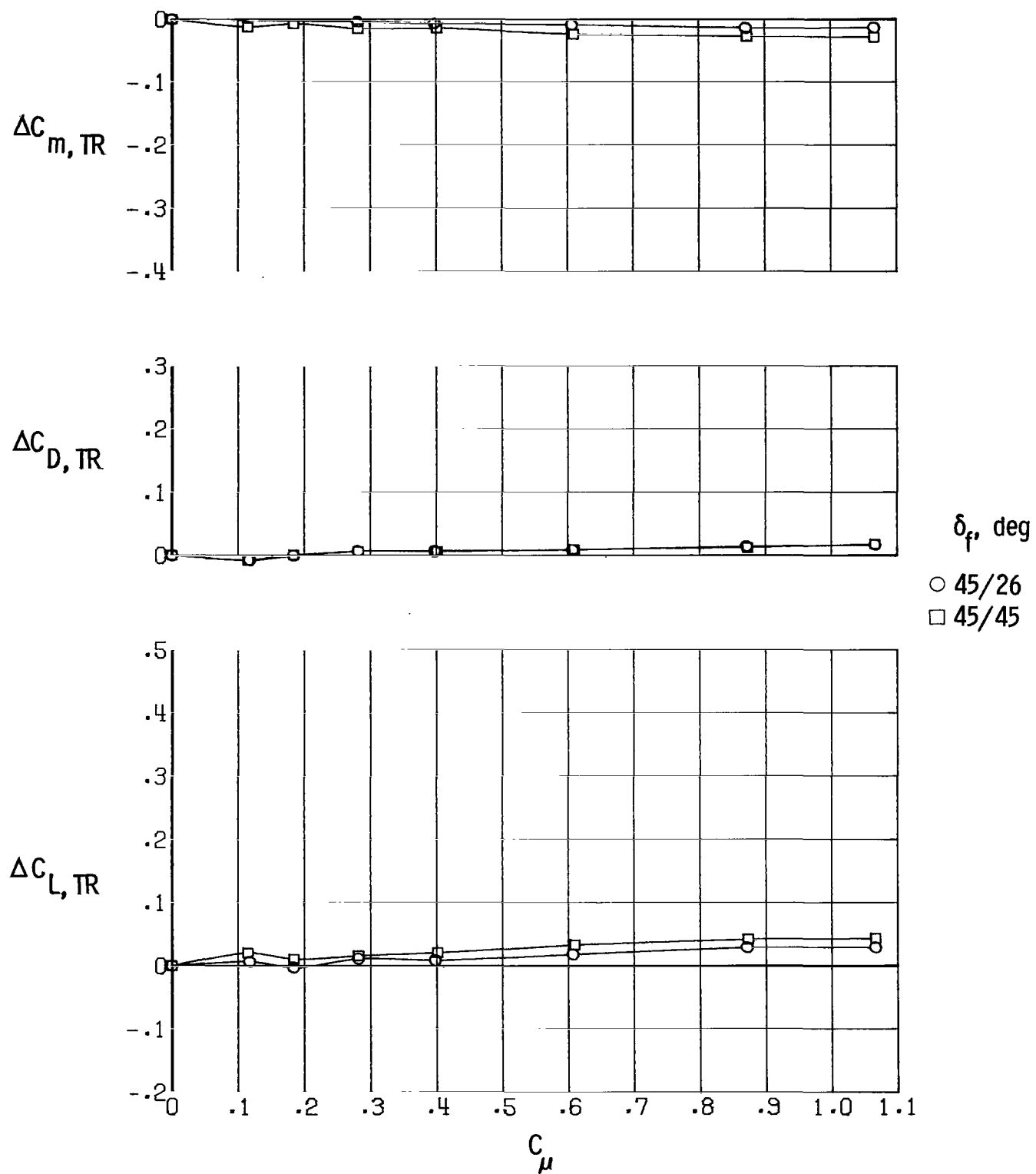
\diamond 1.01

\triangle 1.54



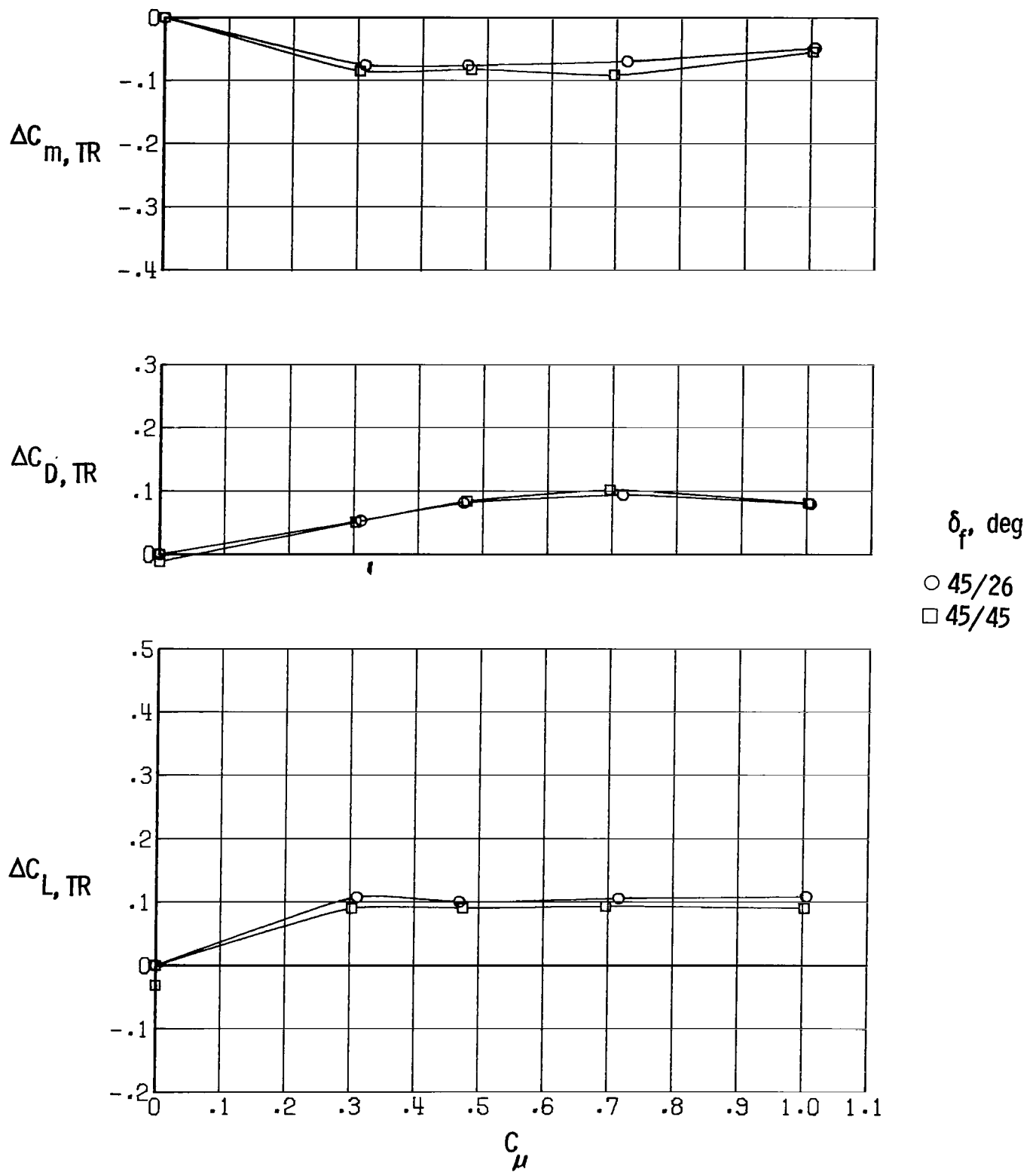
(b) $\delta_{PRI} = 45^\circ$.

Figure 17.- Concluded.



(a) $\delta_{PRI} = 0^\circ$.

Figure 18.- Induced longitudinal aerodynamics due to thrust from primary nozzles alone at two flap deflections. $\alpha = 14^\circ$.



(b) $\delta_{PRI} = 45^\circ$.

Figure 18.- Concluded.

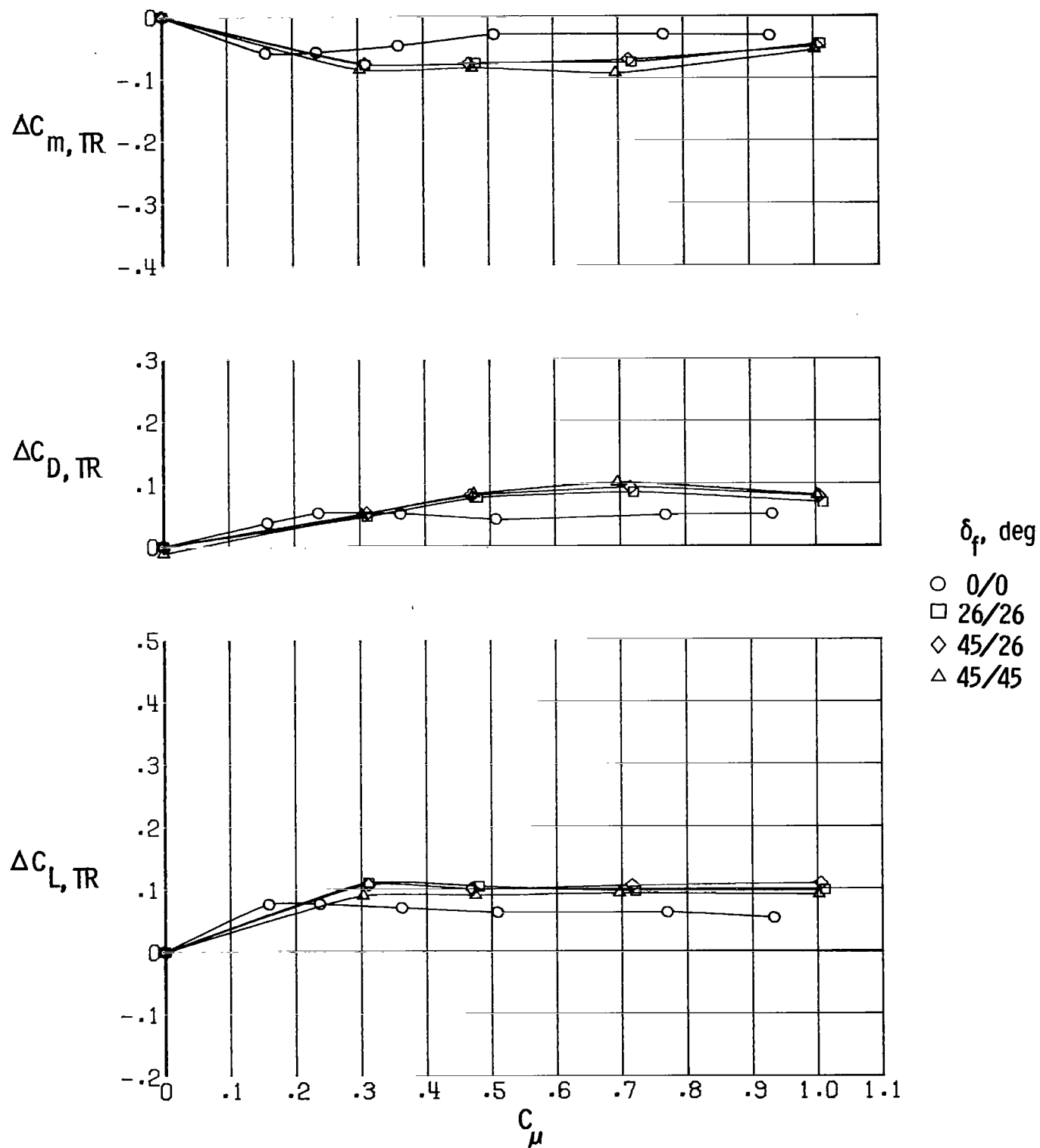
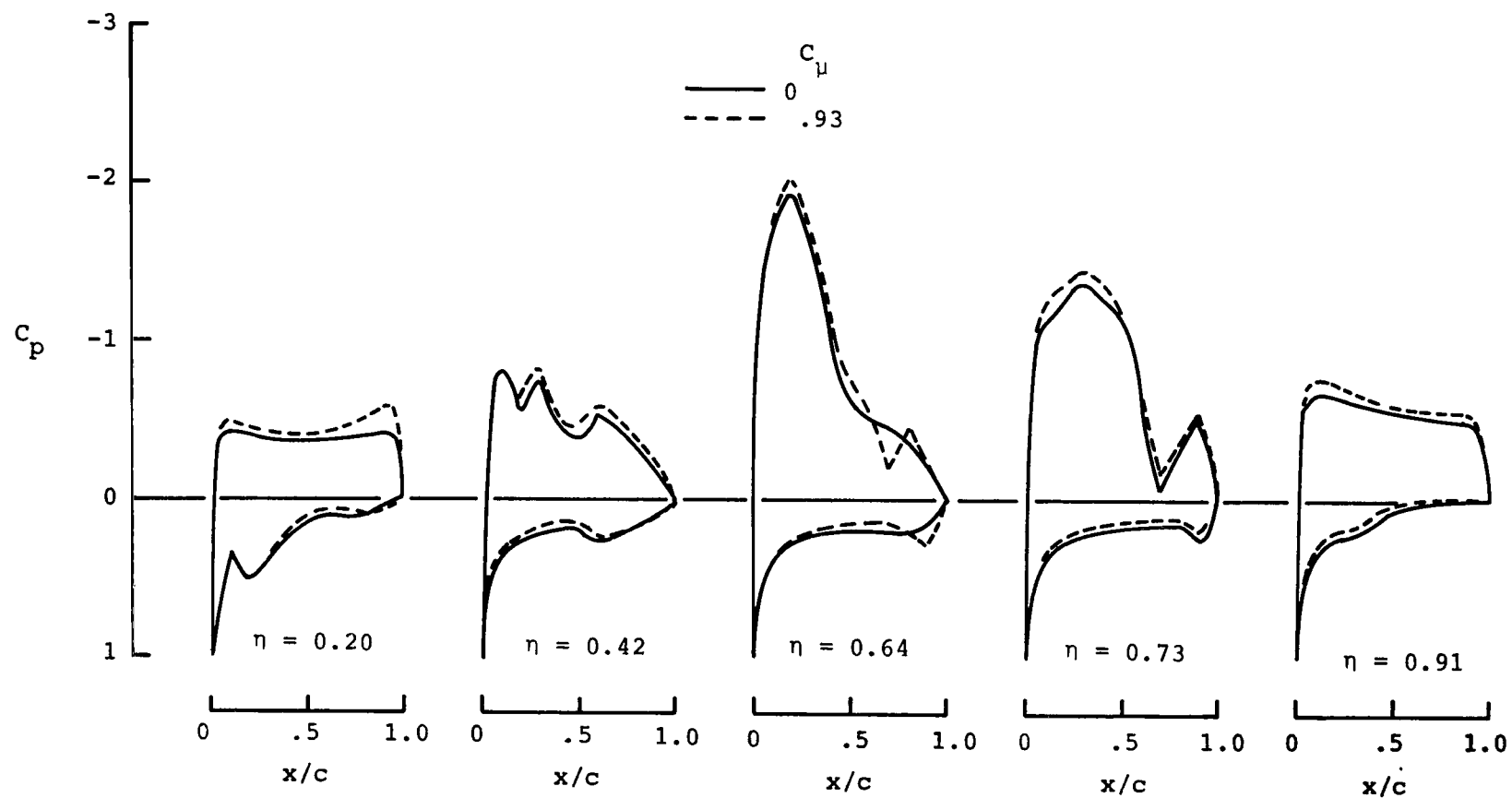
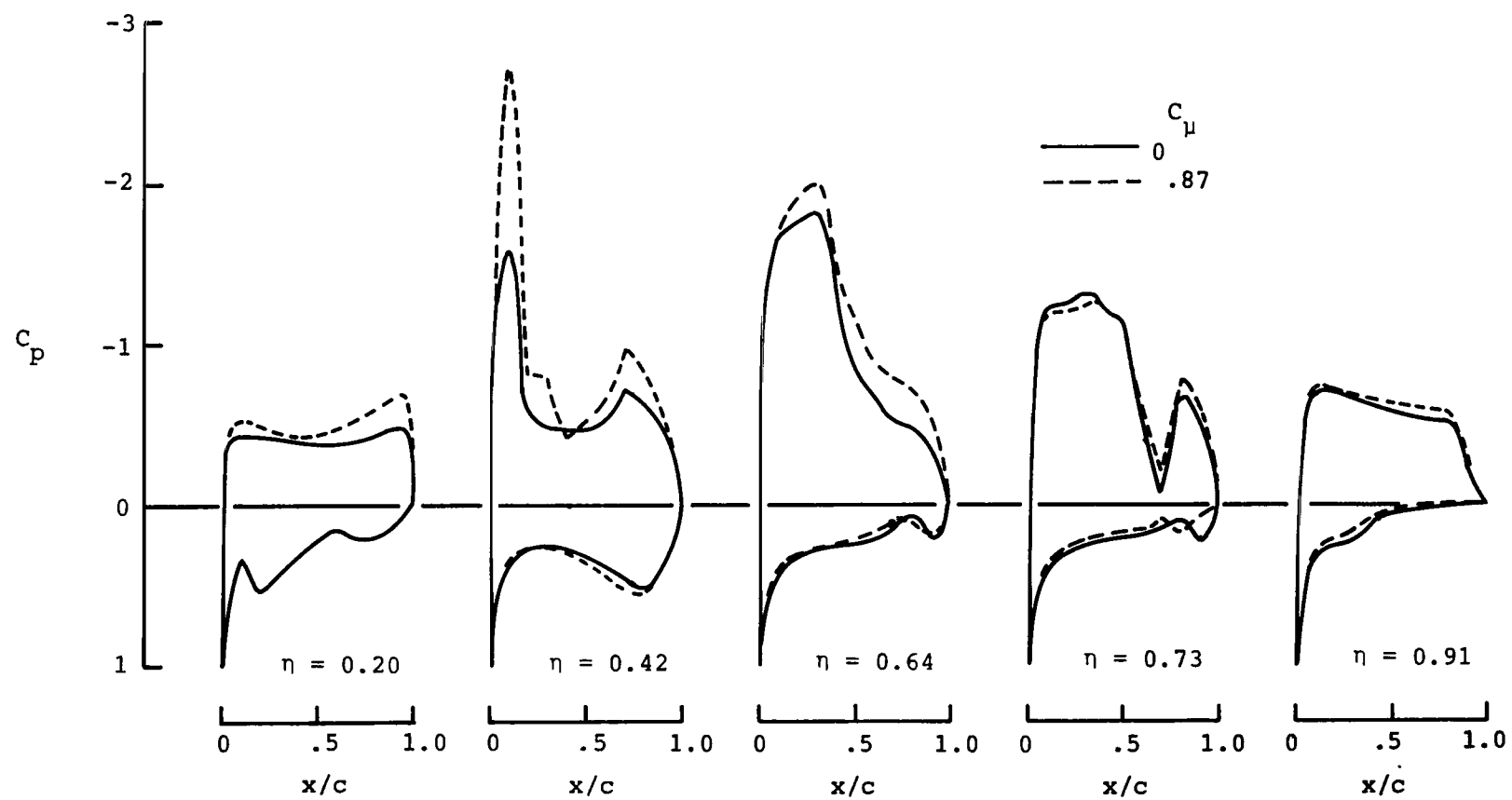


Figure 19.- Effect of flap deflection on induced longitudinal aerodynamics.
 $\delta_{PRI} = 45^\circ$; $\alpha = 14^\circ$.



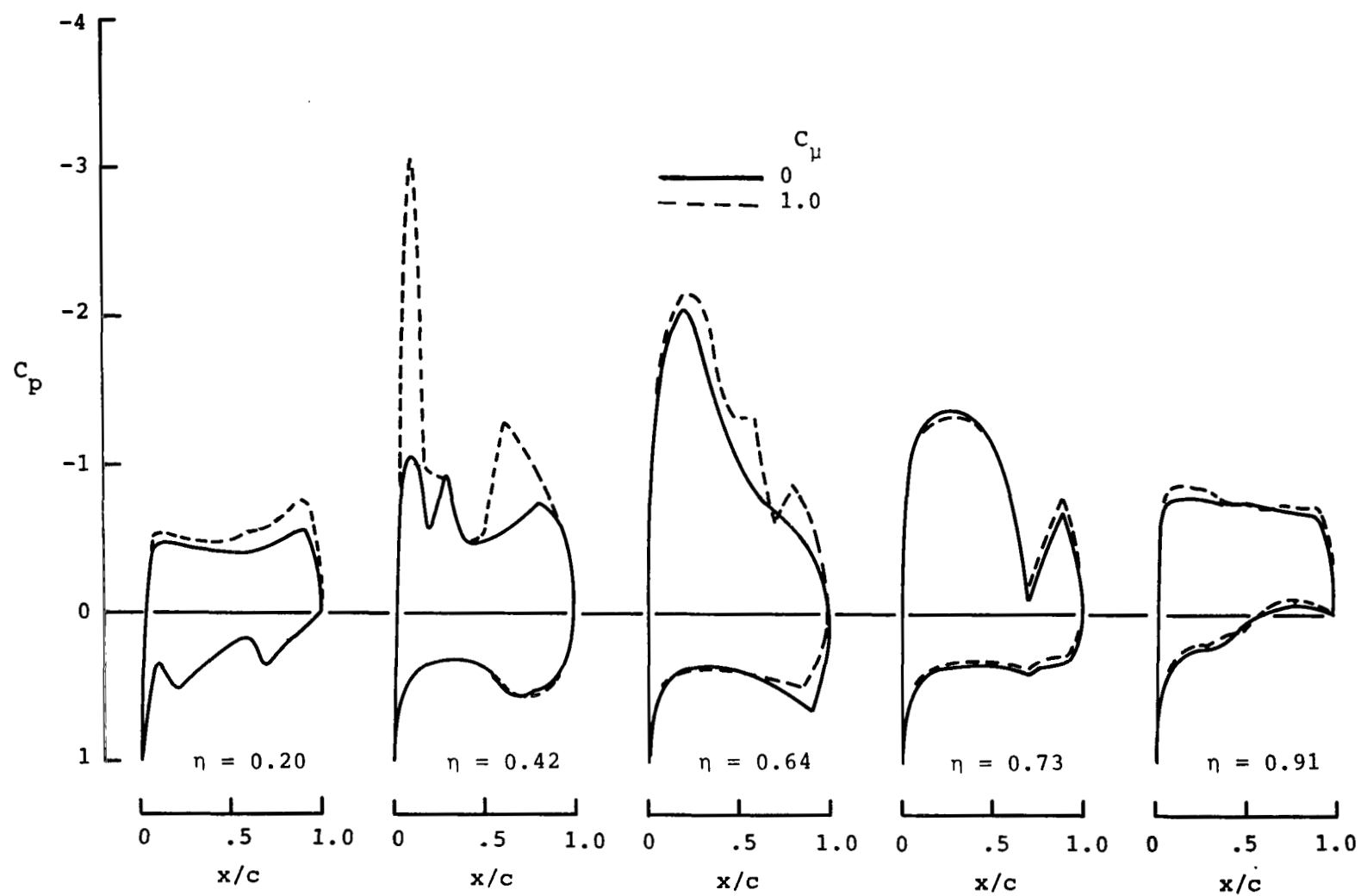
(a) $\delta_f = 0^\circ/0^\circ$.

Figure 20.- Effect of thrust from primary nozzle alone on wing surface pressures of baseline configurations.
 $\delta_{PRI} = 45^\circ$; $\alpha = 14^\circ$.



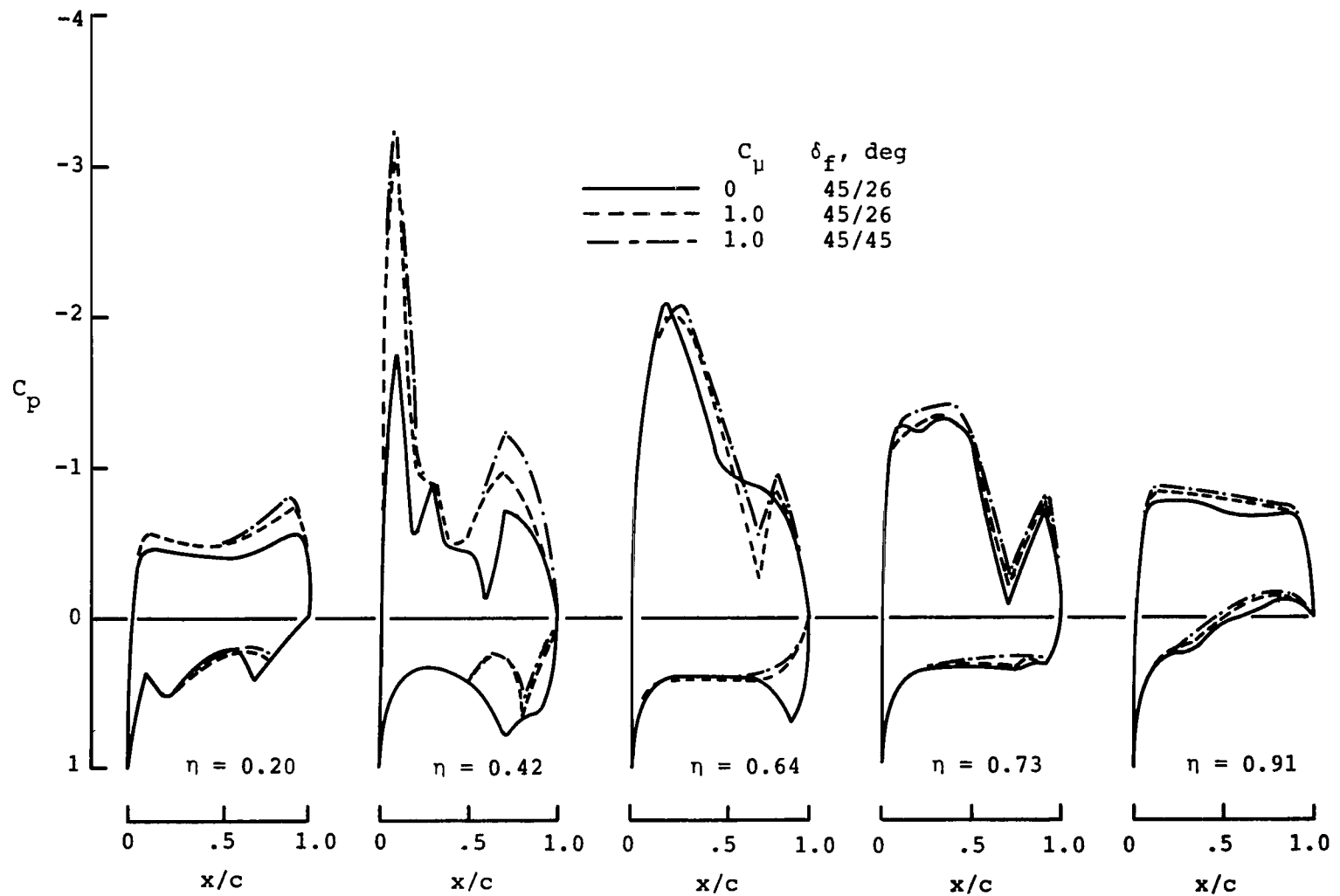
(b) $\delta_f = 26^\circ/0^\circ$.

Figure 20.- Continued.



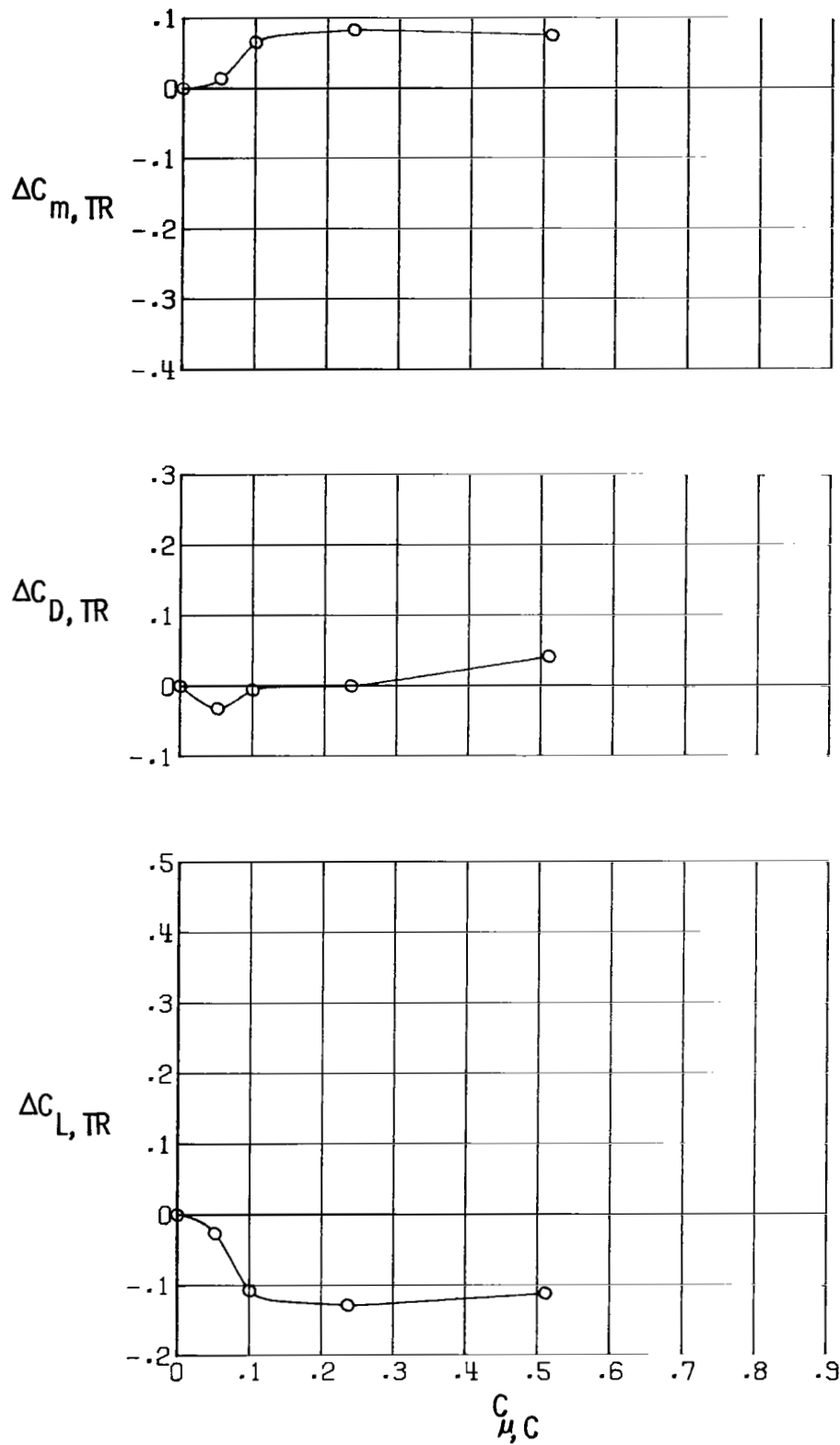
(c) $\delta_f = 26^\circ/26^\circ$.

Figure 20.- Continued.



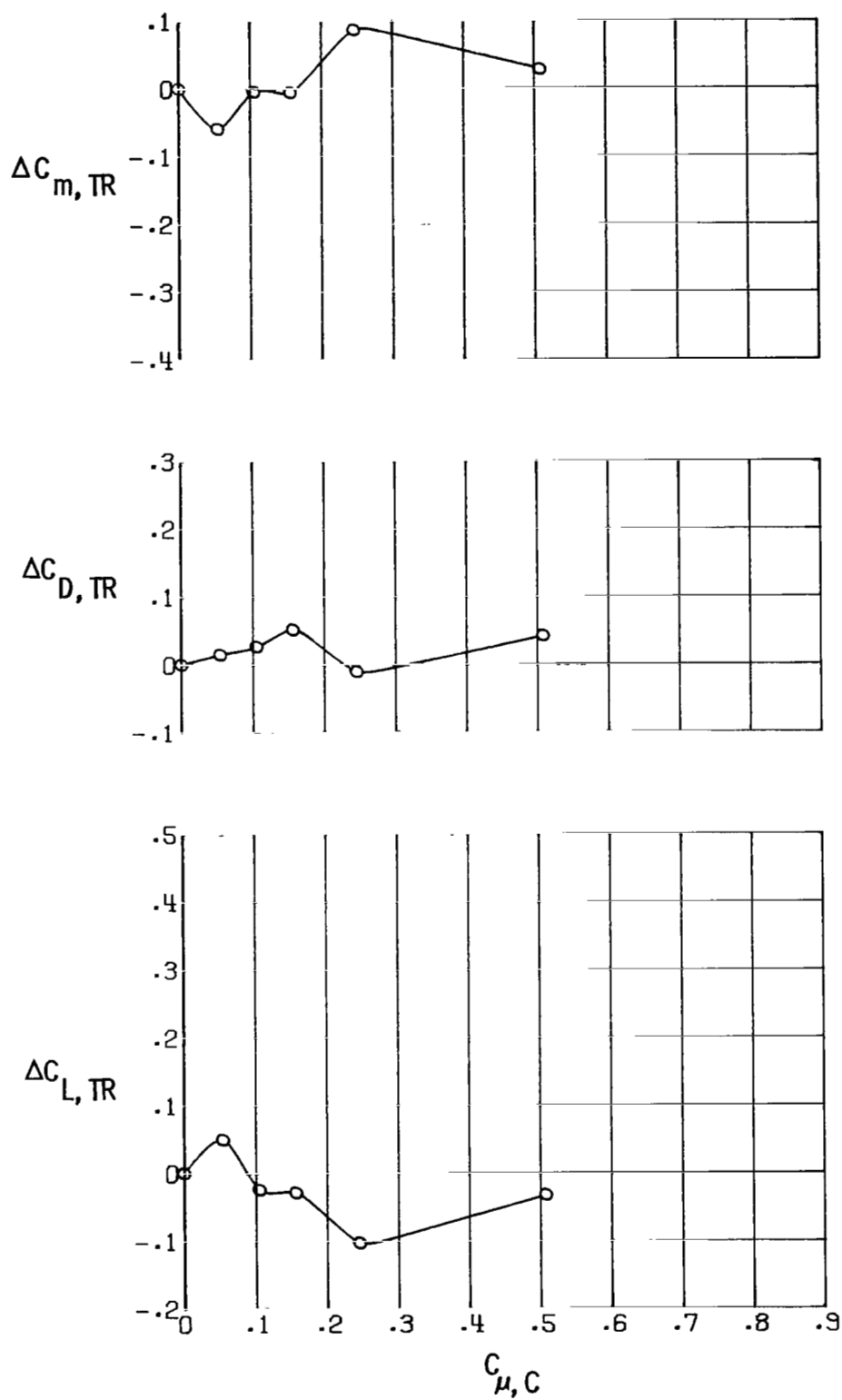
(d) $\delta_f = 45^\circ/26^\circ$ and $45^\circ/45^\circ$.

Figure 20.- Concluded.



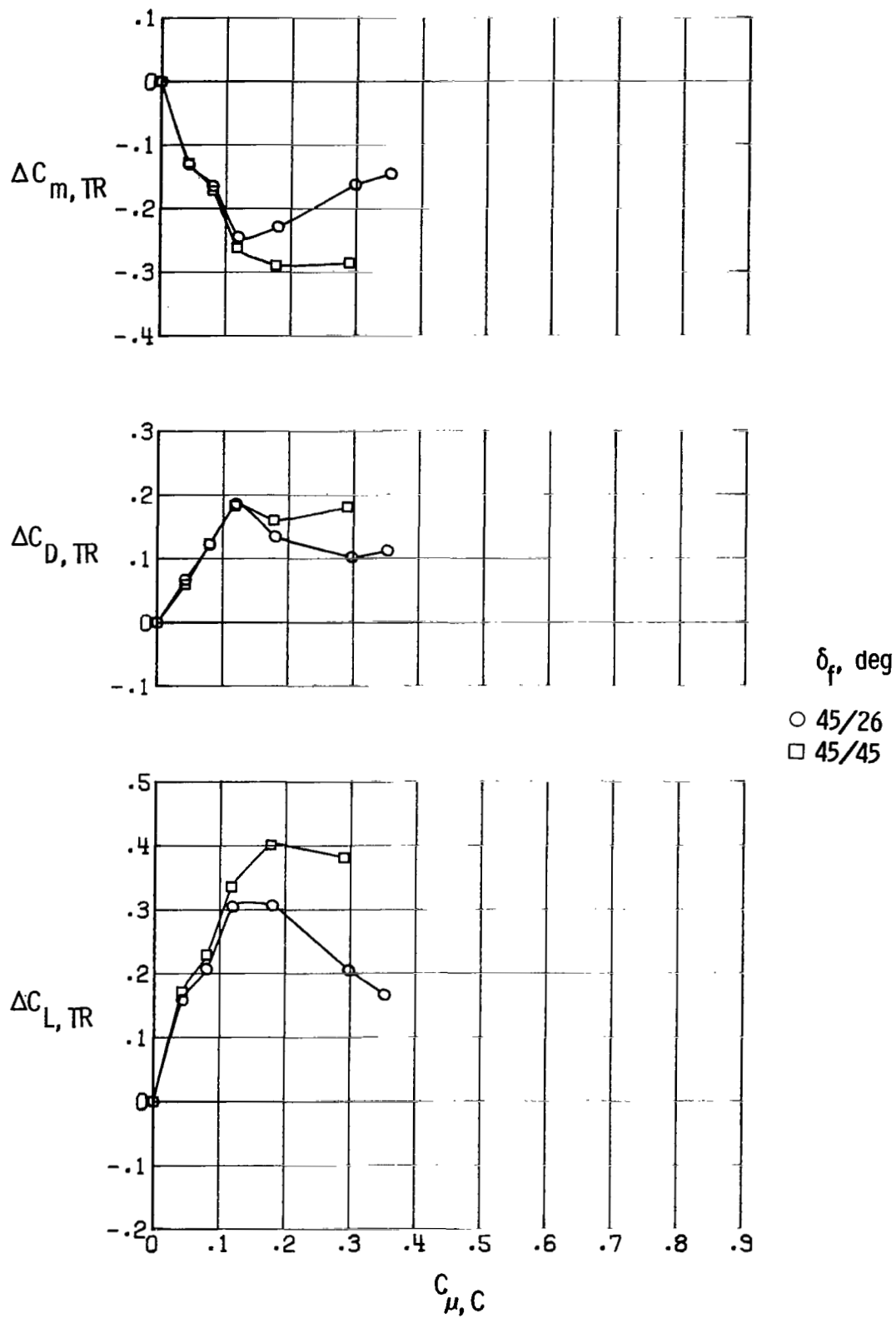
(a) Cascade 1. $\delta_f = 45^\circ/26^\circ$; $A_{e,C}/A_{e,PRI} = 0.2$; $\Lambda_C = -30^\circ$.

Figure 21.- Induced longitudinal aerodynamics for cascade configurations. $\alpha = 14^\circ$.



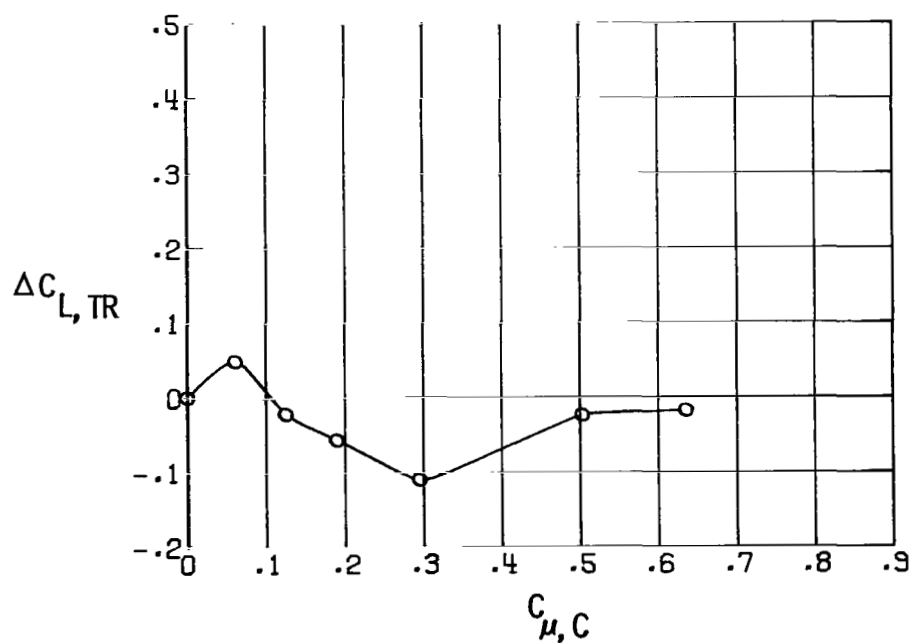
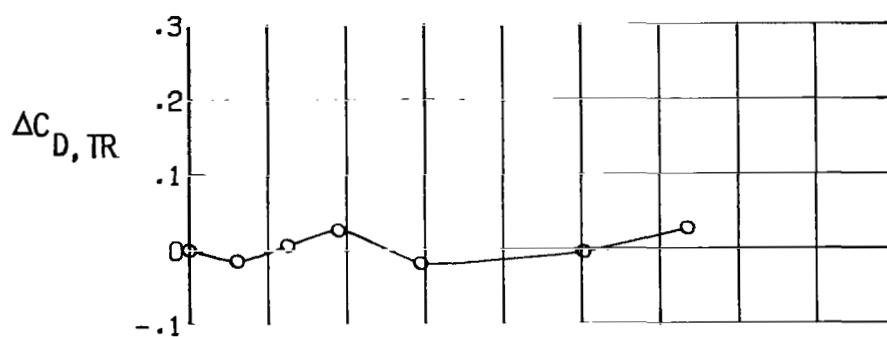
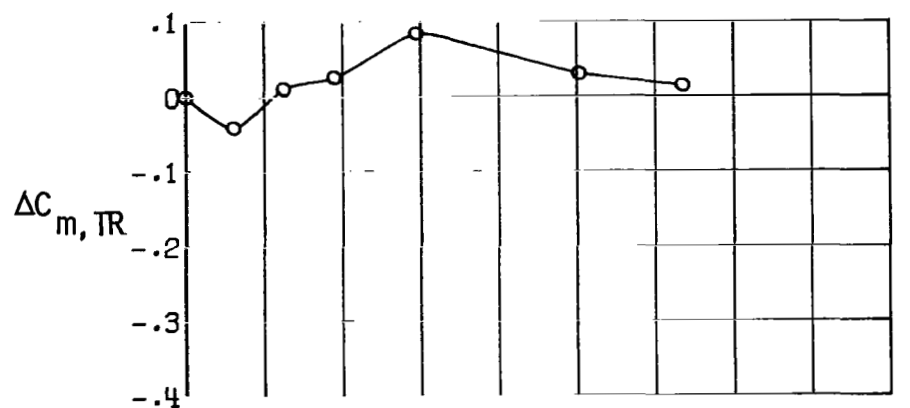
(b) Cascade 2. $\delta_f = 45^\circ/26^\circ$; $A_{e,C}/A_{e,PRI} = 0.2$; $\Lambda_C = 0^\circ$.

Figure 21.- Continued.



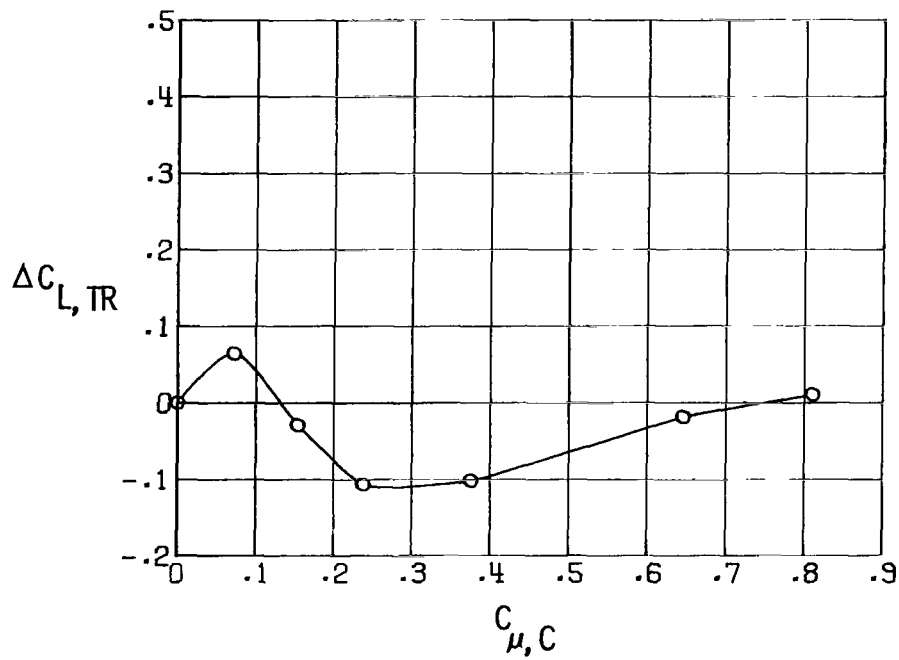
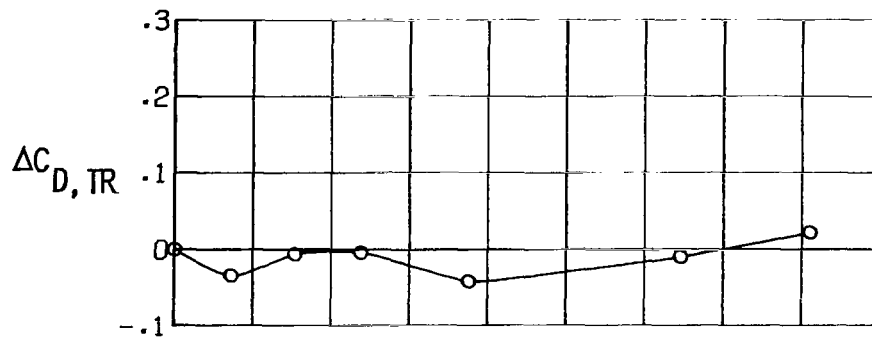
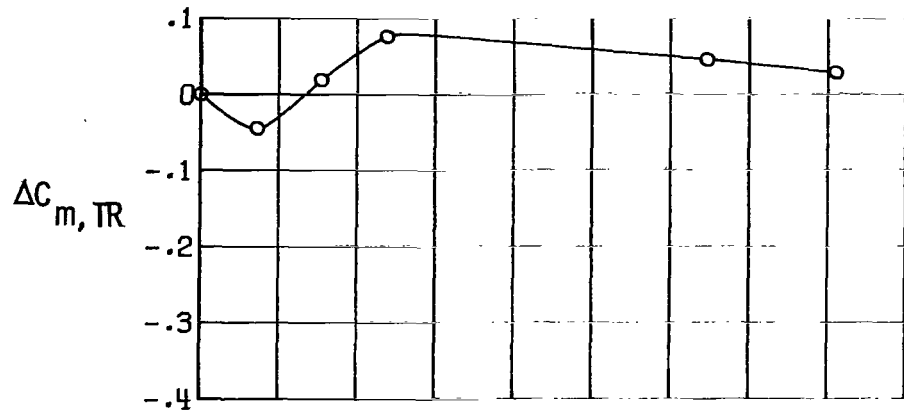
(c) Cascade 3. $A_{e,C}/A_{e,PRI} = 0.2$; $\Lambda_C = 30^\circ$.

Figure 21.- Continued.



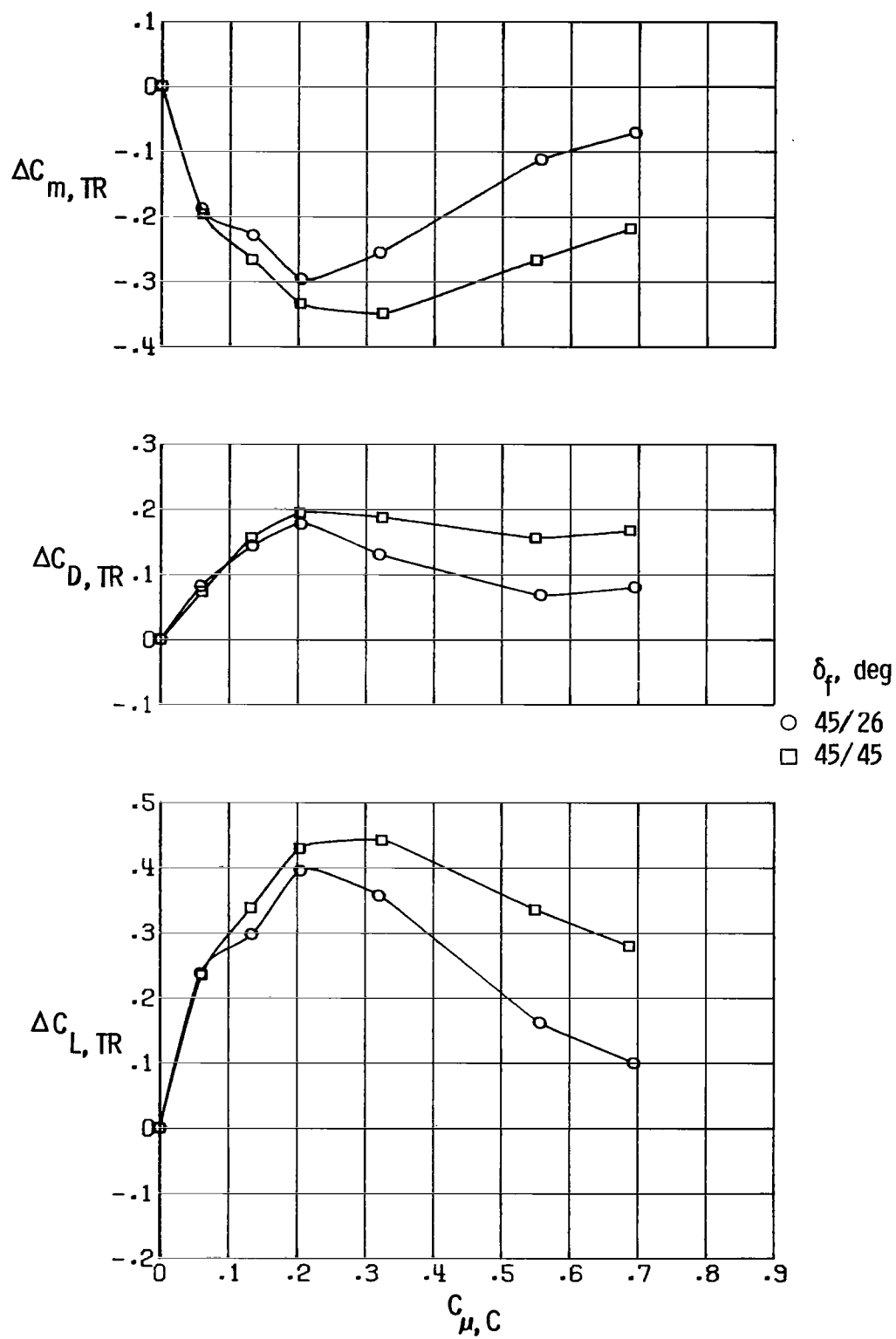
(d) Cascade 4. $\delta_f = 45^\circ/26^\circ$; $A_{e,C}/A_{e,PRI} = 0.30$; $\Lambda_C = 0^\circ$.

Figure 21.- Continued.



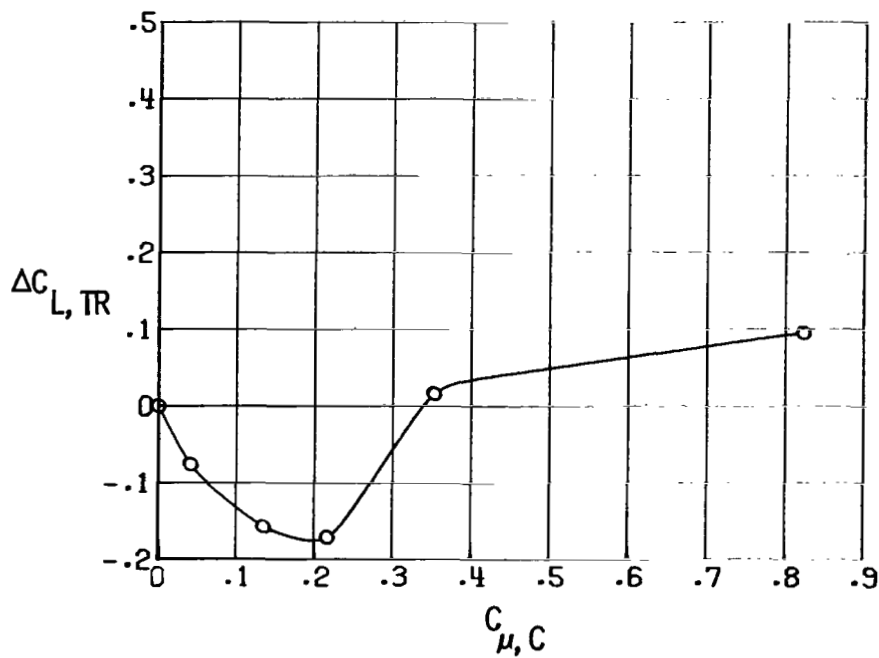
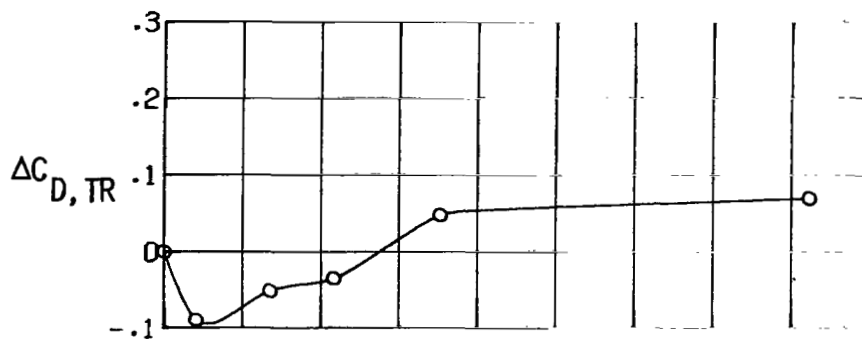
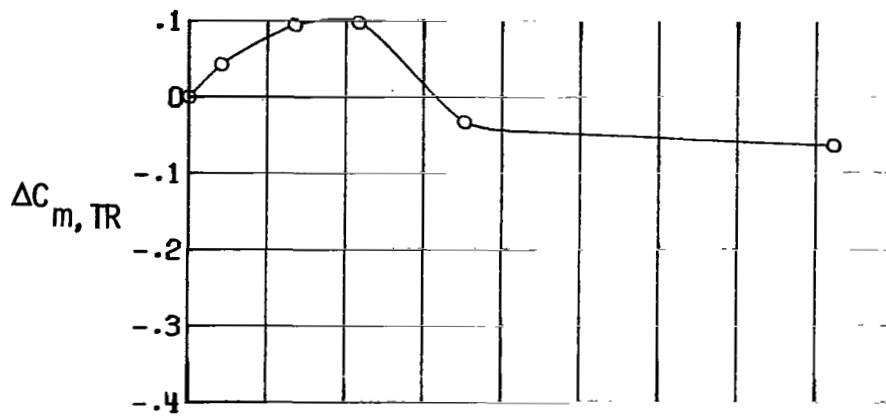
(e) Cascade 5. $\delta_f = 45^\circ/26^\circ$; $A_{e,C}/A_{e,PRI} = 0.45$; $\Lambda_C = 0^\circ$.

Figure 21.- Continued.



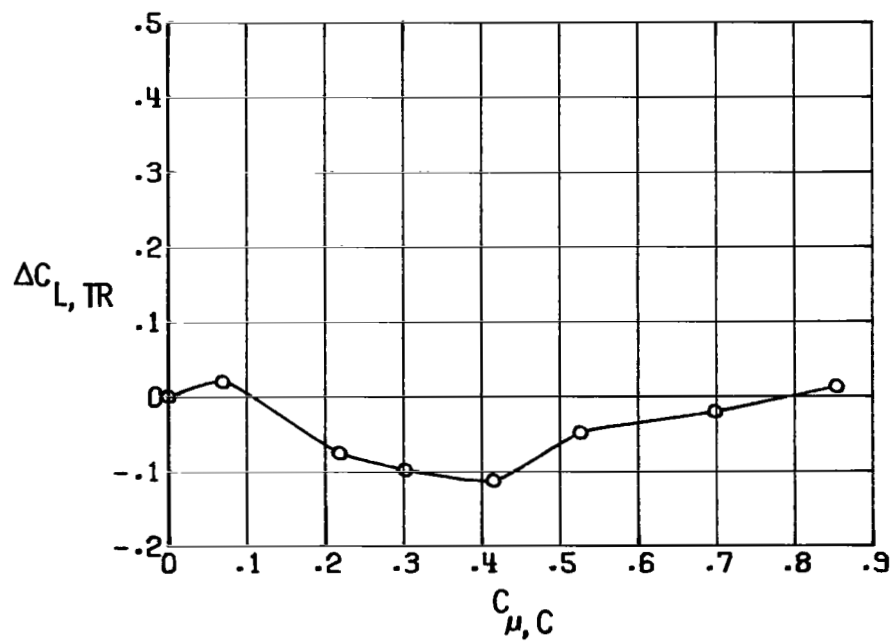
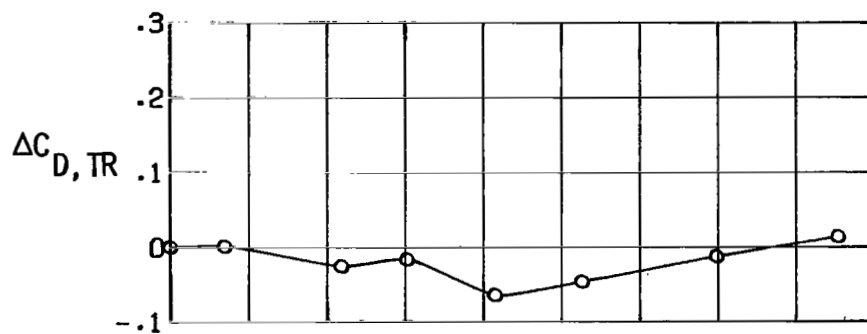
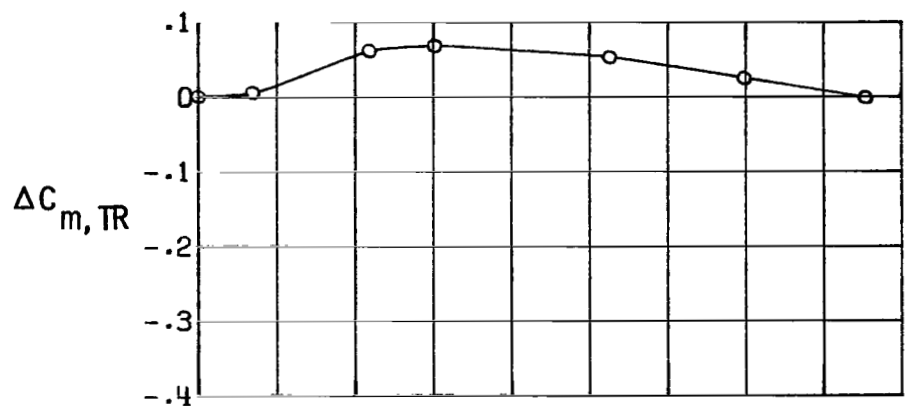
(f) Cascade 6. $A_{e,C}/A_{e,PRI} = 0.45$; $\Lambda_C = 30^\circ$.

Figure 21.- Continued.



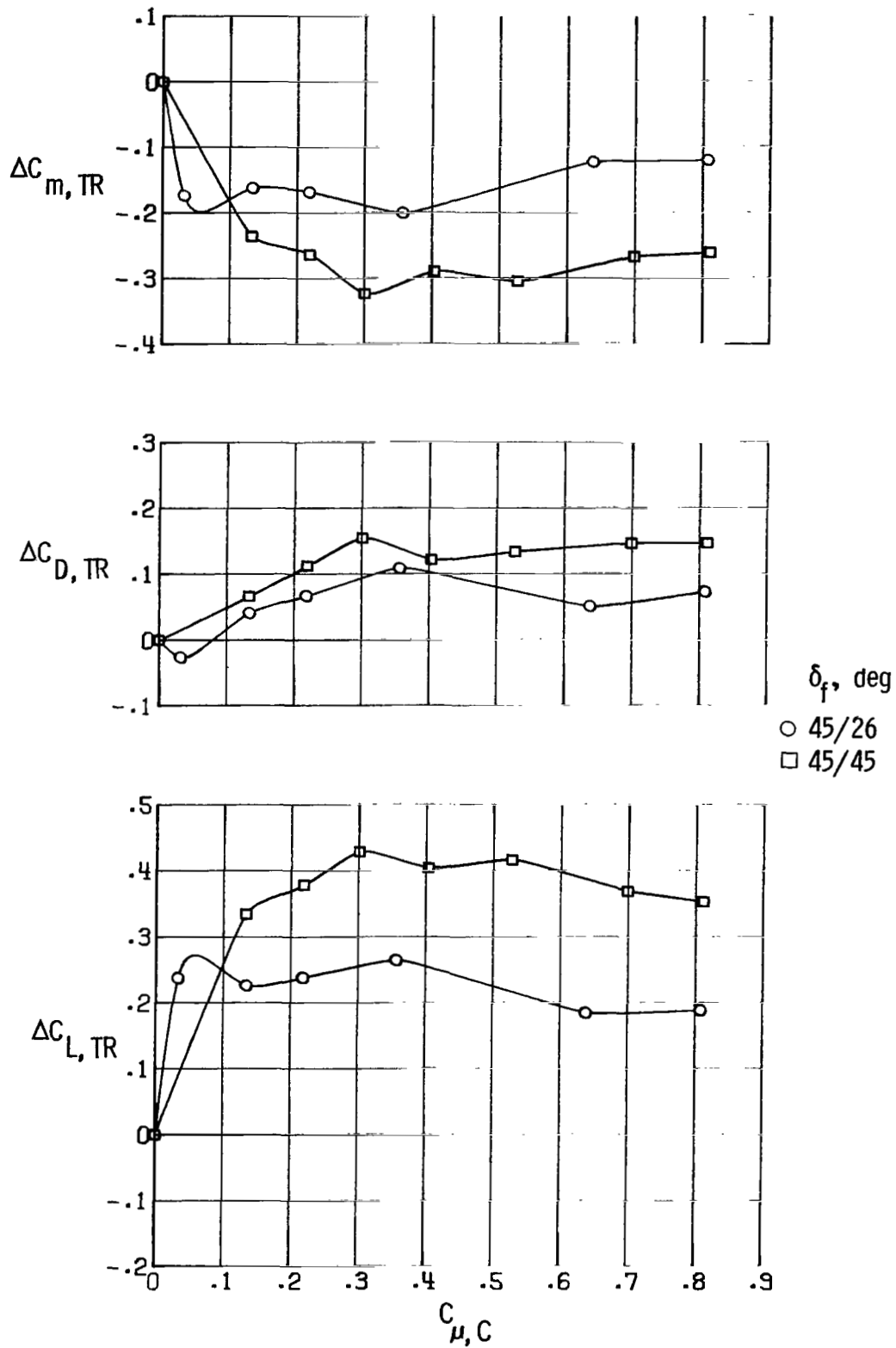
(g) Cascade 7. $\delta_f = 45^\circ/26^\circ$; $A_{e,C}/A_{e,PRI} = 0.60$; $\Lambda_C = -30^\circ$.

Figure 21.- Continued.



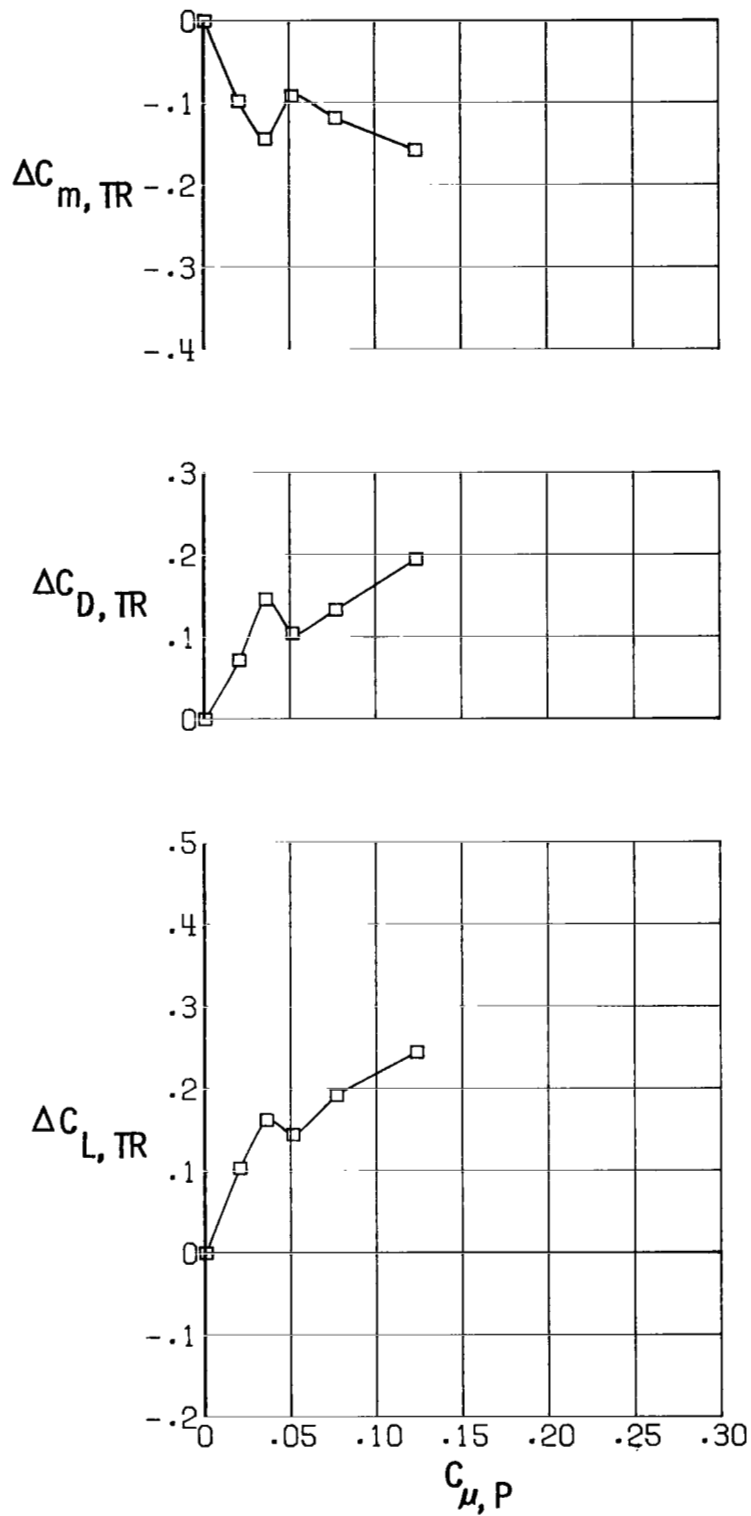
(h) Cascade 8. $\delta_f = 45^\circ/26^\circ$; $A_{e,C}/A_{e,PRI} = 0.60$; $\Lambda_C = 0^\circ$.

Figure 21.- Continued.



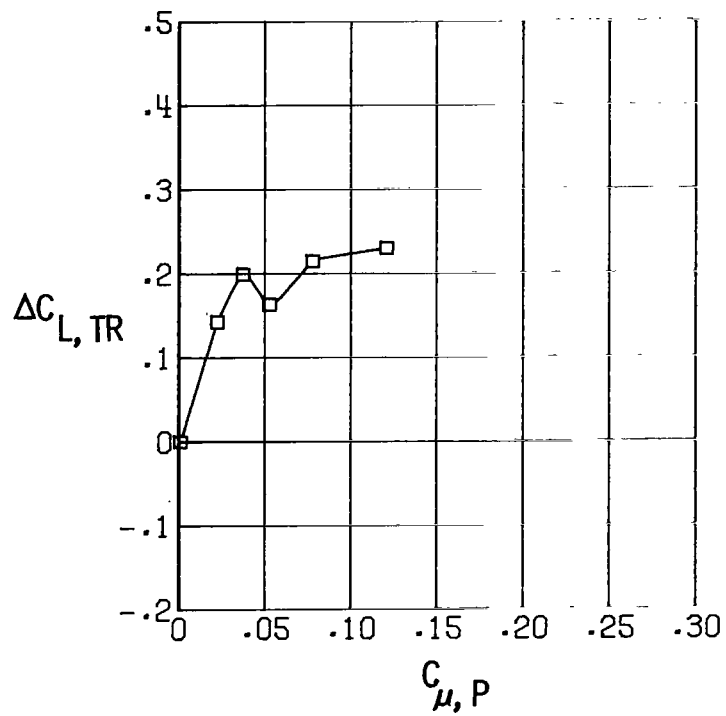
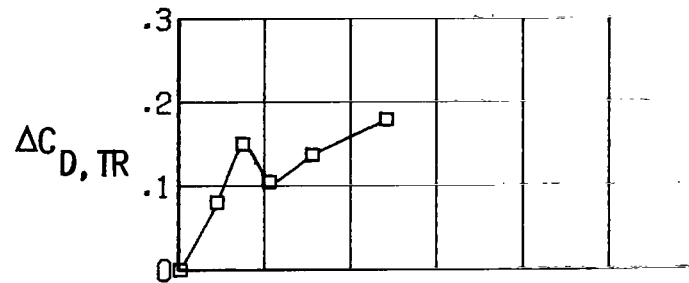
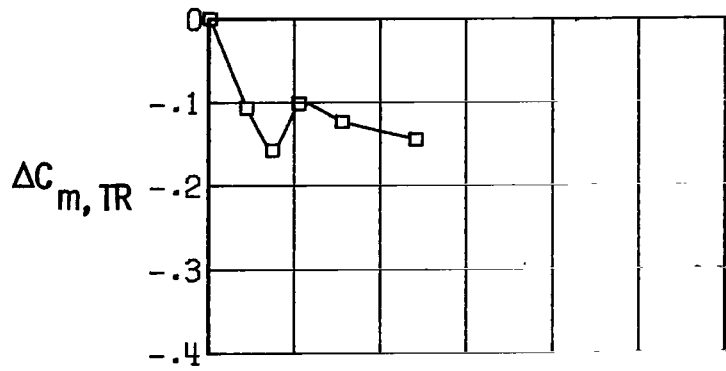
(i) Cascade 9. $A_{e,C}/A_{e,PRI} = 0.60$; $\Lambda_C = 30^\circ$.

Figure 21.- Concluded.



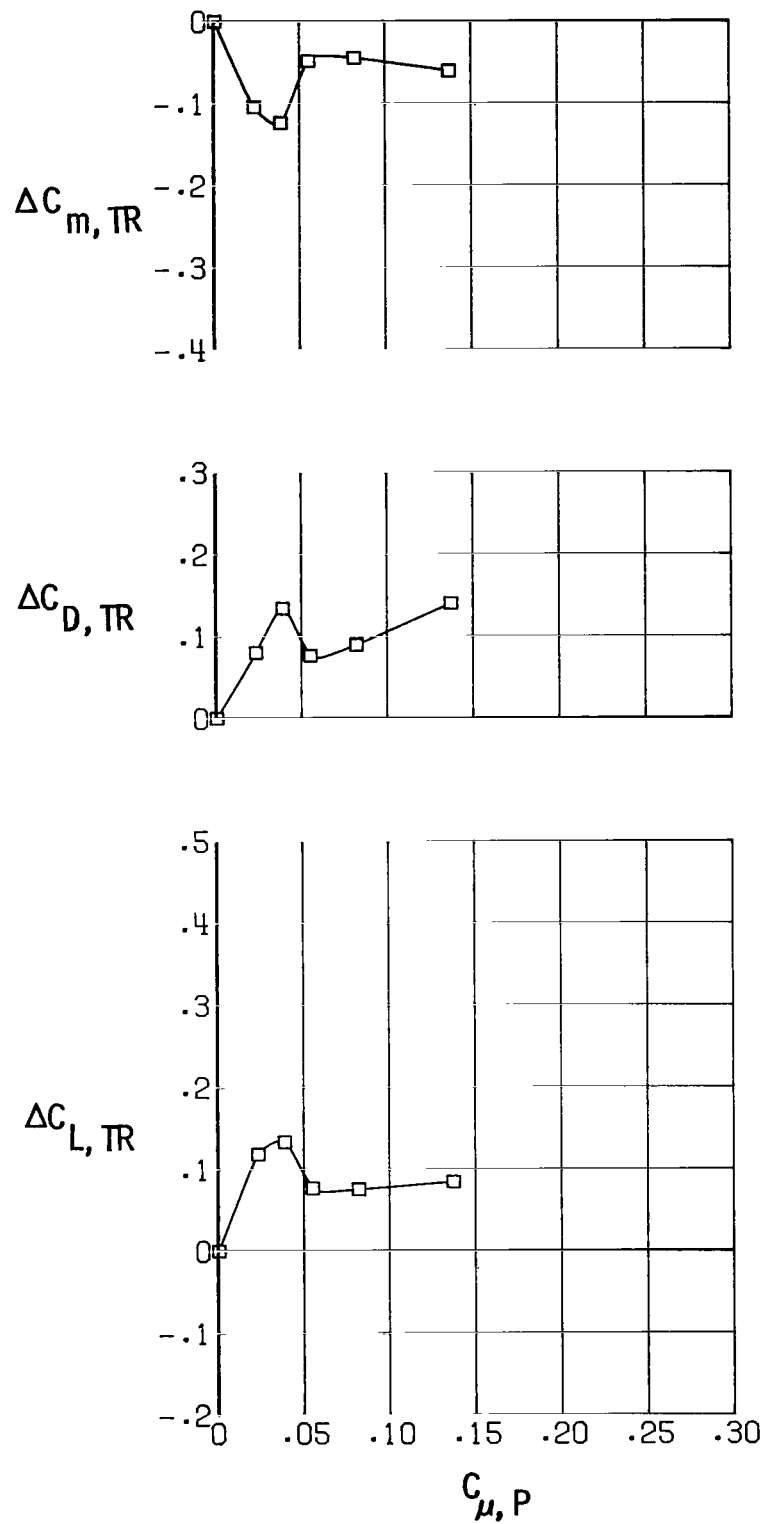
(a) Port 1 at location A. $\delta_f = 45^\circ/45^\circ$;
 $A_{e, P}/A_{e, PRI} = 0.05$; $\Lambda_P = 30^\circ$.

Figure 22.- Induced longitudinal aerodynamics for port configurations. $\alpha = 14^\circ$.



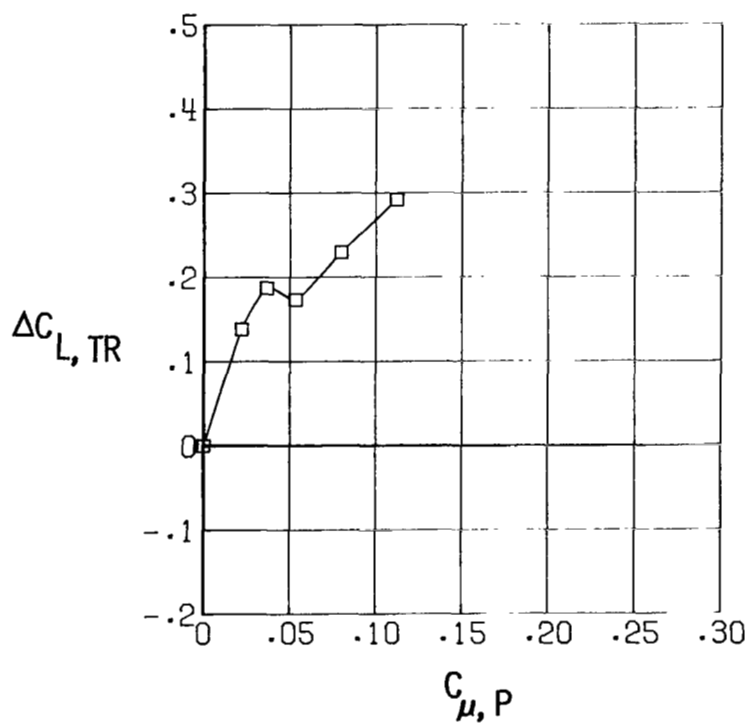
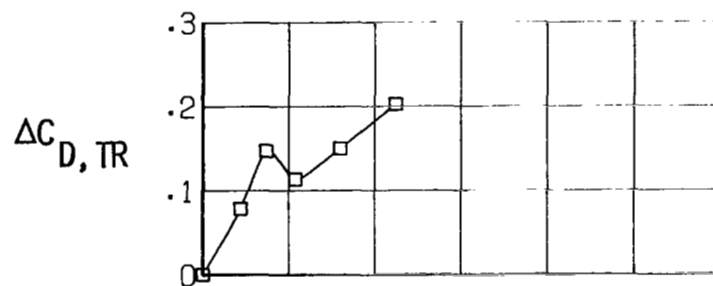
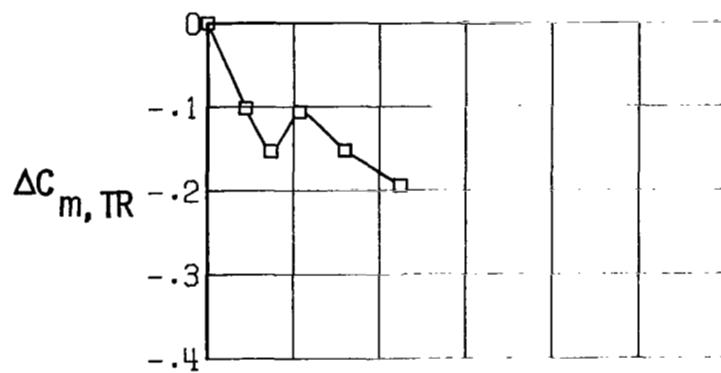
(b) Port 2 at location A. $\delta_f = 45^\circ/45^\circ$;
 $A_{e,P}/A_{e,PRI} = 0.05$; $\Lambda_P = 45^\circ$.

Figure 22.- Continued.



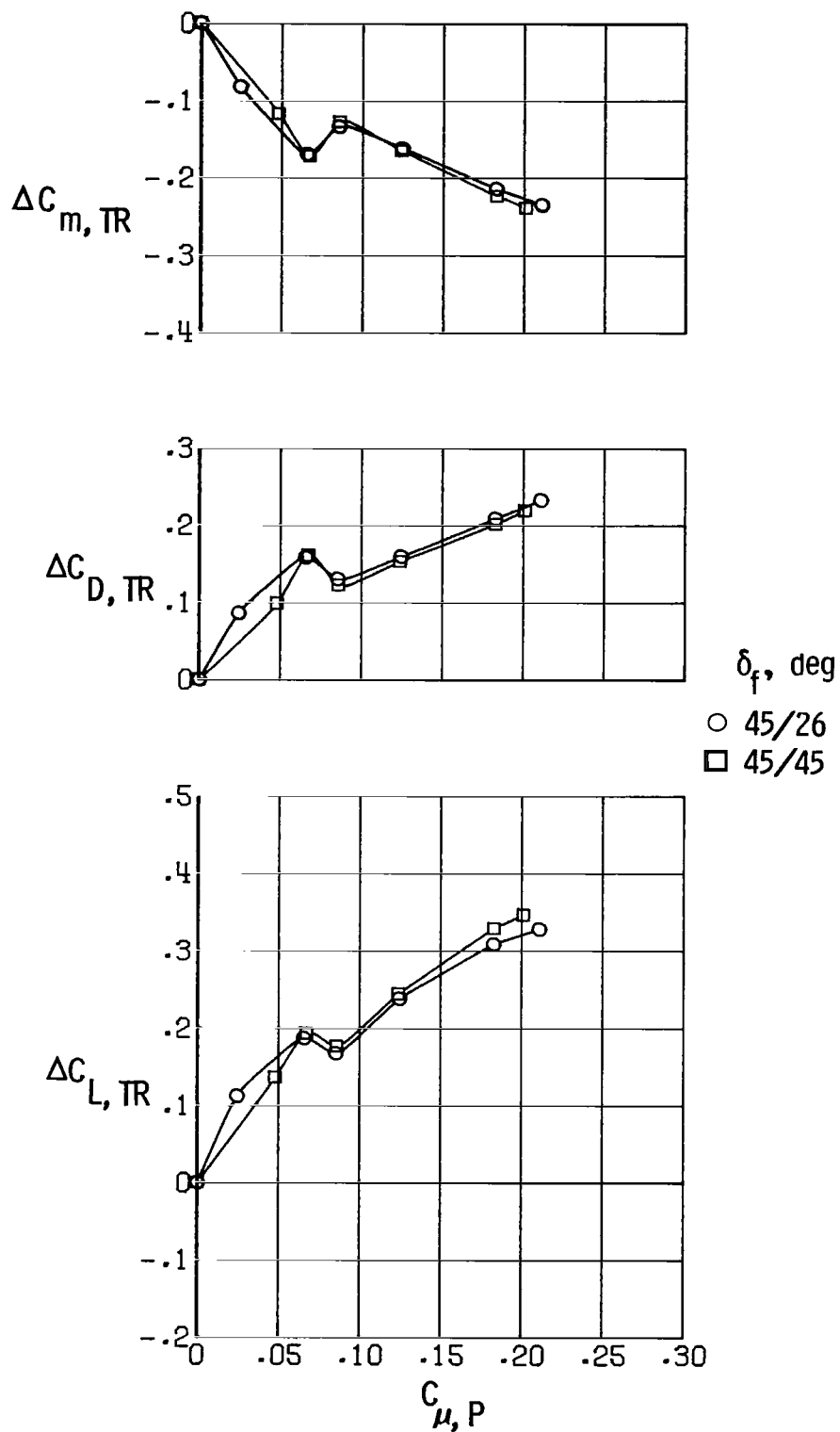
(c) Port 3 at location A. $\delta_F = 45^\circ/45^\circ$;
 $A_{e,P}/A_{e,PRI} = 0.05$; $\Lambda_P = 60^\circ$.

Figure 22.- Continued.



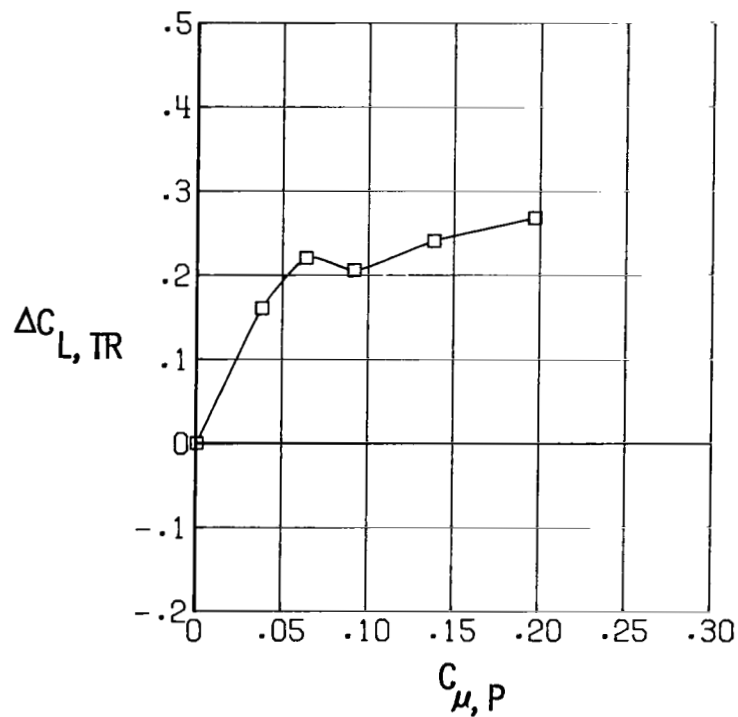
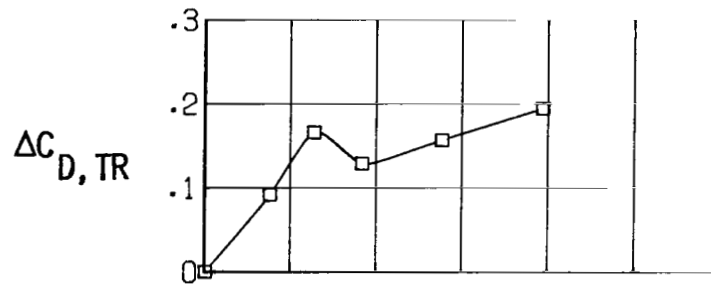
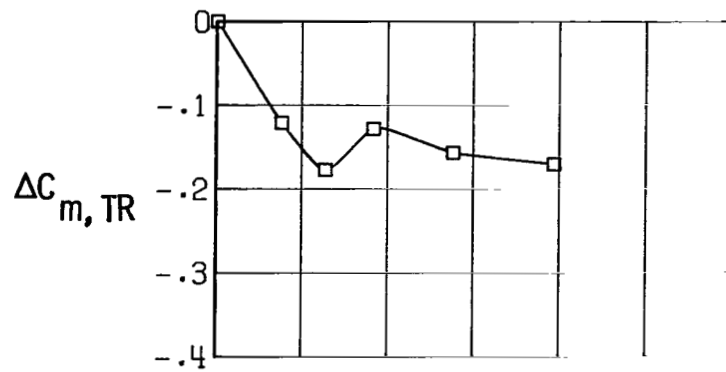
(d) Port 4 at location B. $\delta_f = 45^\circ/45^\circ$;
 $A_{e,P}/A_{e,PRI} = 0.05$; $\Lambda_P = 30^\circ$.

Figure 22.- Continued.



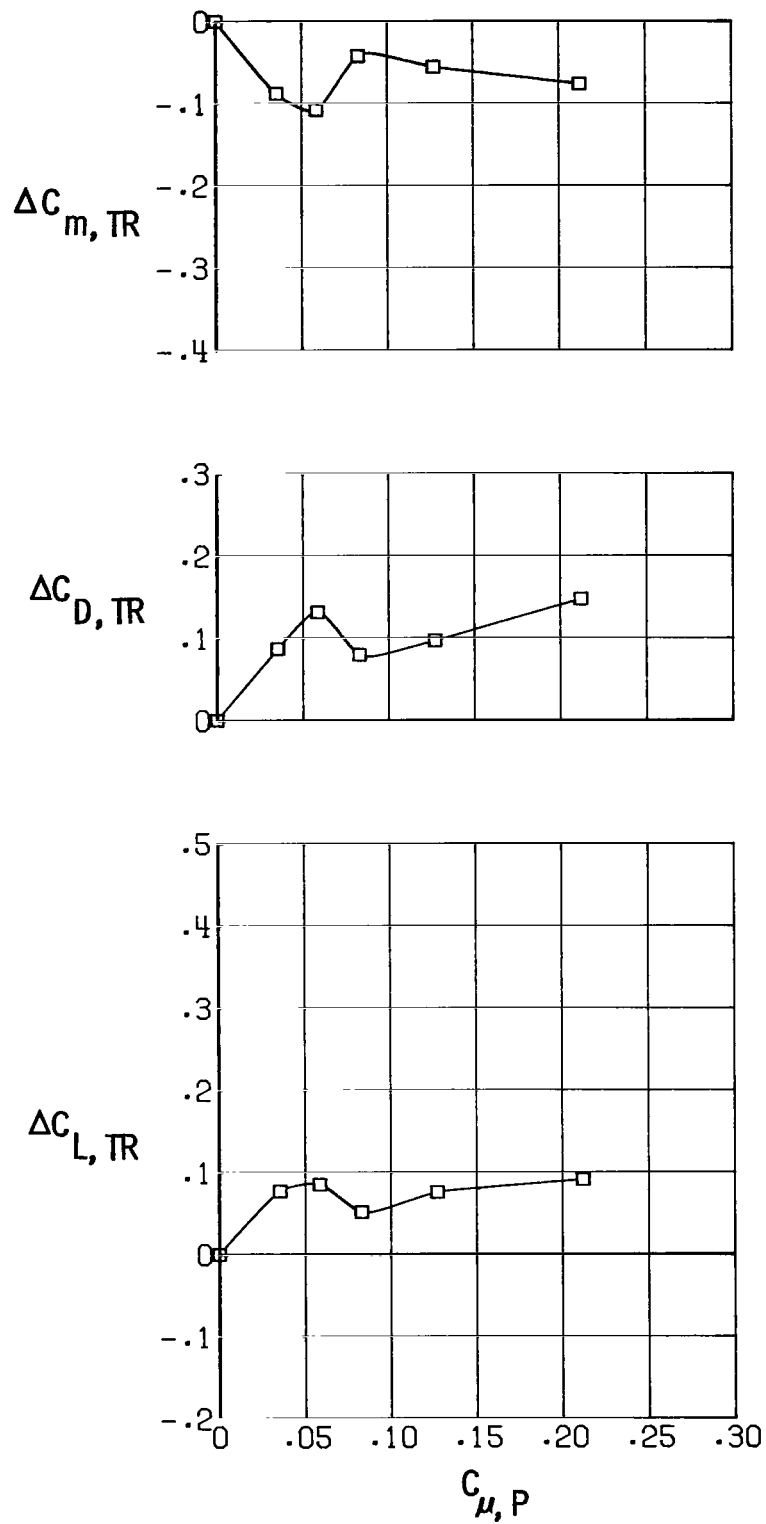
(e) Port 5 at location B. $A_{e,P}/A_{e,PRI} = 0.10$;
 $\Lambda_P = 30^\circ$.

Figure 22.- Continued.



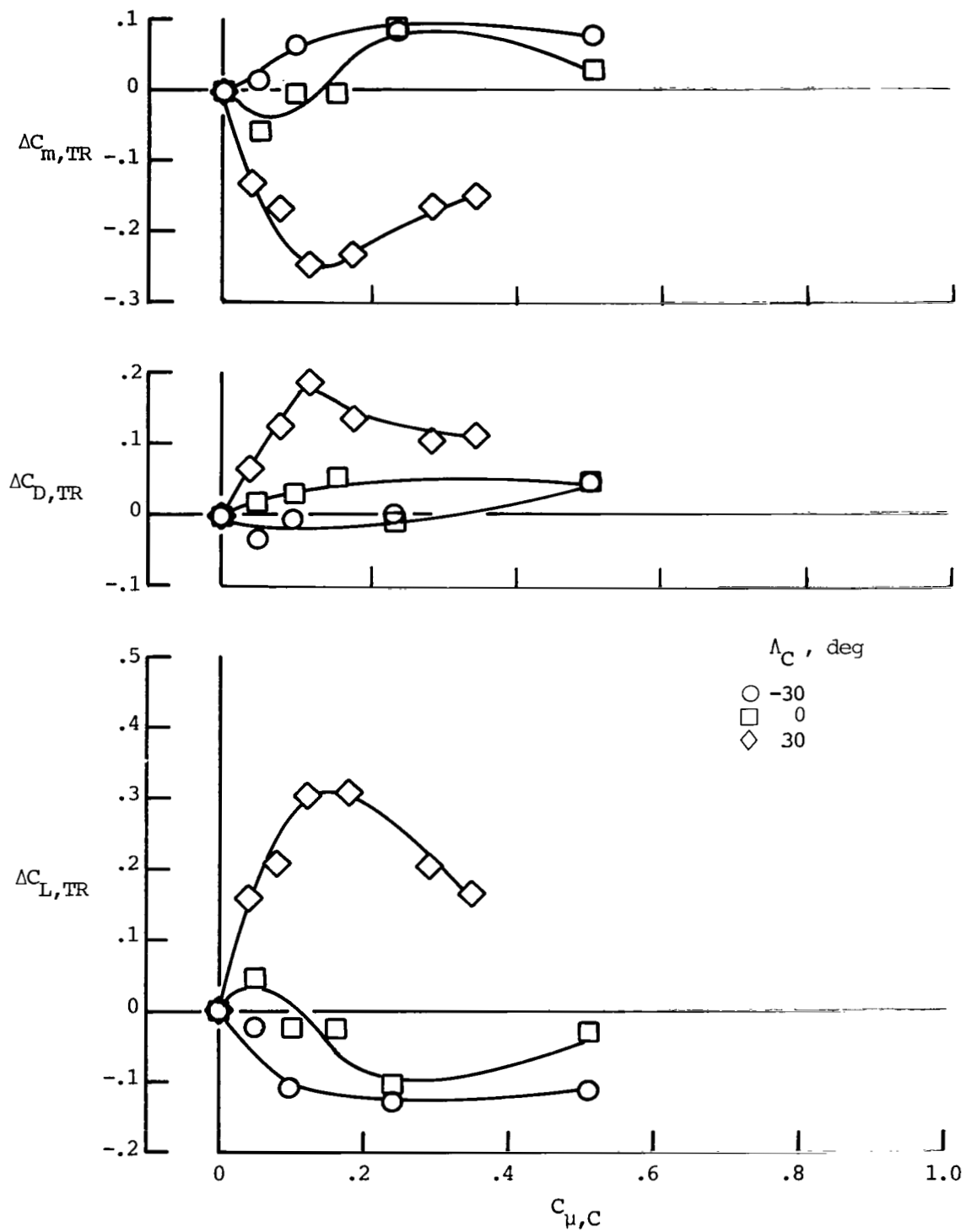
(f) Port 6 at location B. $\delta_f = 45^\circ/45^\circ$;
 $A_{e,P}/A_{e,PRI} = 0.10$; $\Lambda_P = 45^\circ$.

Figure 22.- Continued.



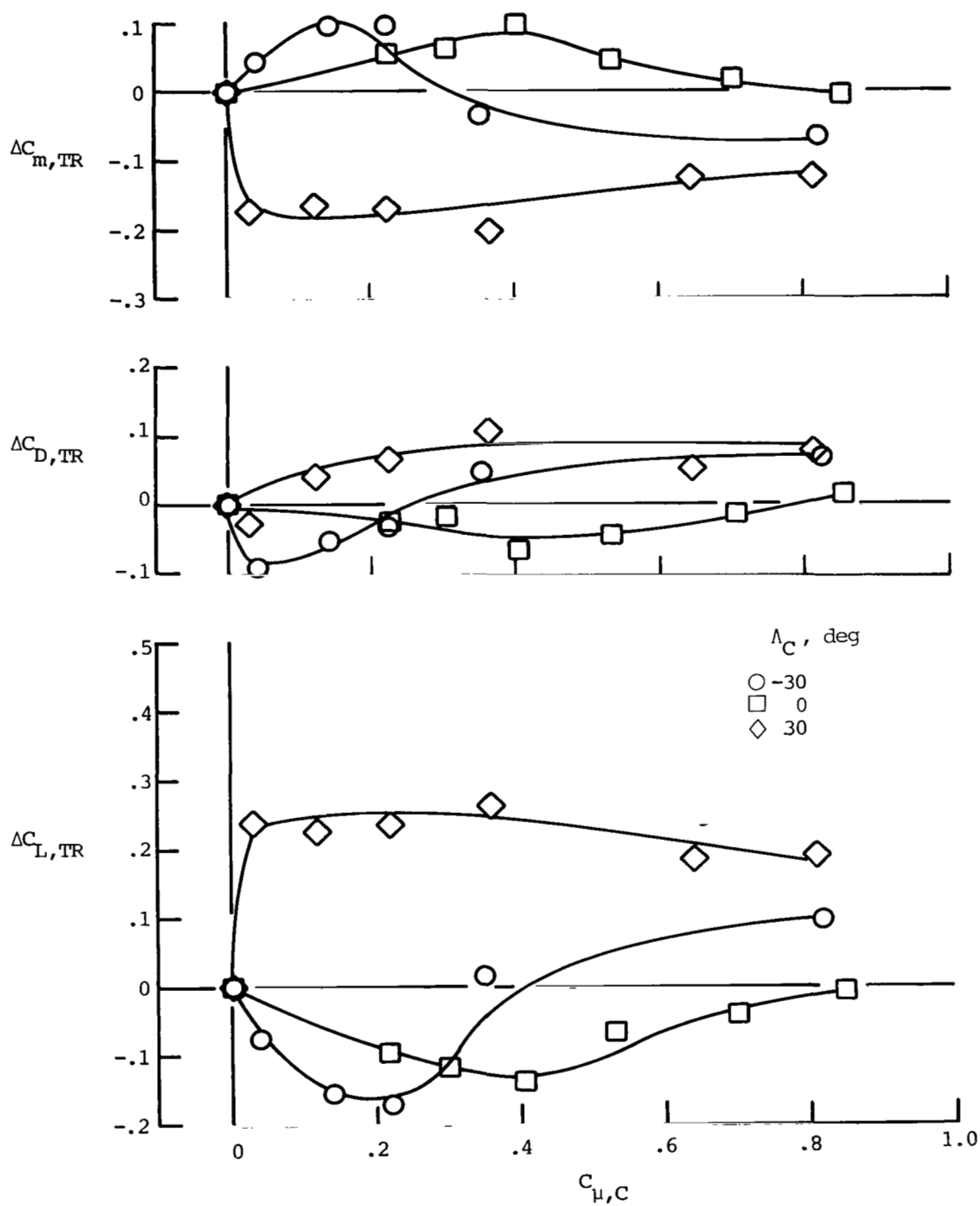
(g) Port 7 at location B. $\delta_f = 45^\circ/45^\circ$;
 $A_{e,P}/A_{e,PRI} = 0.10$; $\Lambda_P = 60^\circ$.

Figure 22.- Concluded.



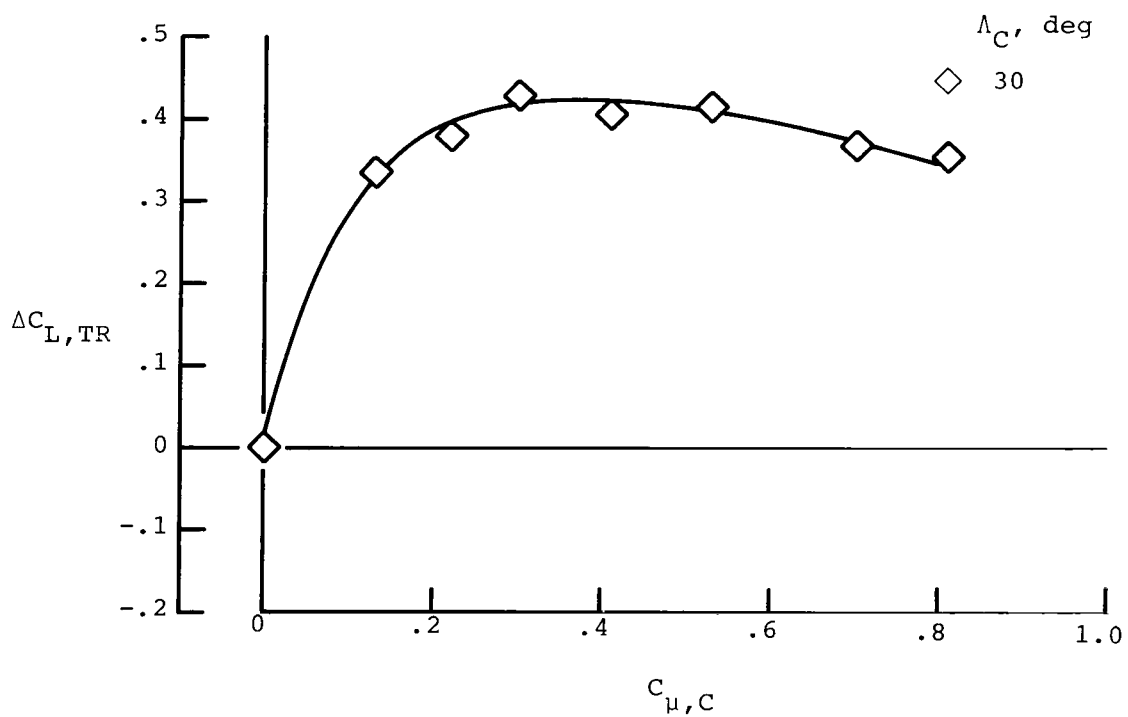
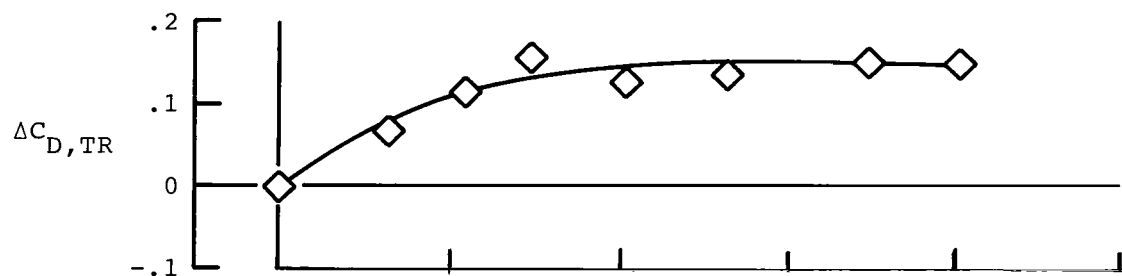
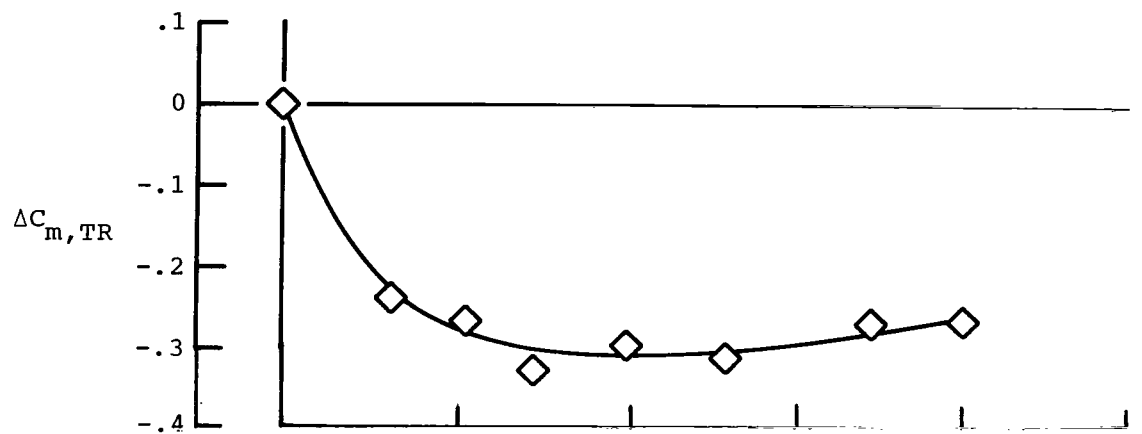
(a) $\delta_f = 45^\circ/26^\circ$; $A_{e,C}/A_{e,PRI} = 0.20$.

Figure 23.- Effect of cascade-nozzle vector angles on induced longitudinal aerodynamics. $\alpha = 14^\circ$.



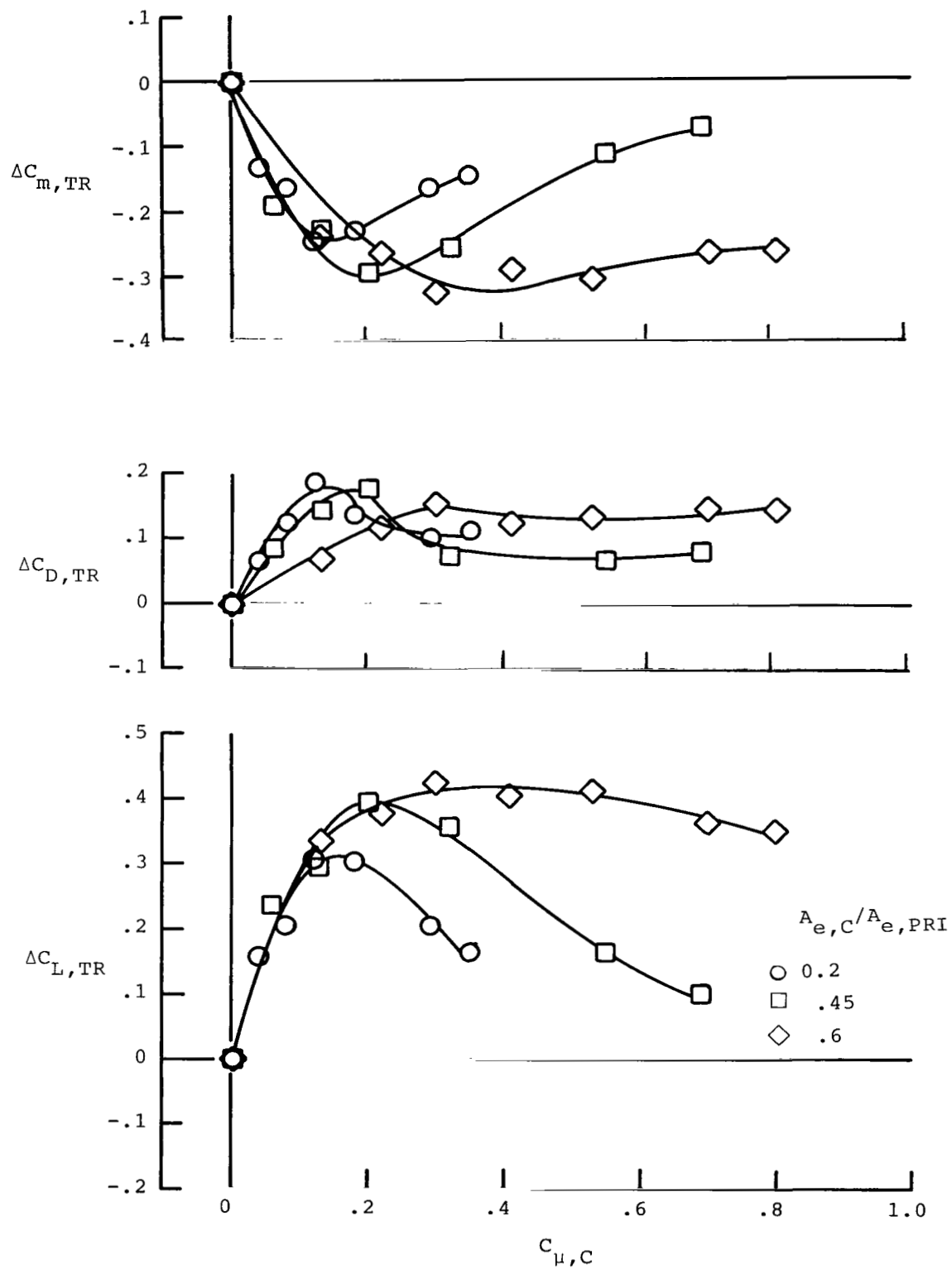
(b) $\delta_f = 45^\circ/26^\circ$; $A_{e,C}/A_{e,PRI} = 0.60$.

Figure 23.- Continued.



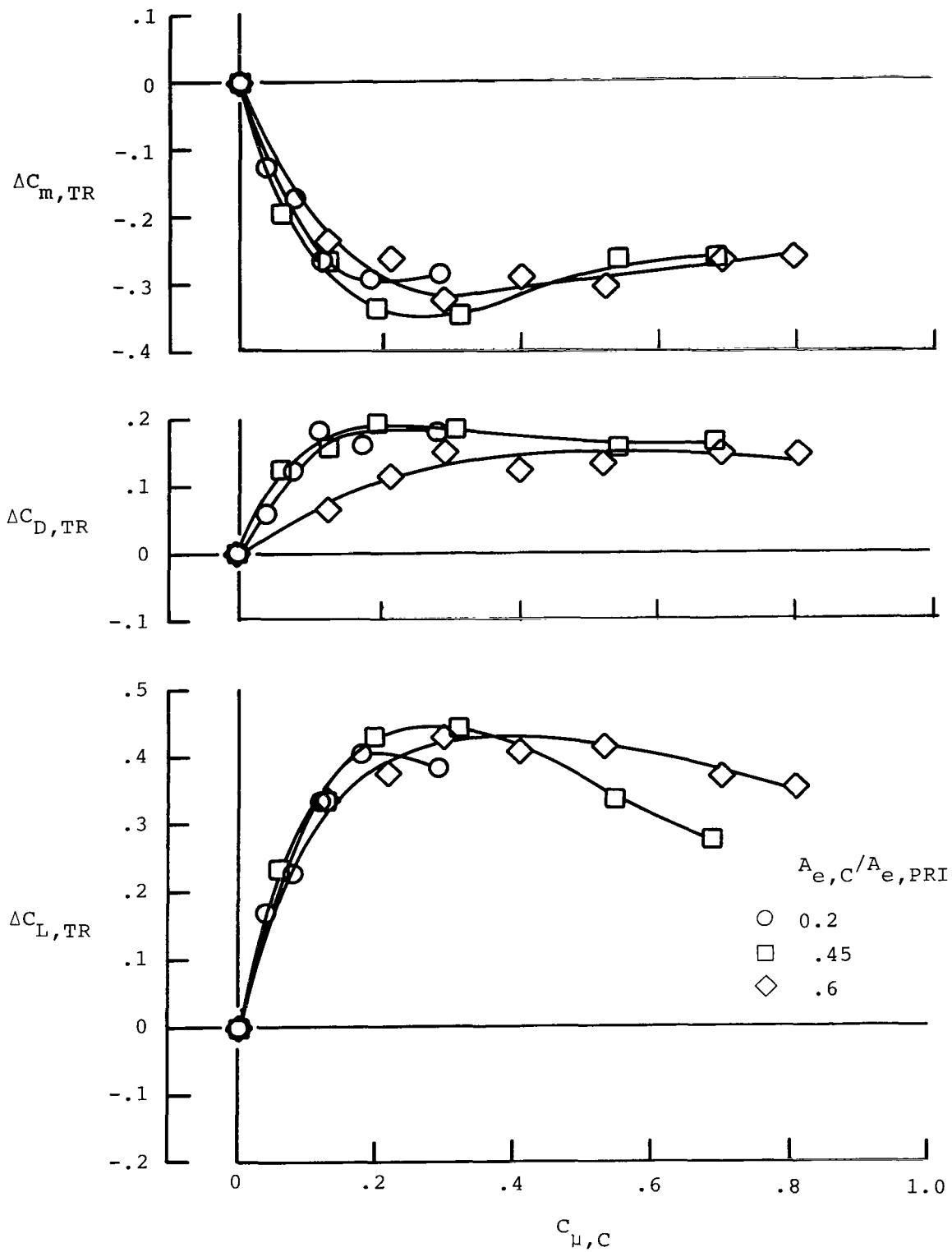
(c) $\delta_f = 45^\circ/45^\circ$; $A_{e,C}/A_{e,PRI} = 0.60$.

Figure 23.- Concluded.



(a) $\delta_f = 45^\circ/26^\circ$.

Figure 24.- Effect of cascade-nozzle exit area on induced longitudinal aerodynamics. $\alpha = 14^\circ$; $\Lambda_C = 30^\circ$.



(b) $\delta_f = 45^\circ/45^\circ$.

Figure 24.- Concluded.

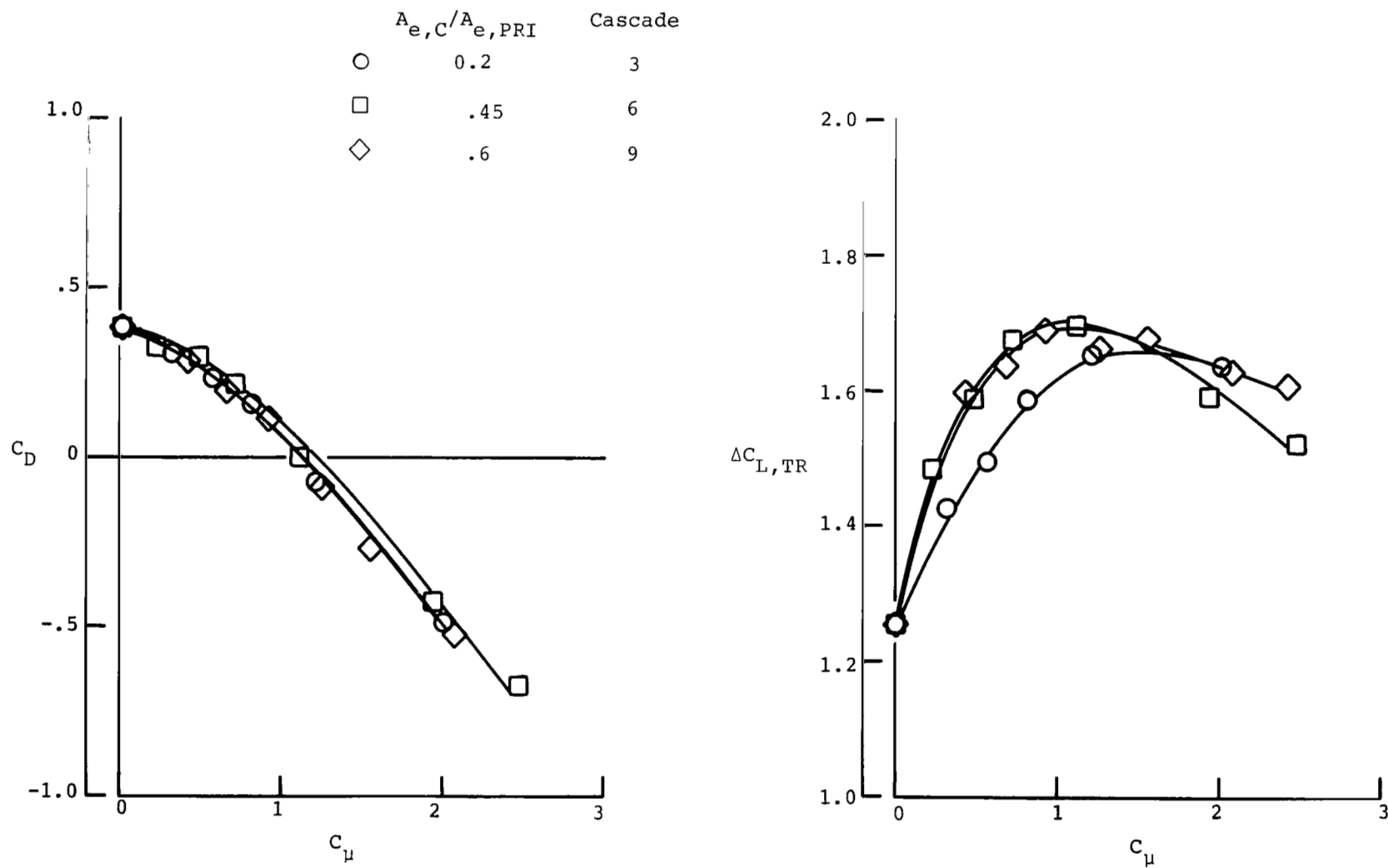


Figure 25.- Comparison of cascades 3, 6, and 9 on a drag balance and induced-lift basis. $\alpha = 14^\circ$;
 $\delta_f = 45^\circ/45^\circ$.

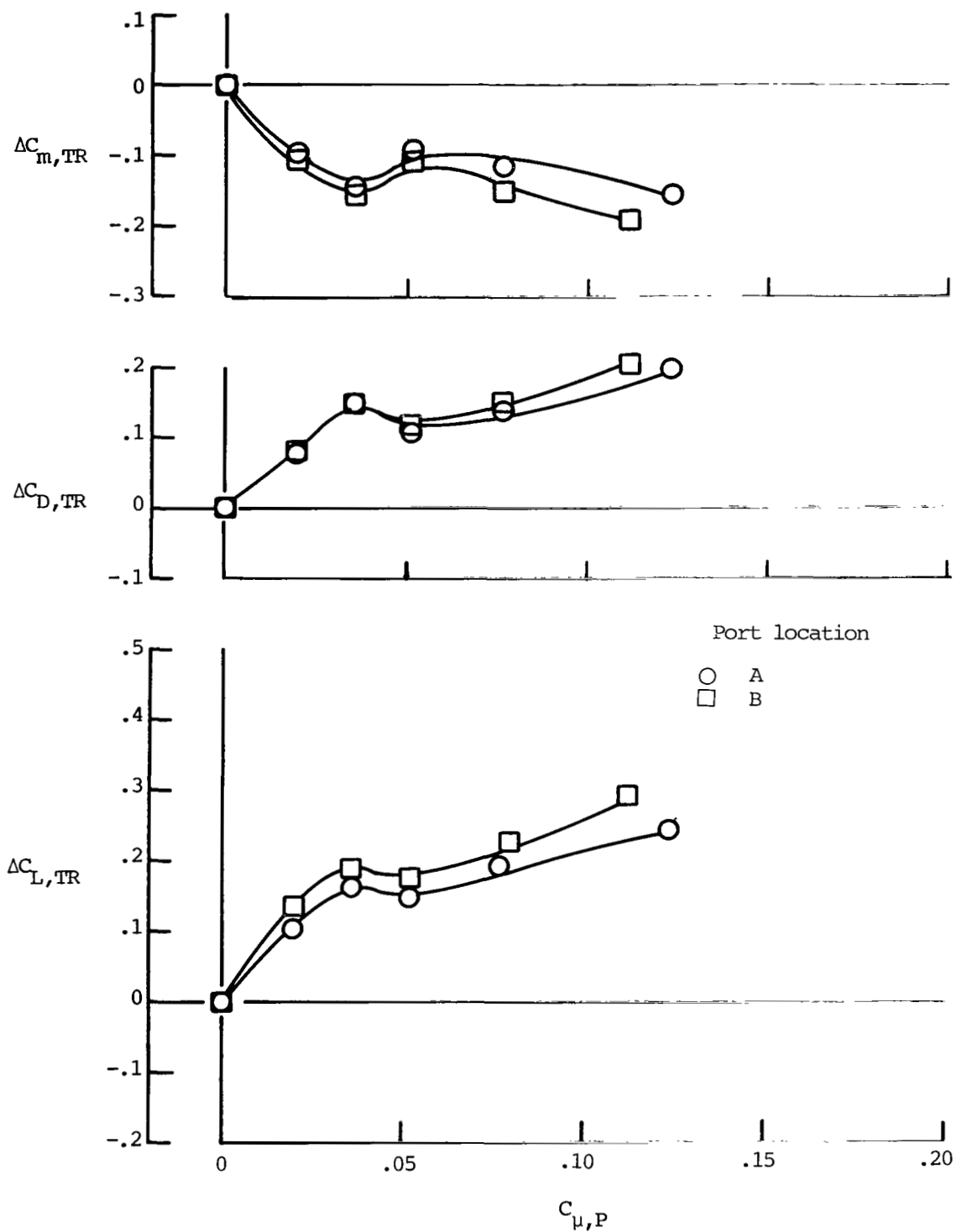
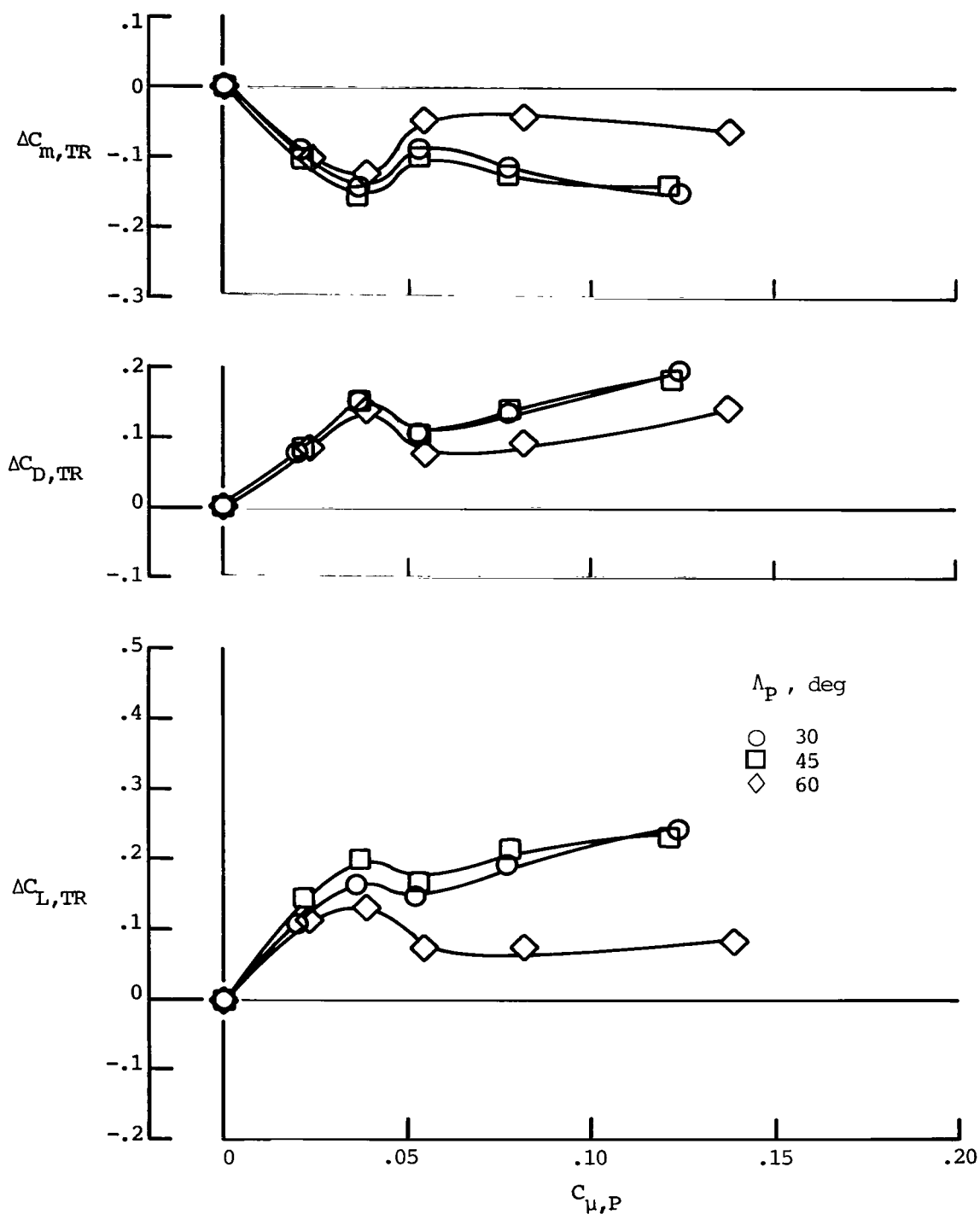
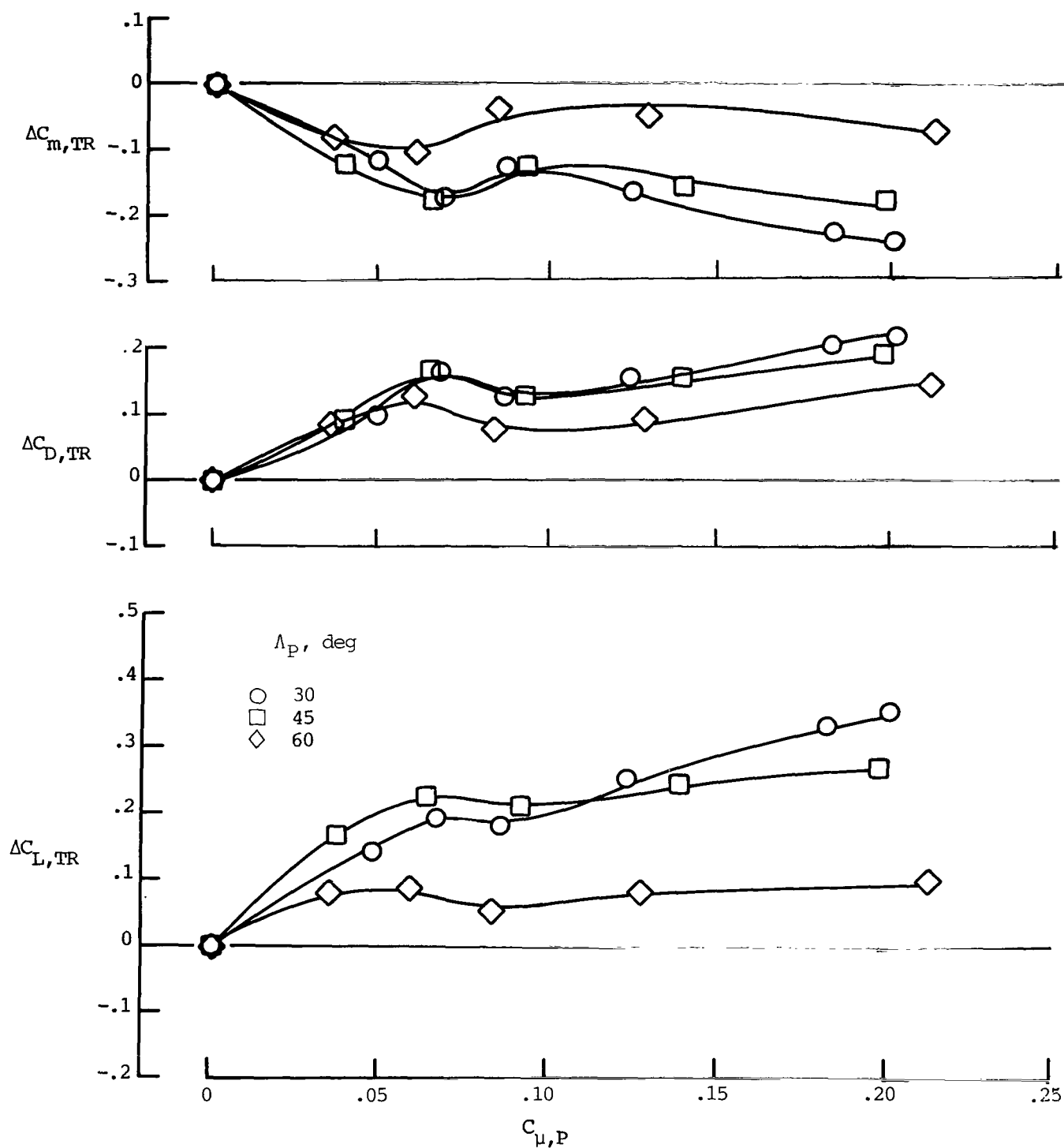


Figure 26.- Effect of port-nozzle location on induced longitudinal aerodynamics.
 $\alpha = 14^\circ$; $A_{e,P}/A_{e,PRI} = 0.05$; $\delta_f = 45^\circ/45^\circ$; $\Lambda_P = 30^\circ$.



(a) Location A; $A_{e,P}/A_{e,PRI} = 0.05$.

Figure 27.- Effect of port-nozzle vector angle on induced longitudinal aerodynamics. $\alpha = 14^\circ$; $\delta_f = 45^\circ/45^\circ$.



(b) Location B; $A_{e,P}/A_{e,PRI} = 0.10$.

Figure 27.- Concluded.

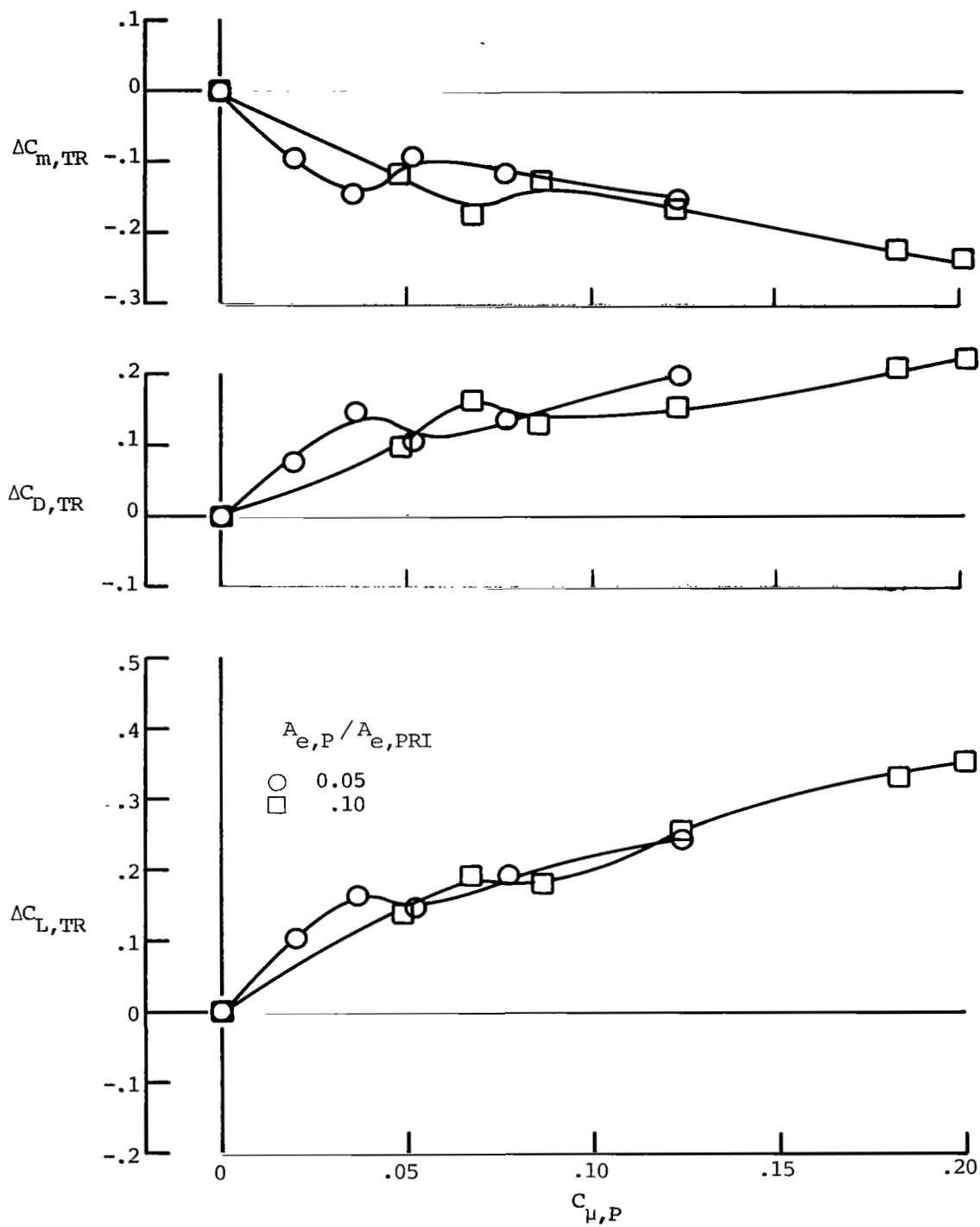
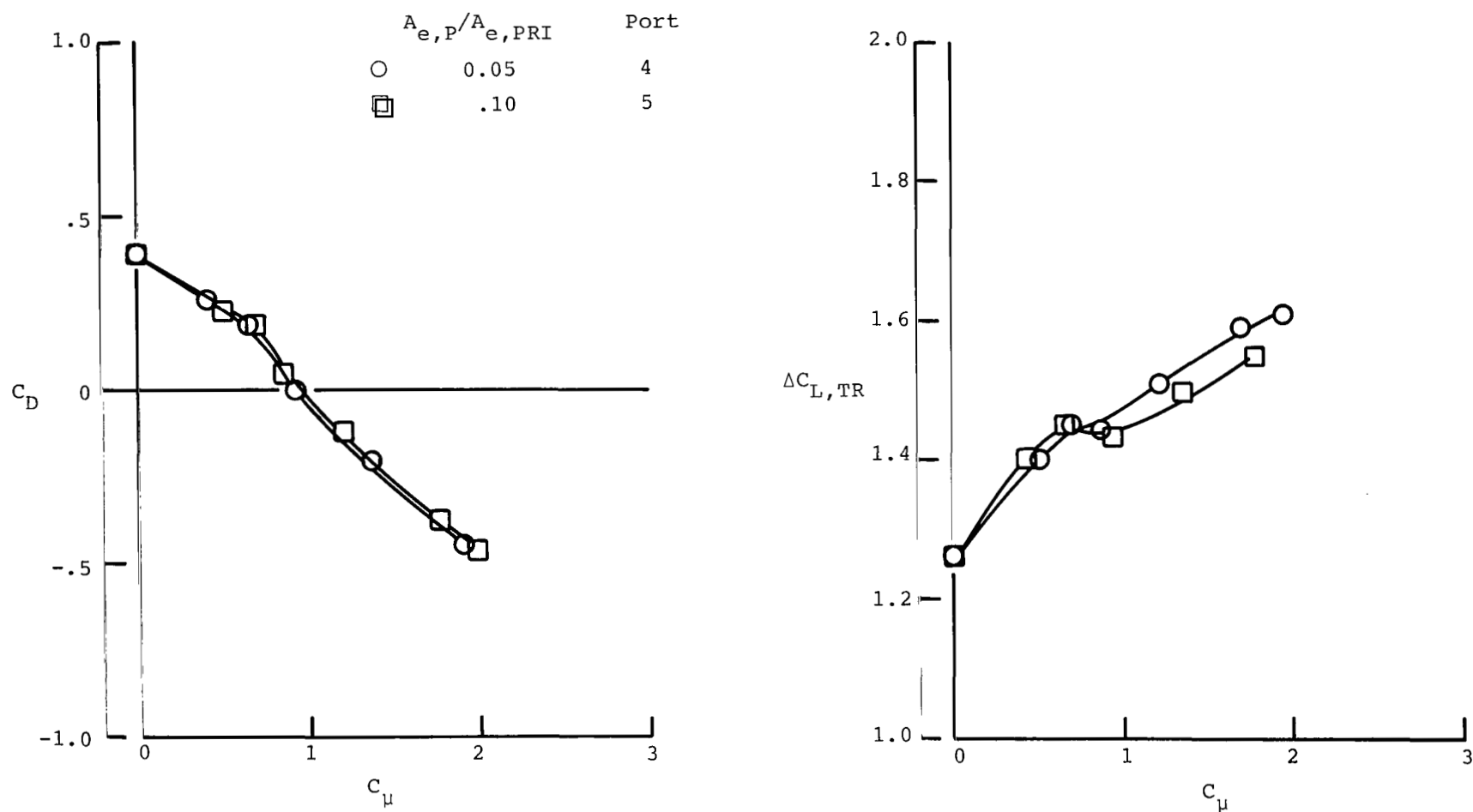
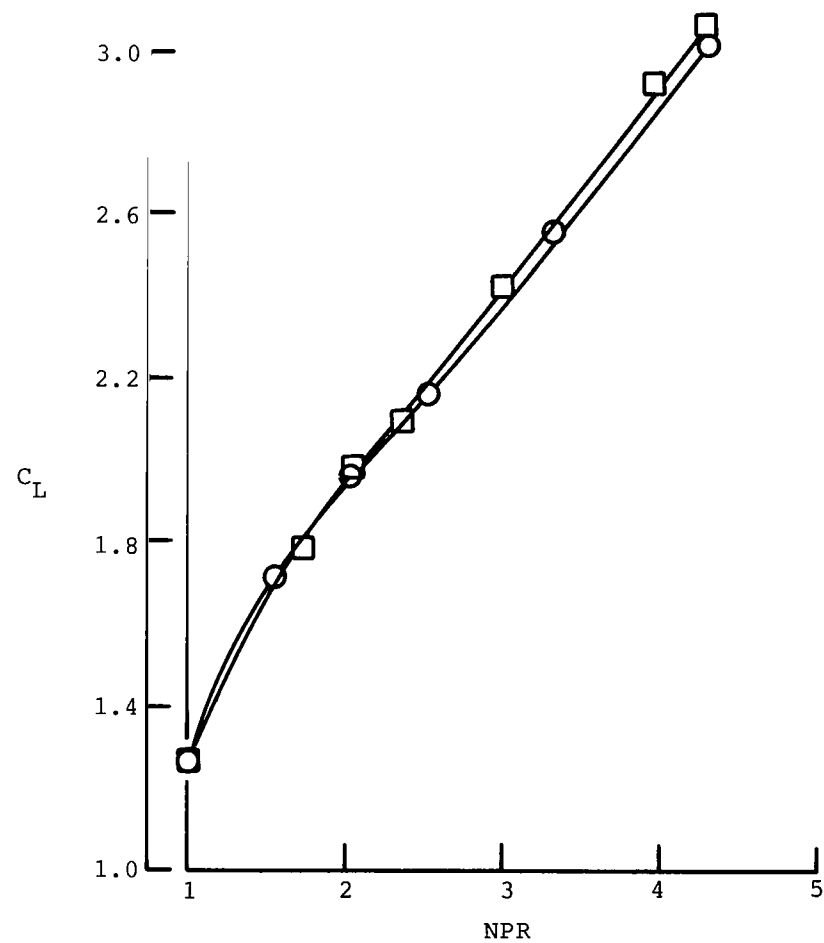
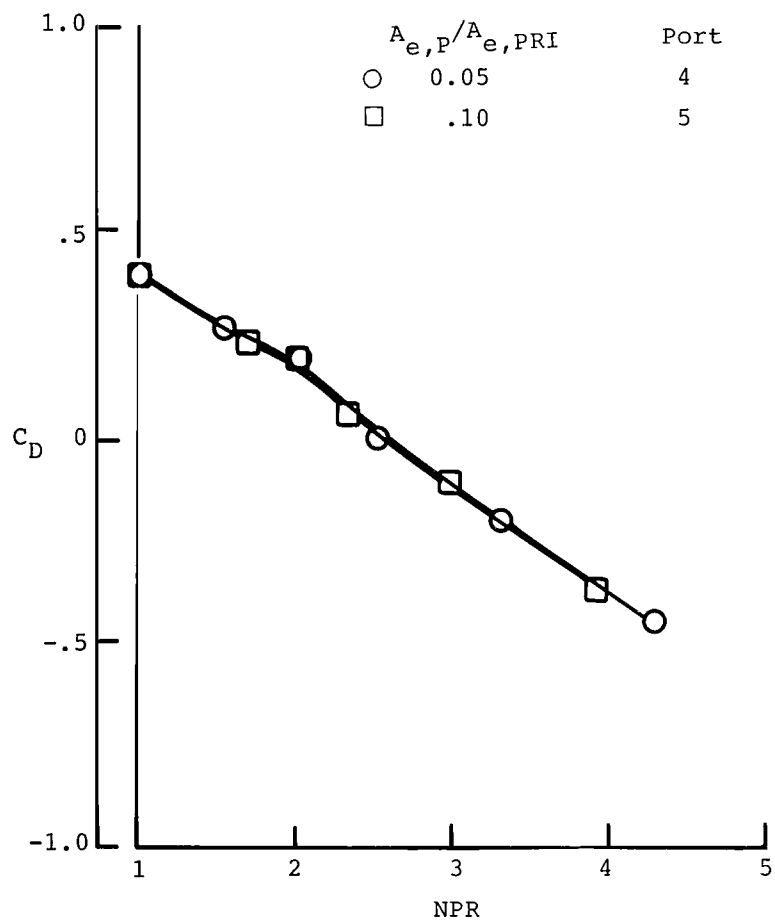


Figure 28.- Effect of port-nozzle exit area on induced longitudinal aerodynamics. Location B; $\alpha = 14^\circ$; $\delta_f = 45^\circ/45^\circ$; $\Lambda_p = 30^\circ$.



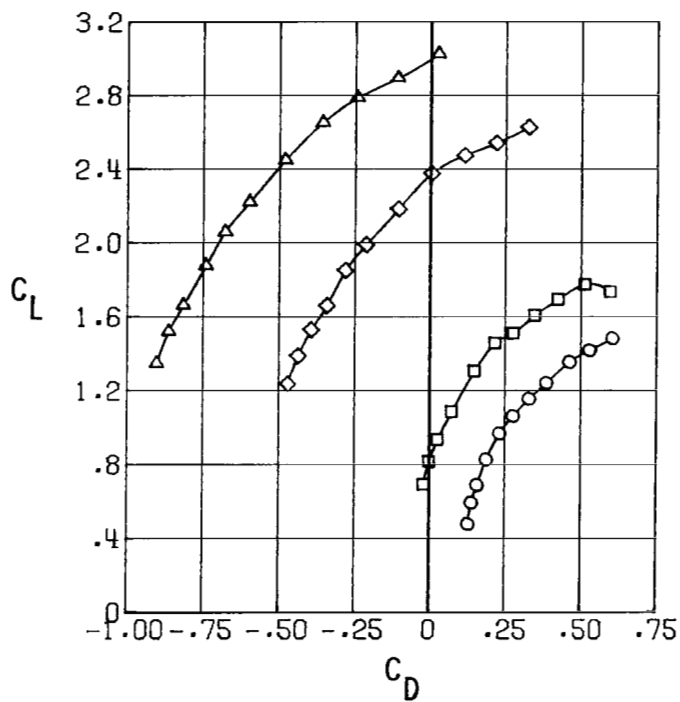
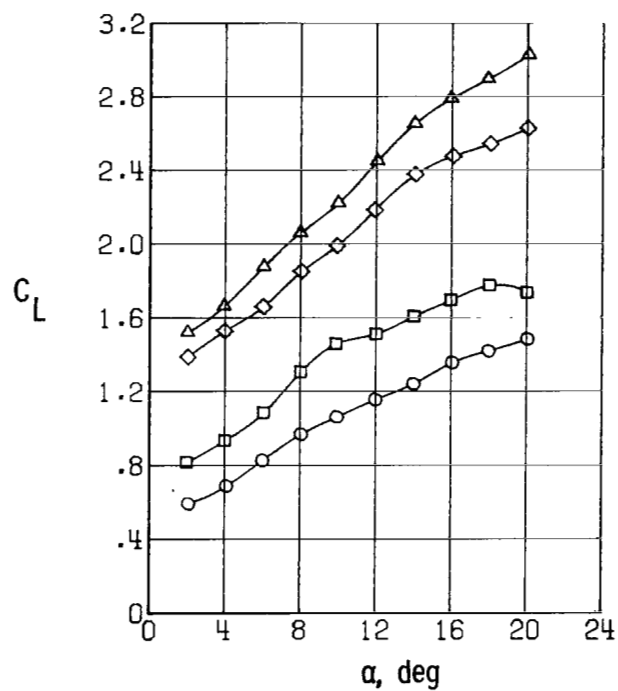
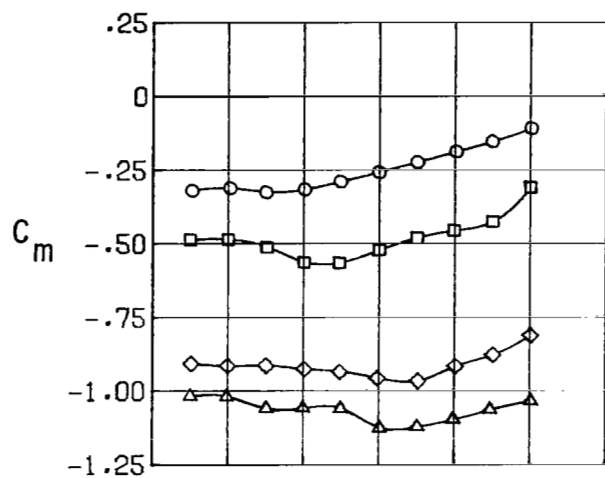
(a) Drag balance and thrust-removed lift plotted against C_μ .

Figure 29.- Comparison of ports 4 and 5. Location B; $\alpha = 14^\circ$; $\delta_f = 45^\circ/45^\circ$; $\Lambda_P = 30^\circ$.



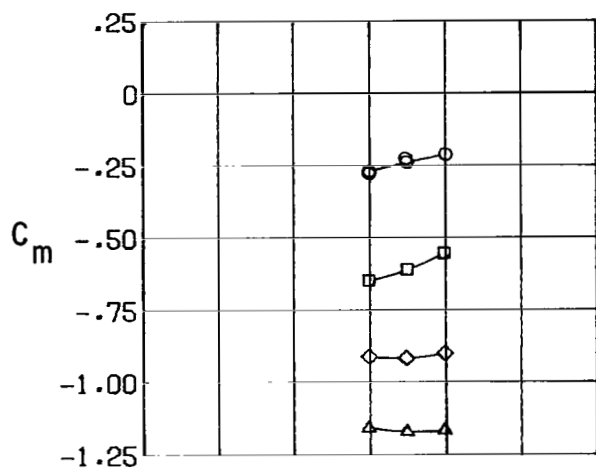
(b) Drag balance and lift plotted against NPR.

Figure 29.- Concluded.

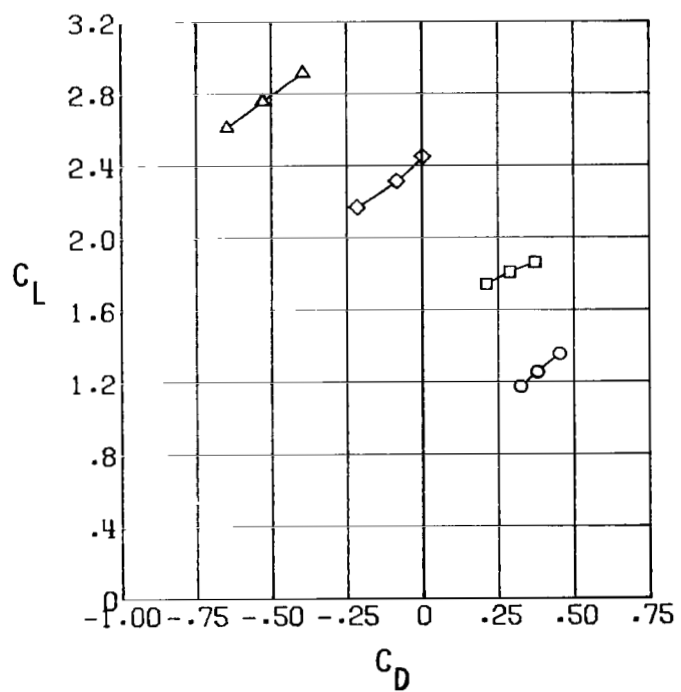
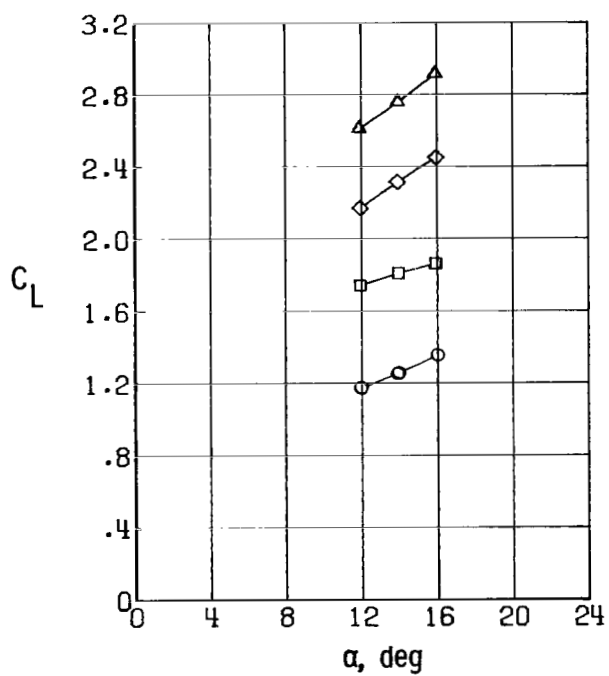


(a) Cascade 6.

Figure 30.- Effect of power on longitudinal aerodynamics of selected cascade and port configurations. $\delta_f = 45^\circ/45^\circ$; $\delta_{PRI} = 45^\circ$.

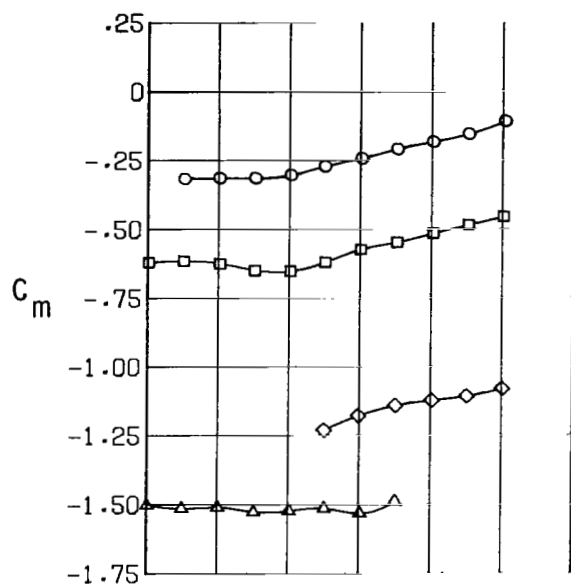


	C_μ	$C_{\mu, \text{PRI}}$	$C_{\mu, \text{C}}$
○	0	0	0
□	.42	.29	.13
◇	1.26	.84	.42
△	2.10	1.40	.70

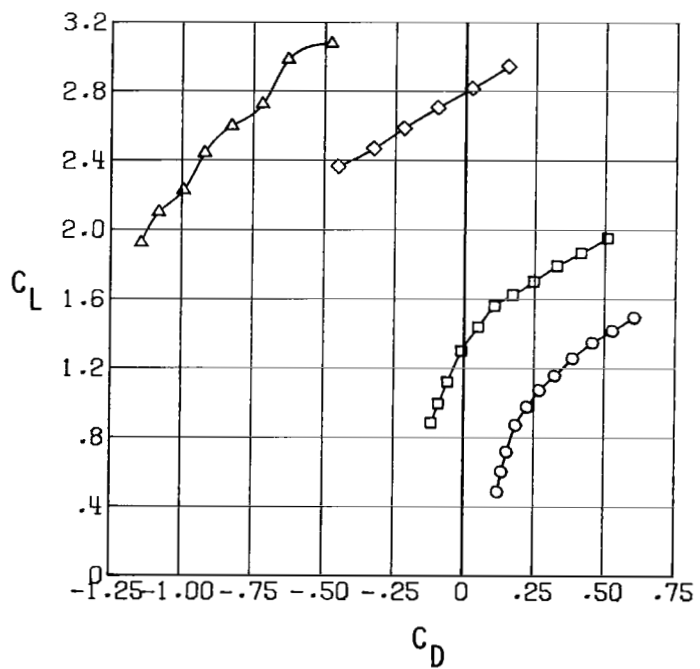
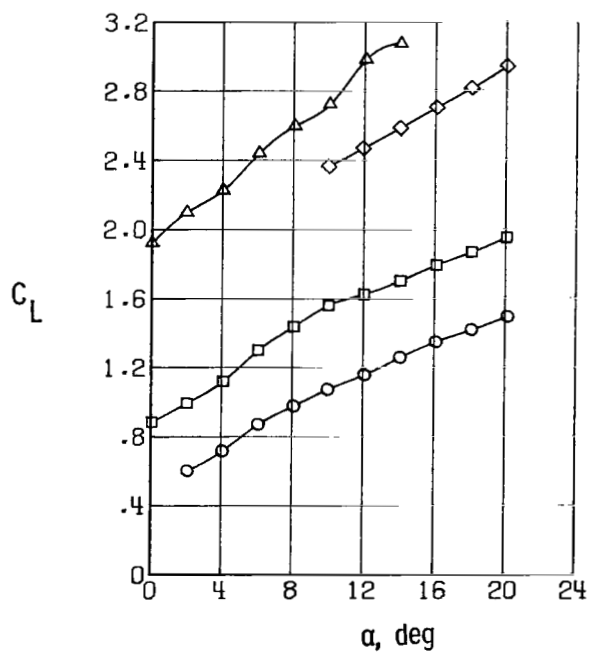


(b) Cascade 9.

Figure 30.- Continued.

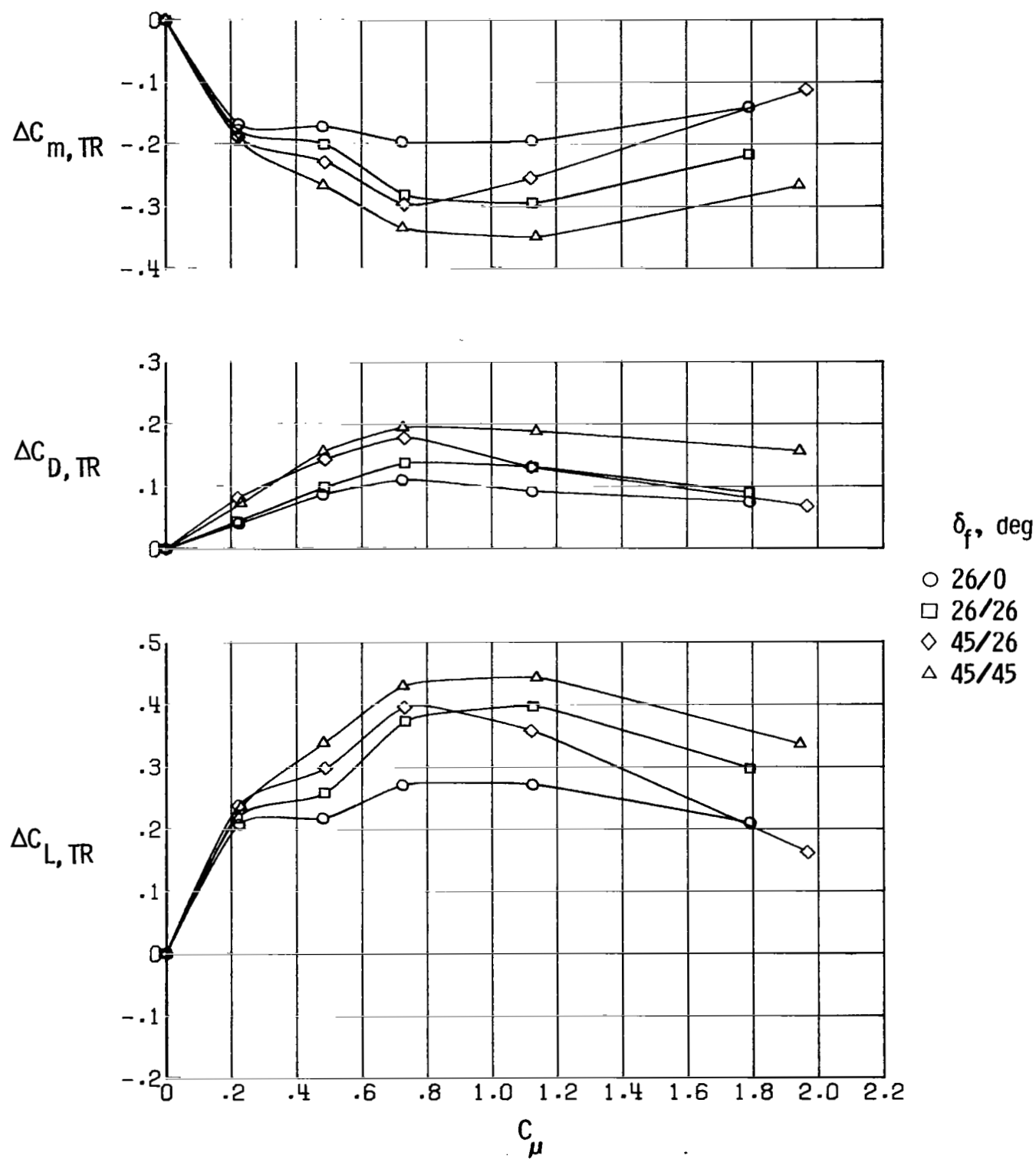


C_μ	$C_{\mu, PRI}$	$C_{\mu, P}$
○ 0	0	0
□ .40	.35	.05
◇ 1.40	1.25	.15
△ 1.96	1.75	.21



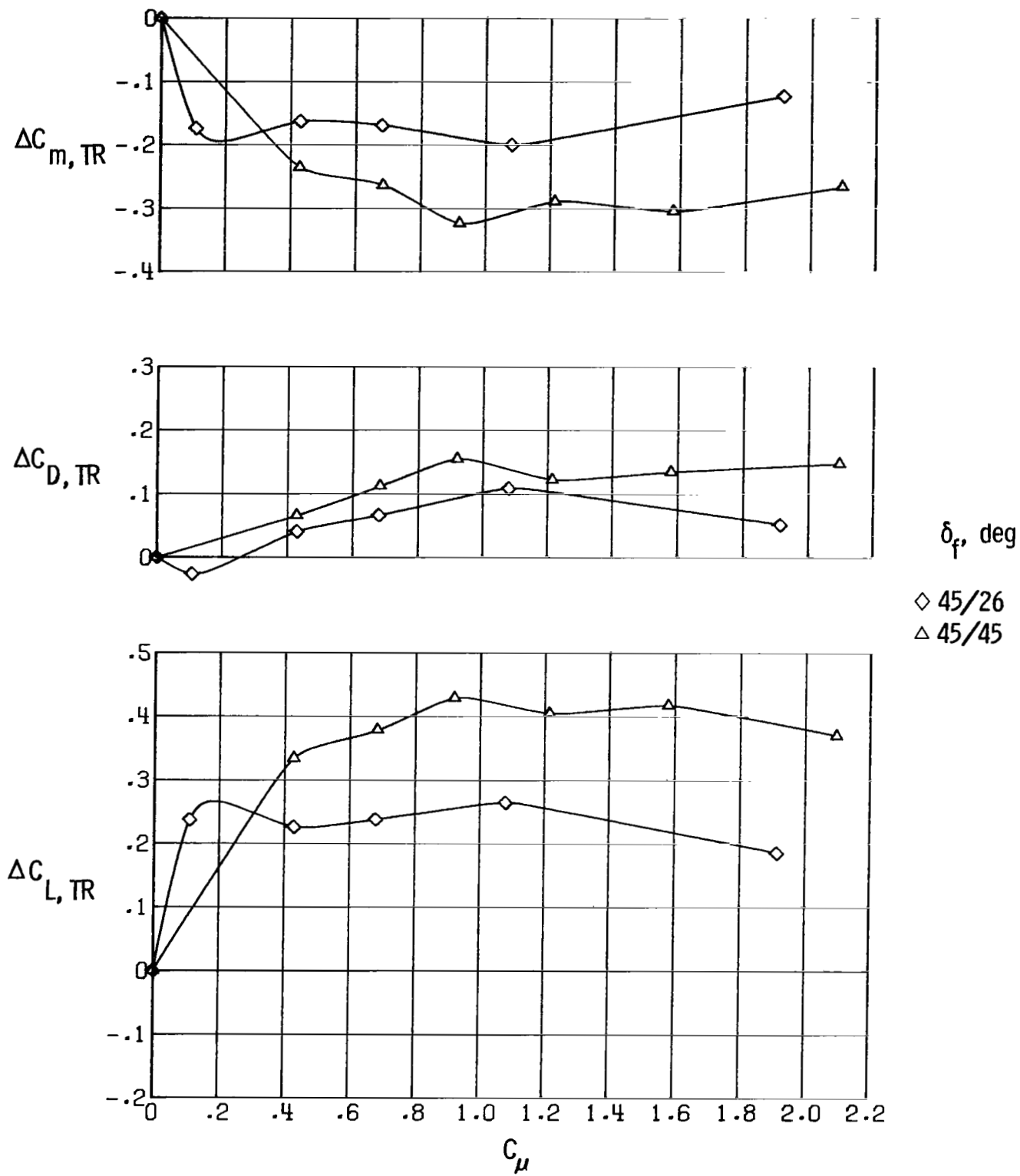
(c) Port 5.

Figure 30.- Concluded.



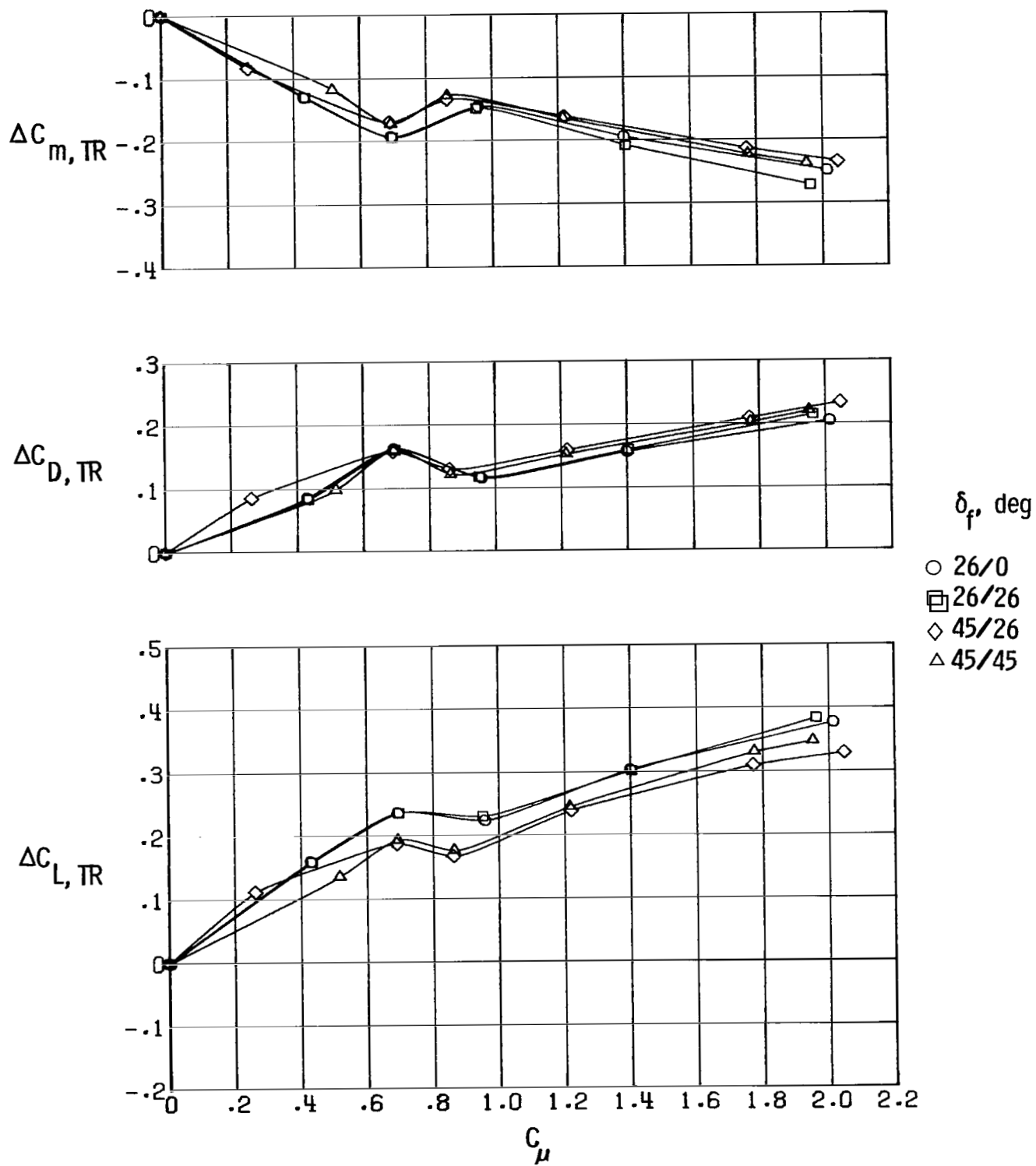
(a) Cascade 6.

Figure 31.- Effect of C_μ and flap deflection on induced longitudinal aerodynamics of selected configurations. $\alpha = 14^\circ$; $\delta_{PRI} = 45^\circ$.



(b) Cascade 9.

Figure 31.- Continued.



(c) Port 5.

Figure 31.- Concluded.



L-83-144

Figure 32.- Photograph of oil flow on wing upper surface. $\alpha = 14^\circ$; $\delta_f = 45^\circ/26^\circ$;
 $C_\mu = 0$.



L-83-145

Figure 33.- Wing upper-surface oil-flow photograph. Port 5; $\delta_f = 45^\circ/45^\circ$.

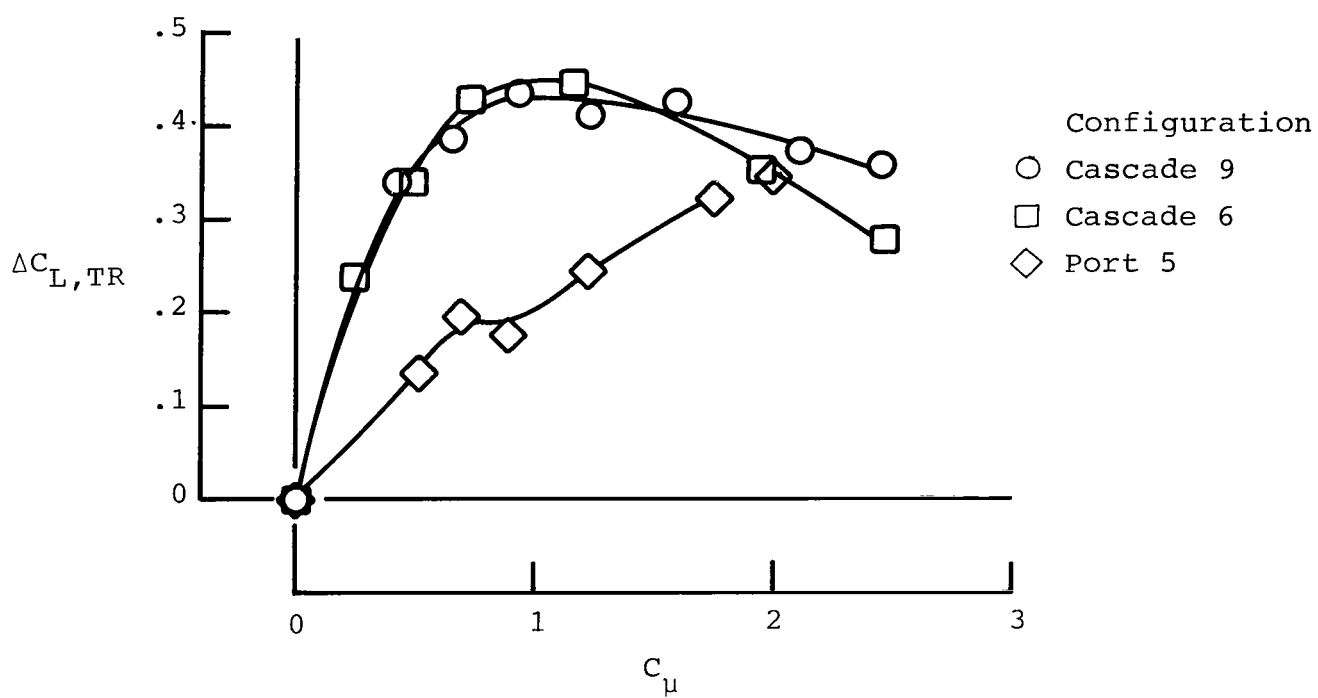
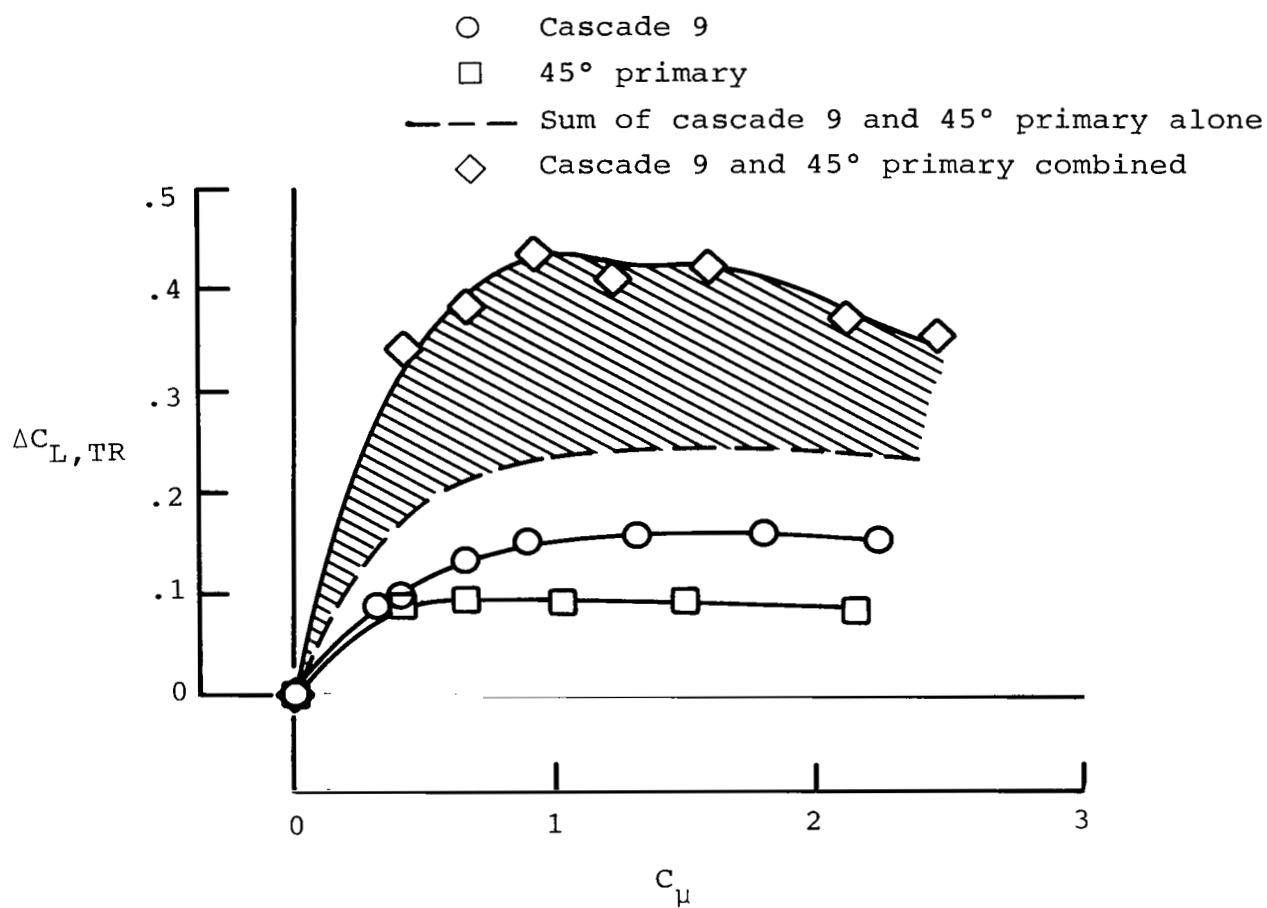
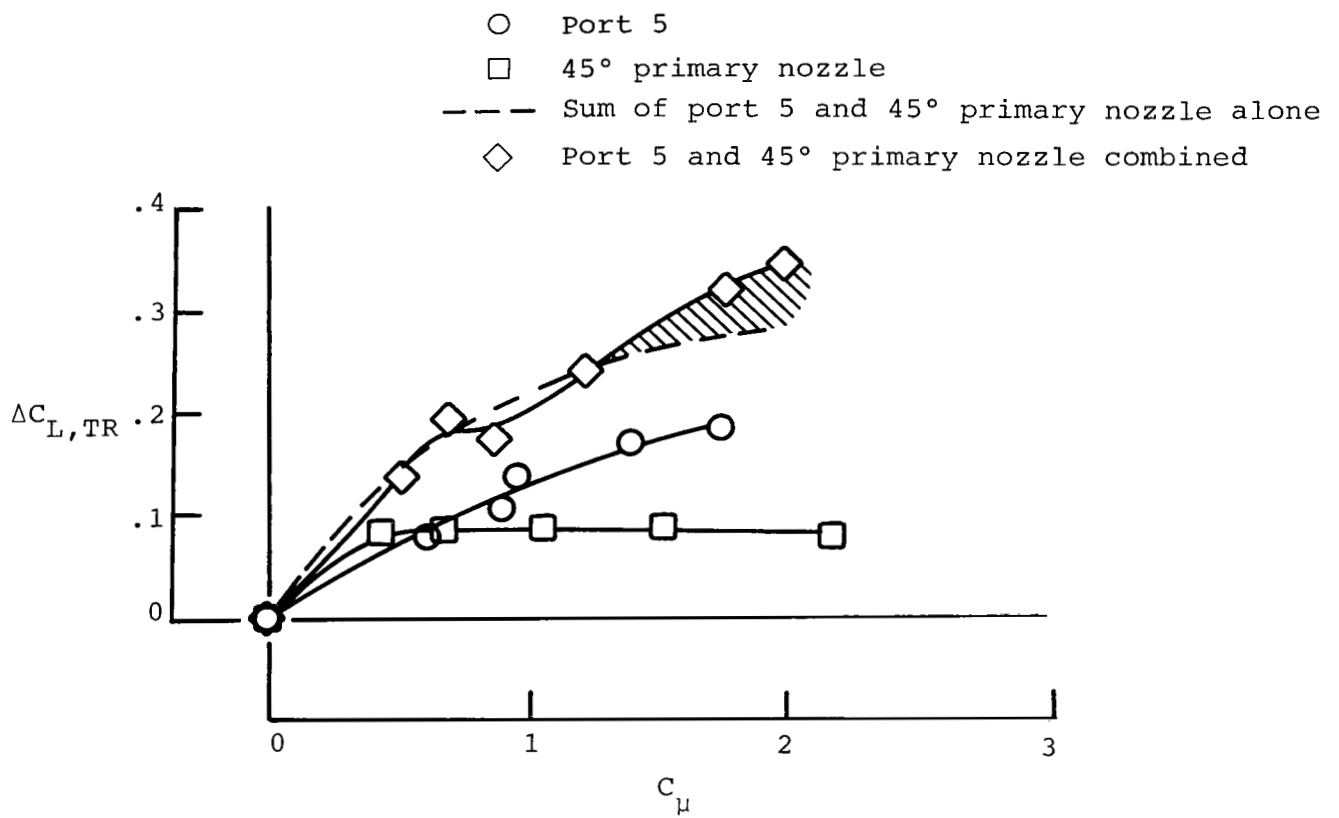


Figure 34.- Comparison of induced lift for selected configurations. $\delta_{PRI} = 45^\circ$; $\delta_f = 45^\circ/45^\circ$; $\alpha = 14^\circ$.



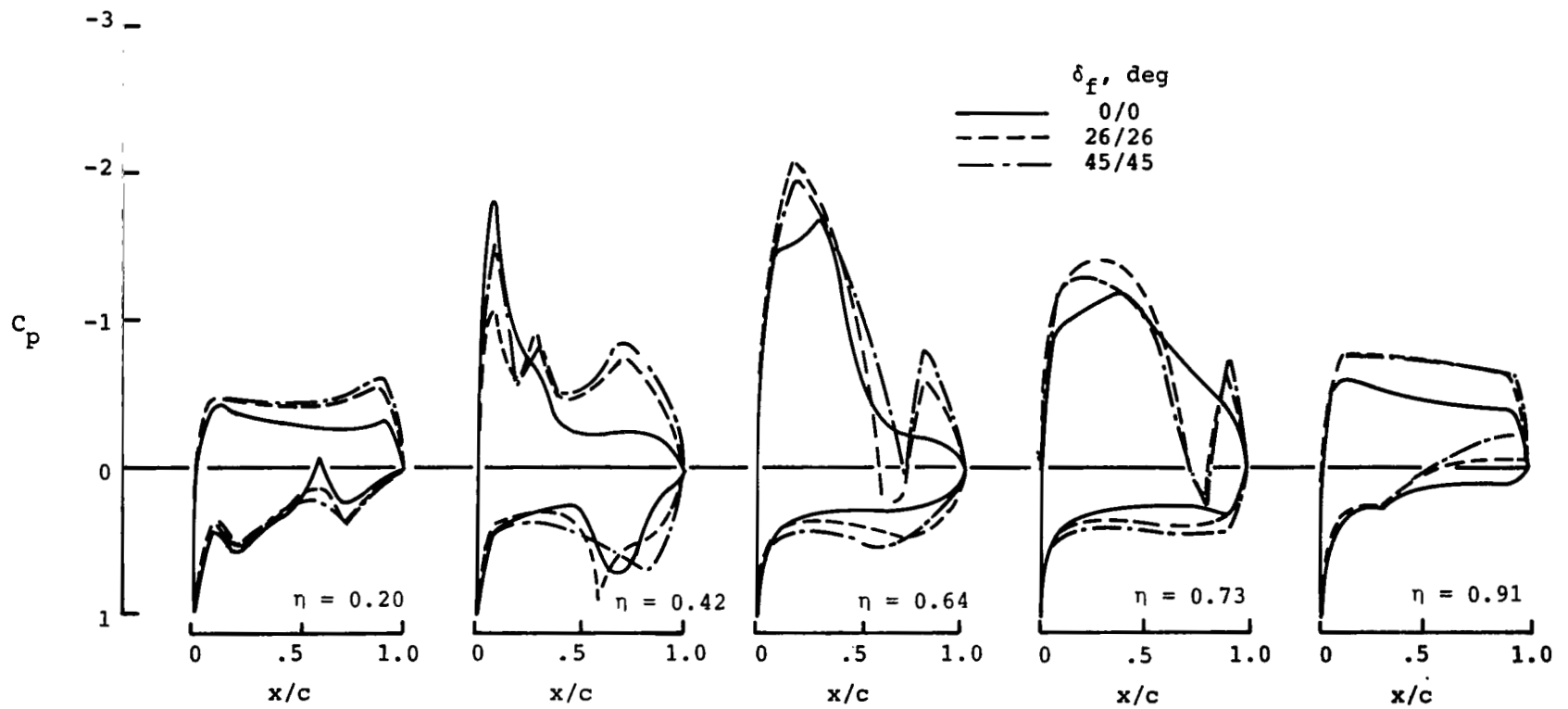
(a) Cascade 9.

Figure 35.- Breakdown of induced lift for cascade 9 and port 5. $\alpha = 14^\circ$;
 $\delta_{PRI} = 45^\circ$; $\delta_f = 45^\circ/45^\circ$.



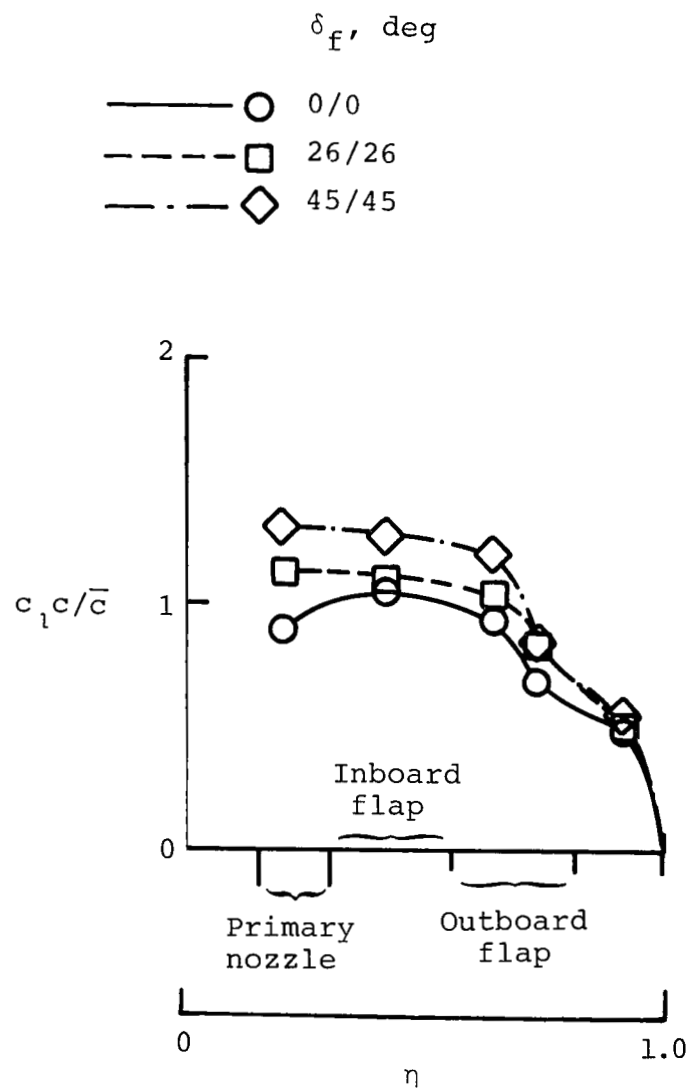
(b) Port 5.

Figure 35.- Concluded.



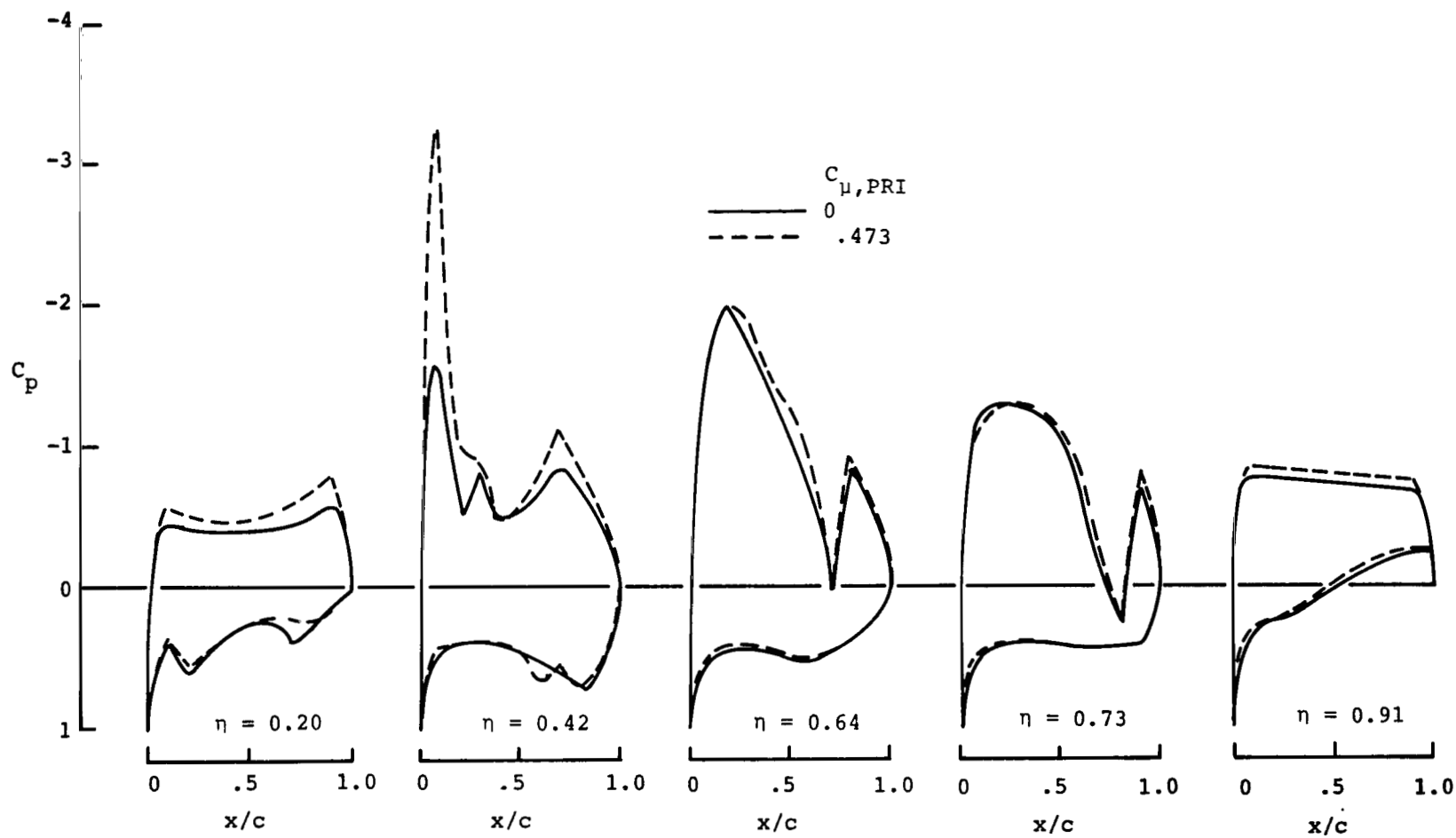
(a) Surface pressures.

Figure 36.- Effect of flap deflection on wing surface pressures and span-load distributions of baseline configuration. $\alpha = 14^\circ$; $C_{\mu} = 0$; $\delta_{PRI} = 0^\circ$.



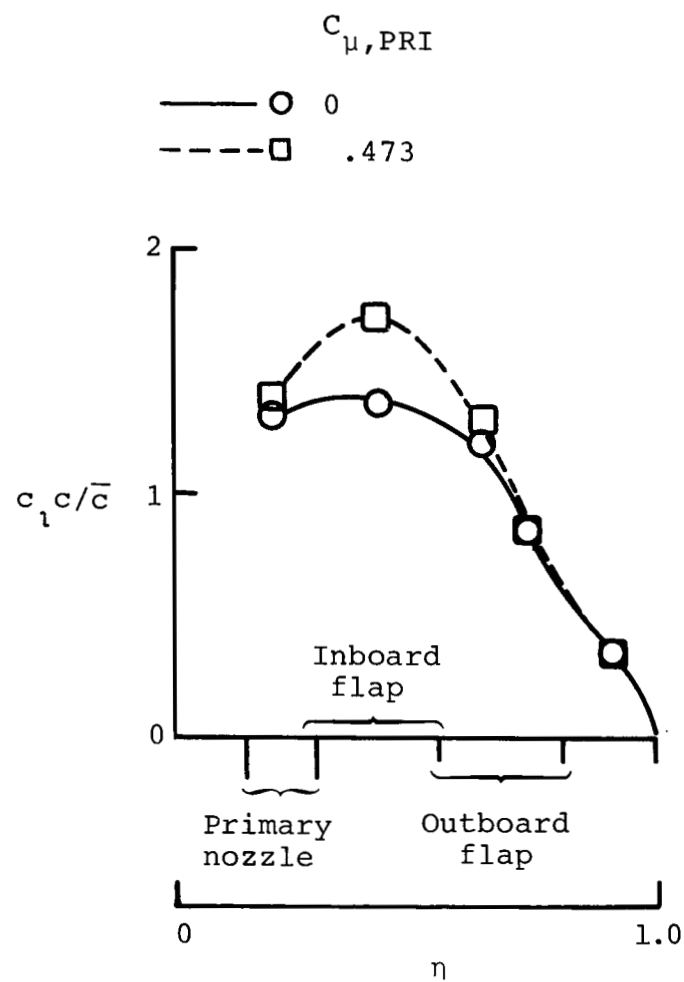
(b) Span-load distribution.

Figure 36.- Concluded.



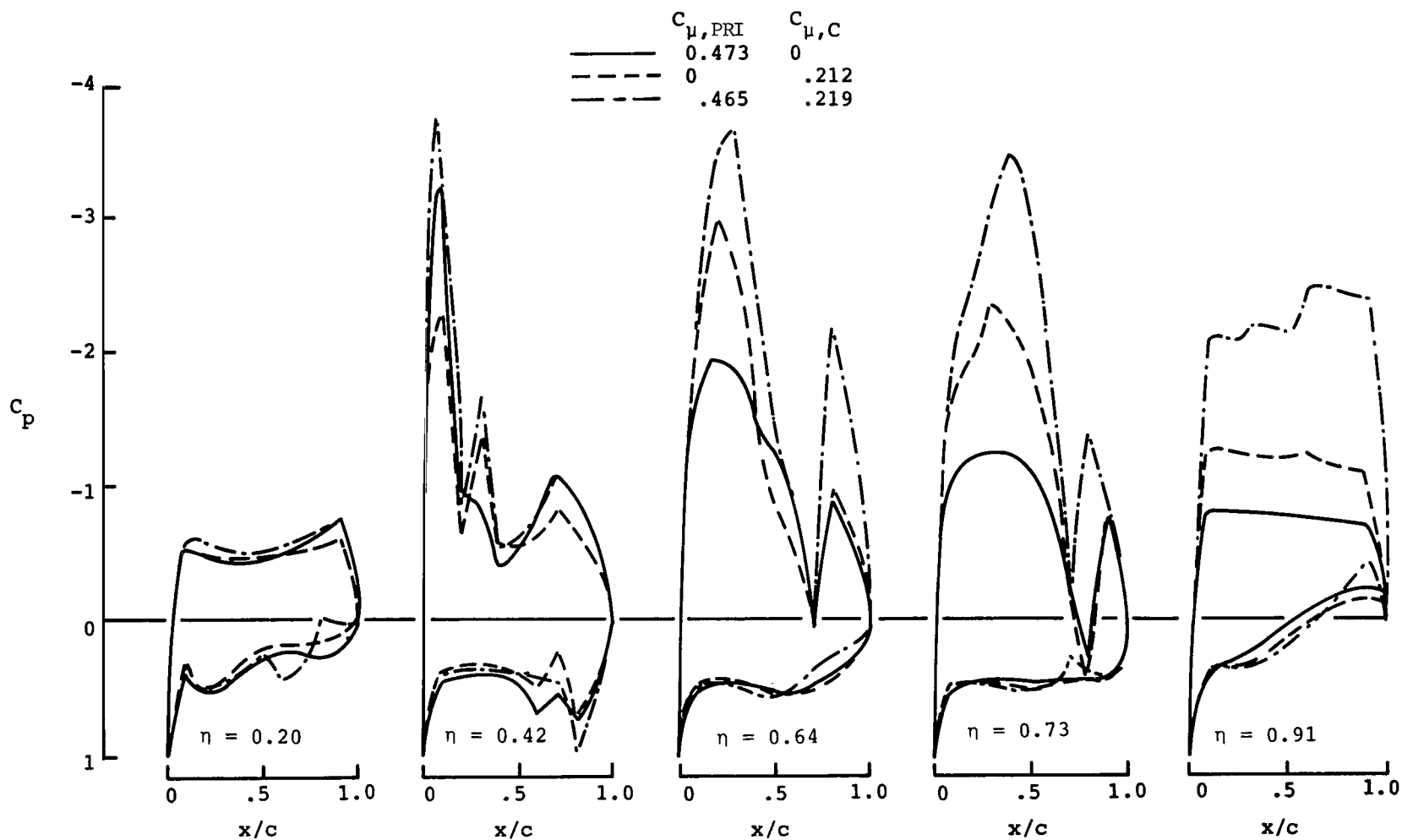
(a) Surface pressure.

Figure 37.- Effect of primary-nozzle thrust on wing surface pressures and wing span-load distribution.
 $\alpha = 14^\circ$; $\delta_f = 45^\circ/45^\circ$; $\delta_{PRI} = 45^\circ$.



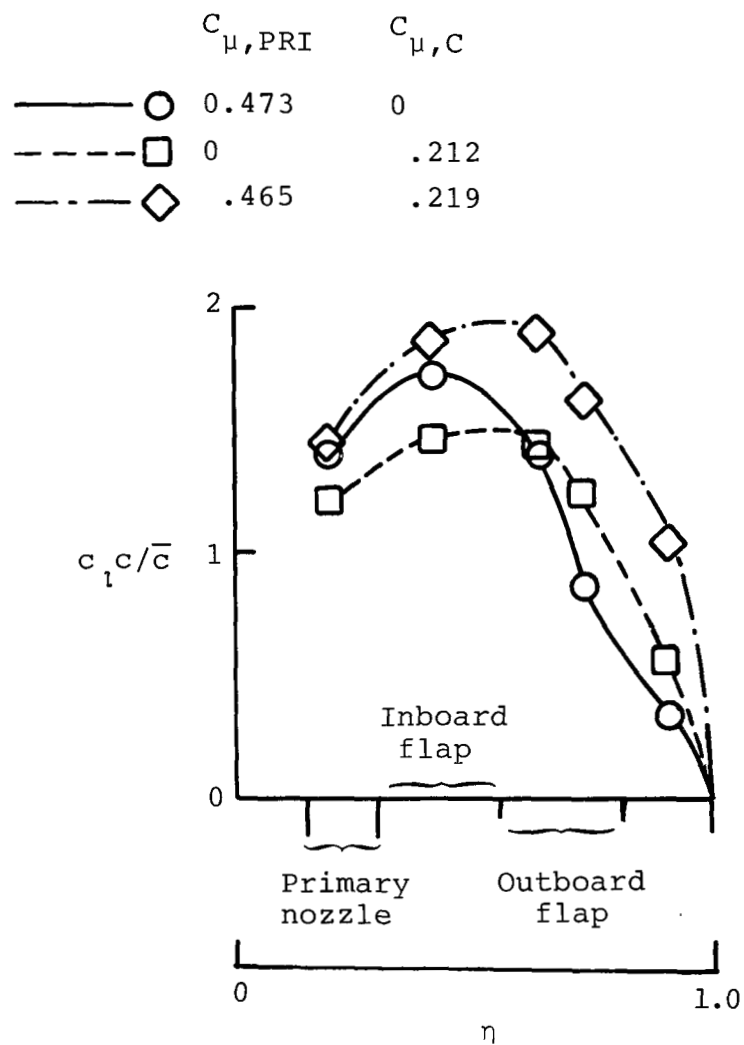
(b) Span-load distribution.

Figure 37.- Concluded.



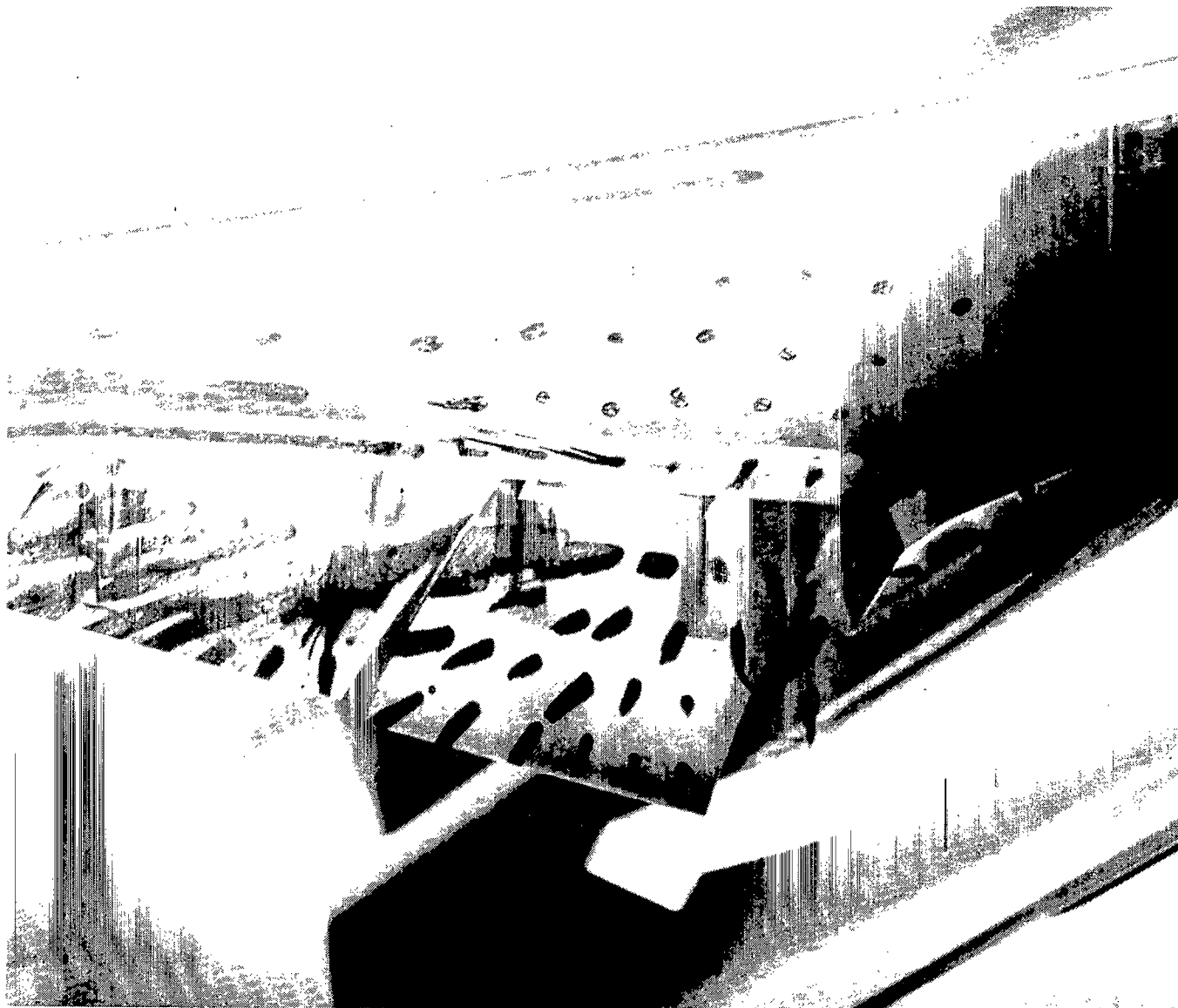
(a) Surface pressure.

Figure 38.- Effect of thrust of primary nozzle and cascade 9 on wing surface pressures and span-load distribution. $\alpha = 14^\circ$; $\delta_f = 45^\circ/45^\circ$; $\delta_{PRI} = 45^\circ$.



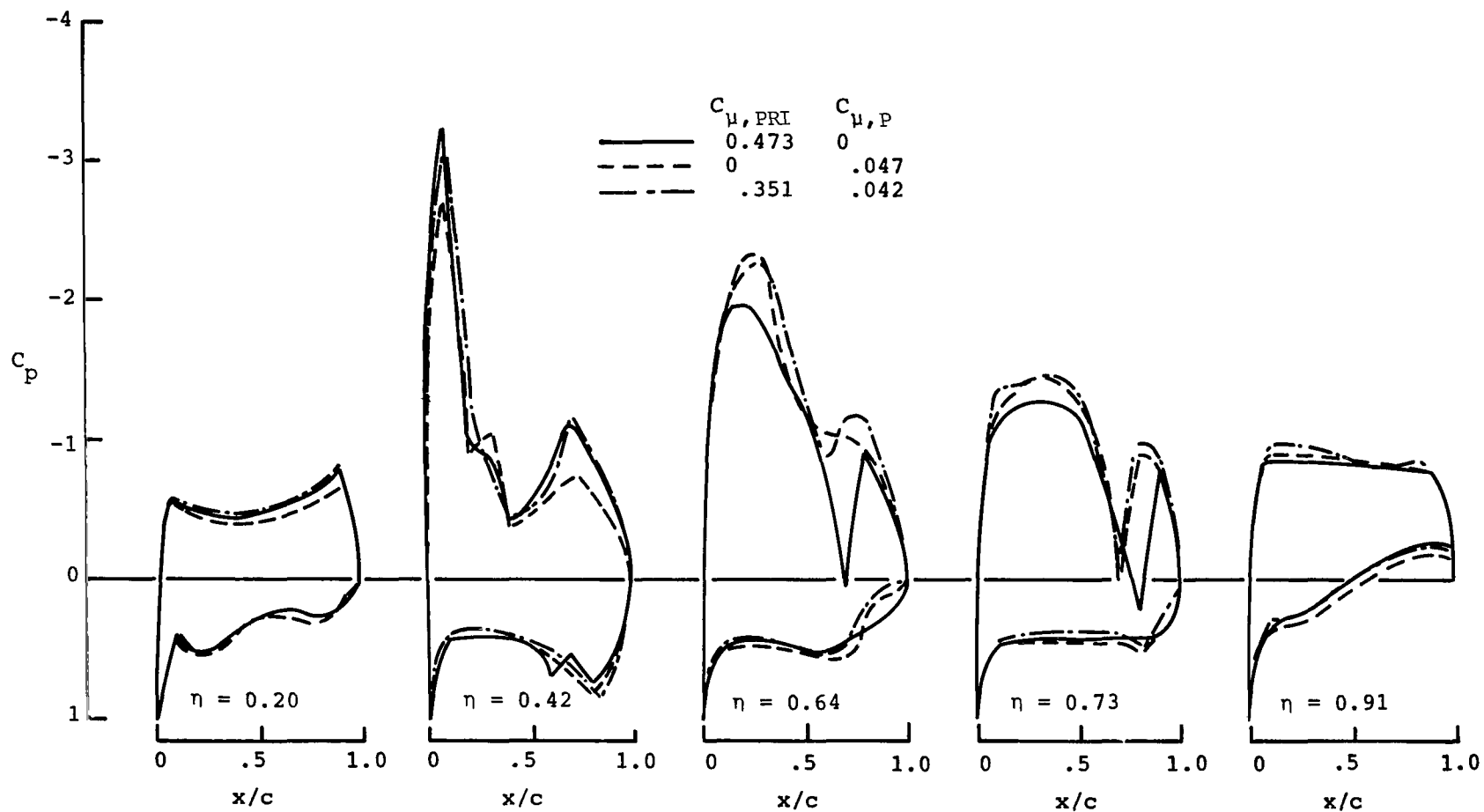
(b) Span-load distribution.

Figure 38.- Concluded.



L-83-146

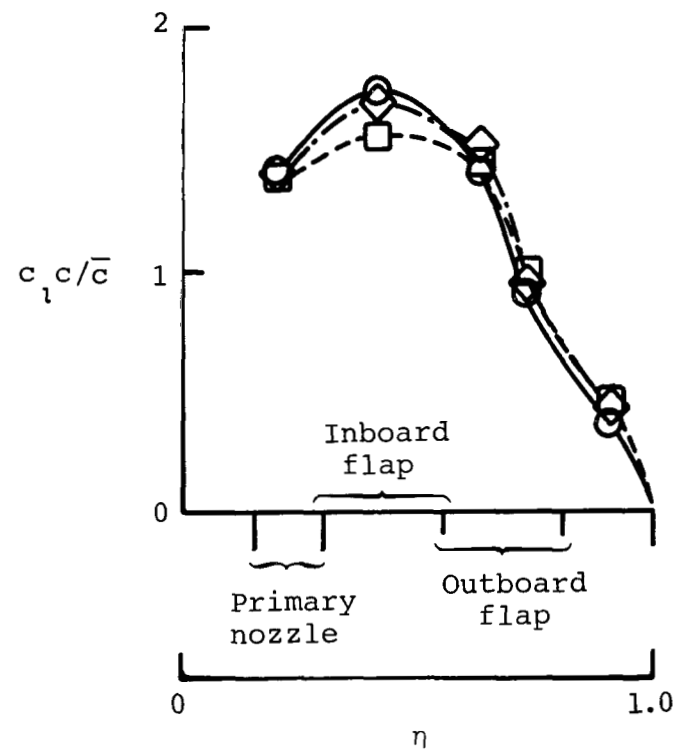
Figure 39.- Wing undersurface oil-flow photograph. Cascade 9; $\delta_f = 45^\circ/26^\circ$.



(a) Surface pressures.

Figure 40.- Effect of thrust of primary nozzle and port 5 on wing surface pressures and span-load distribution.
 $\alpha = 14^\circ$; $\delta_f = 45^\circ/45^\circ$; $\delta_{PRI} = 45^\circ$.

	$C_{\mu, PRI}$	$C_{\mu, P}$
—○—	0.473	0
- - -□-	0	.047
- · -◇-	.351	.042



(b) Span-load distribution.

Figure 40.- Concluded.

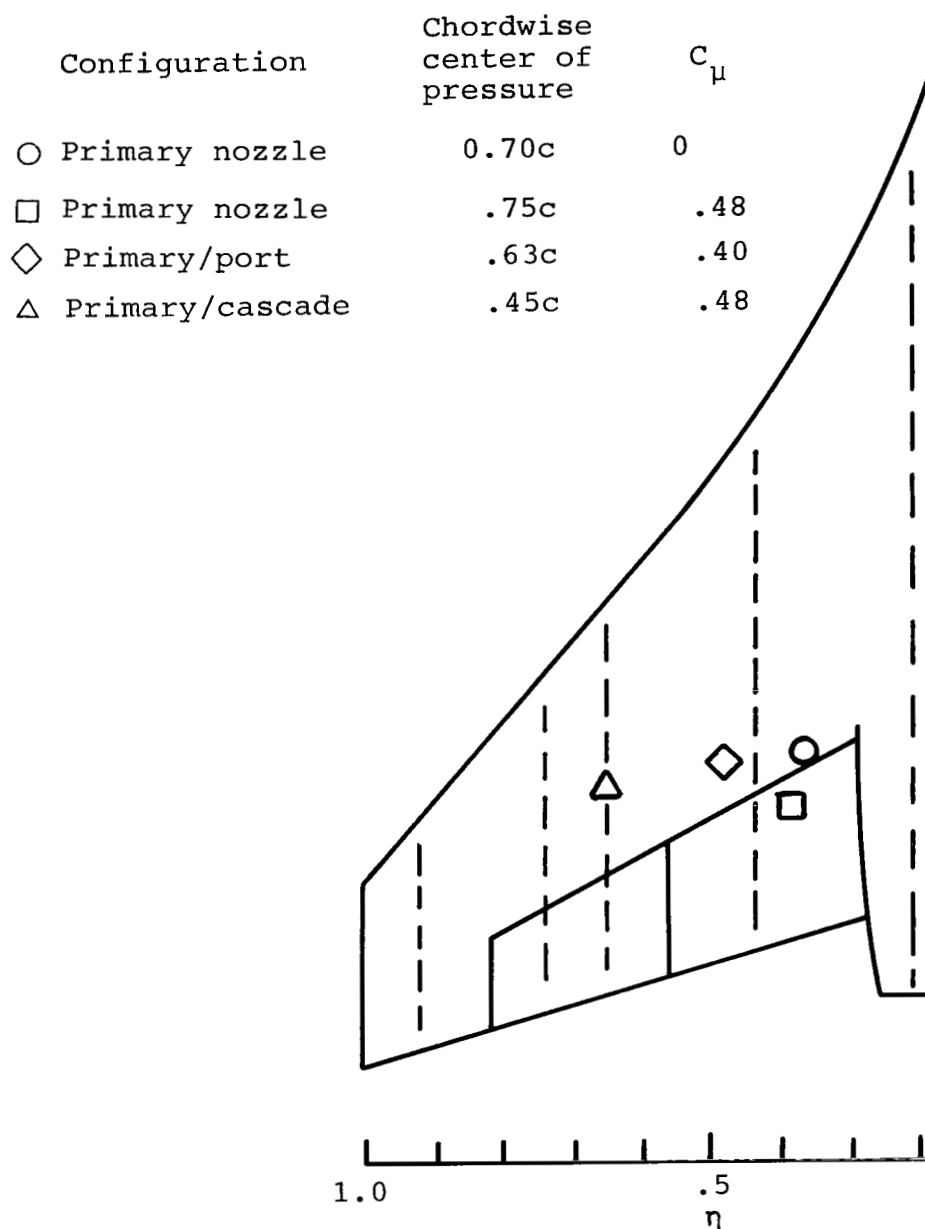
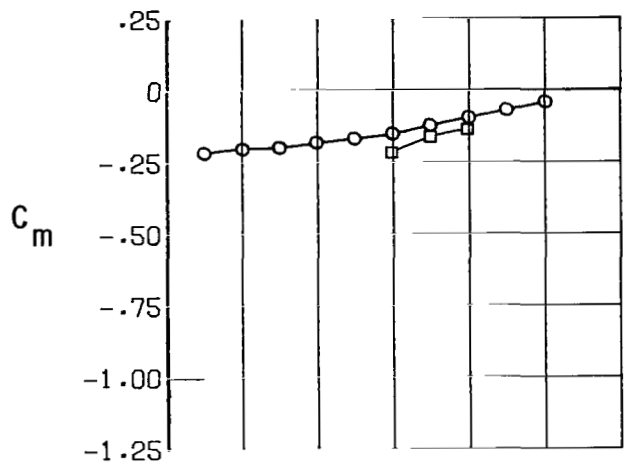
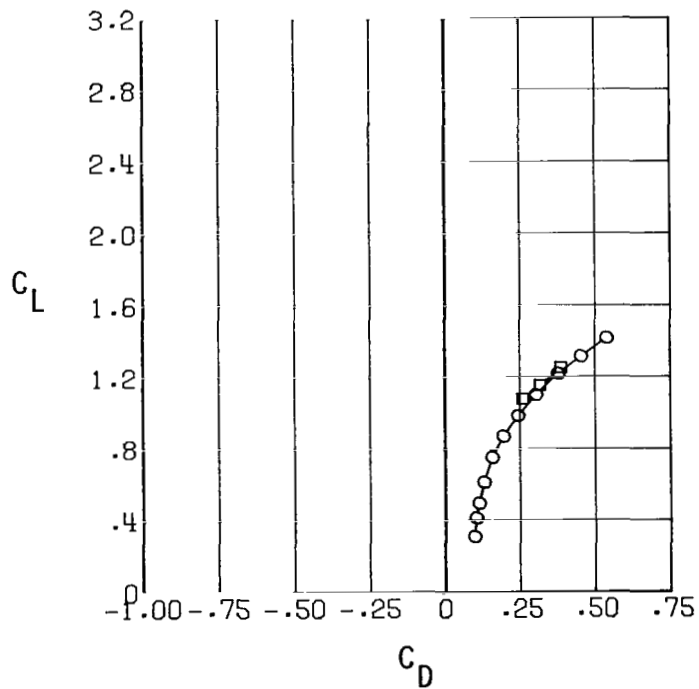
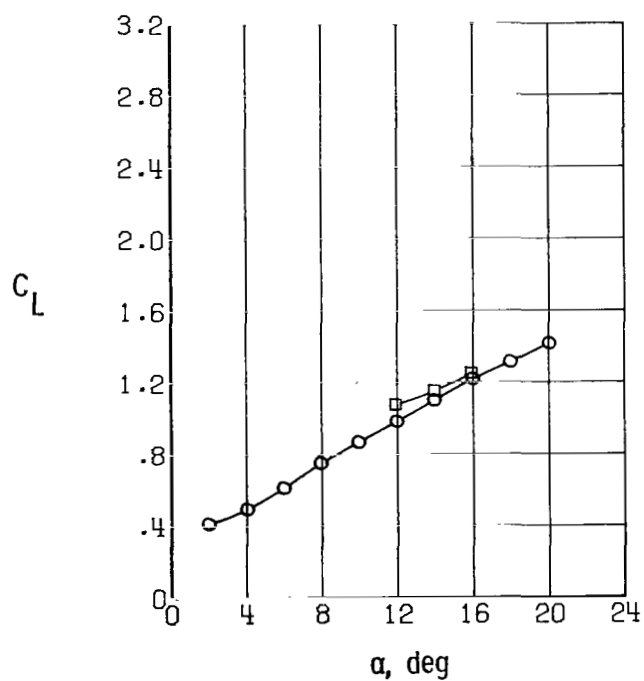


Figure 41.- Center of pressure location on wing semispan for each nozzle configuration. $\alpha = 14^\circ$; $\delta_f = 45^\circ/45^\circ$; $\delta_{PRI} = 45^\circ$.

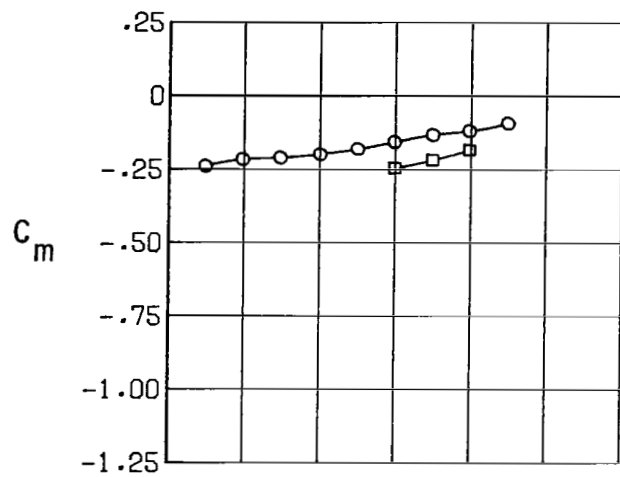


Slot
 ○ Open
 □ Closed

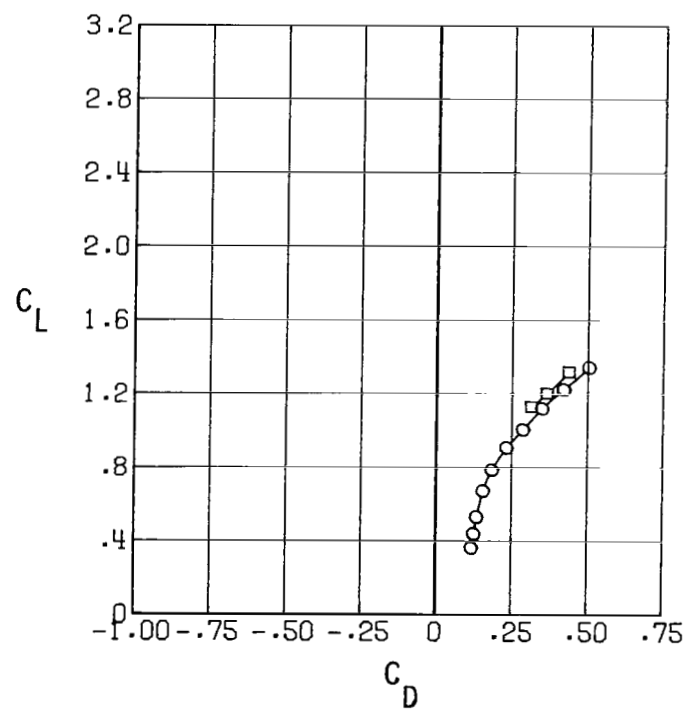
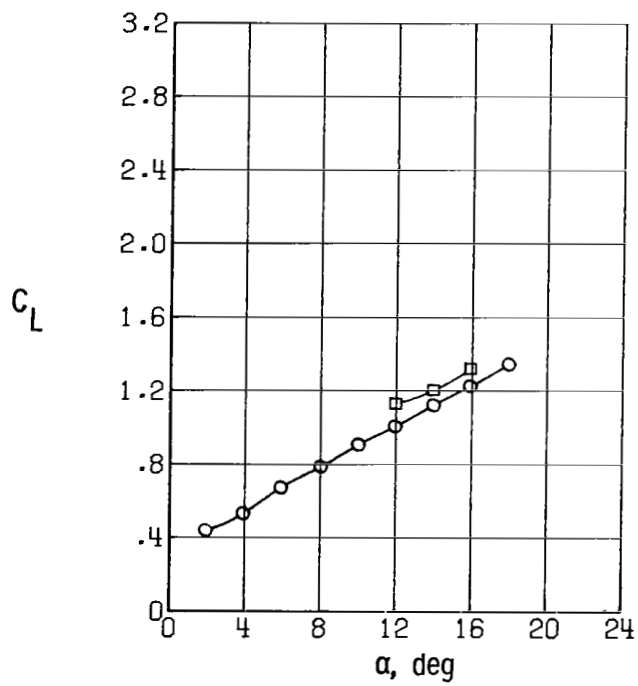


(a) $\delta_f = 45^\circ/26^\circ$; $C_\mu = 0$.

Figure 42.- Effect of slotted flap on longitudinal aerodynamics and induced lift with $\delta_f = 45^\circ/26^\circ$ and $45^\circ/45^\circ$.

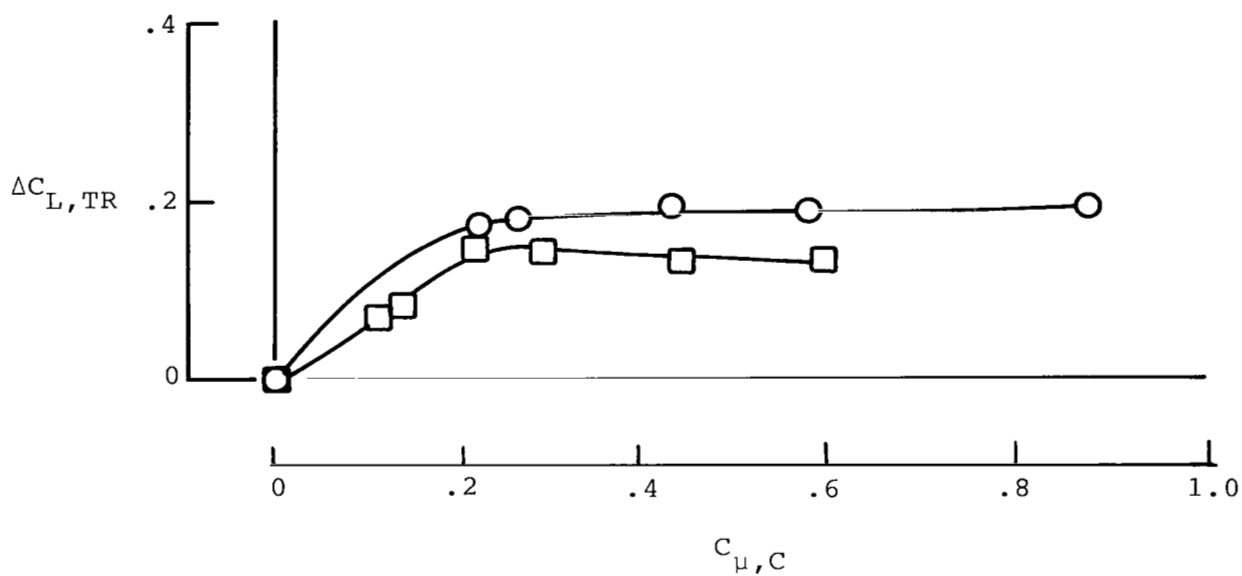


Slot
 ○ Open
 □ Closed

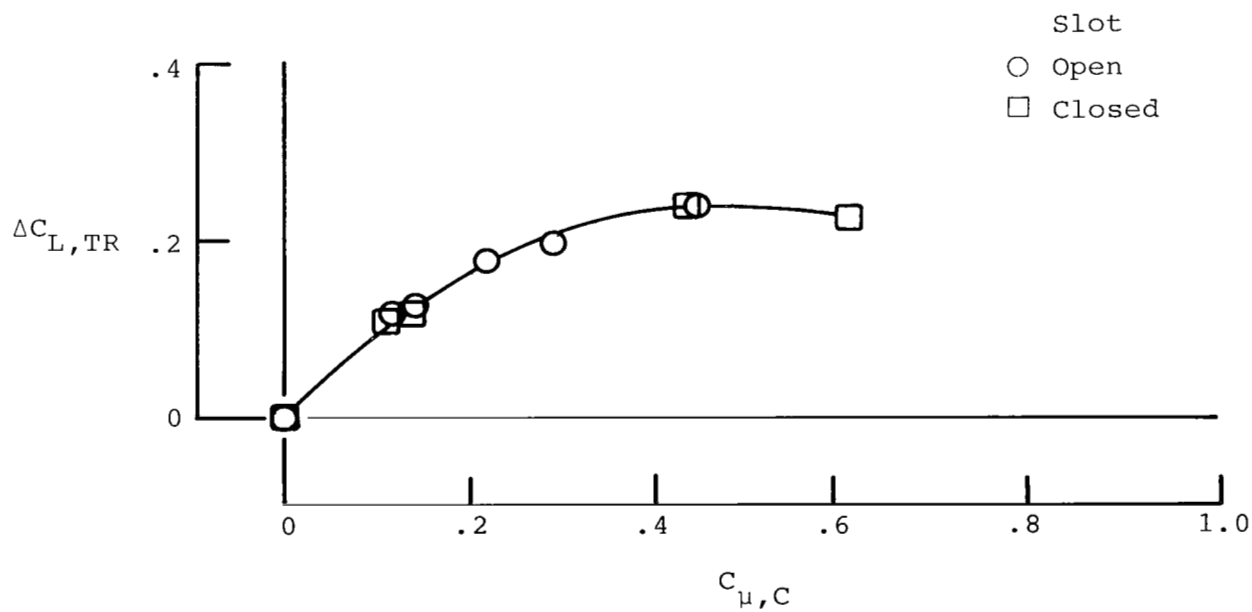


(b) $\delta_f = 45^\circ/45^\circ$; $C_\mu = 0$.

Figure 42.- Concluded.

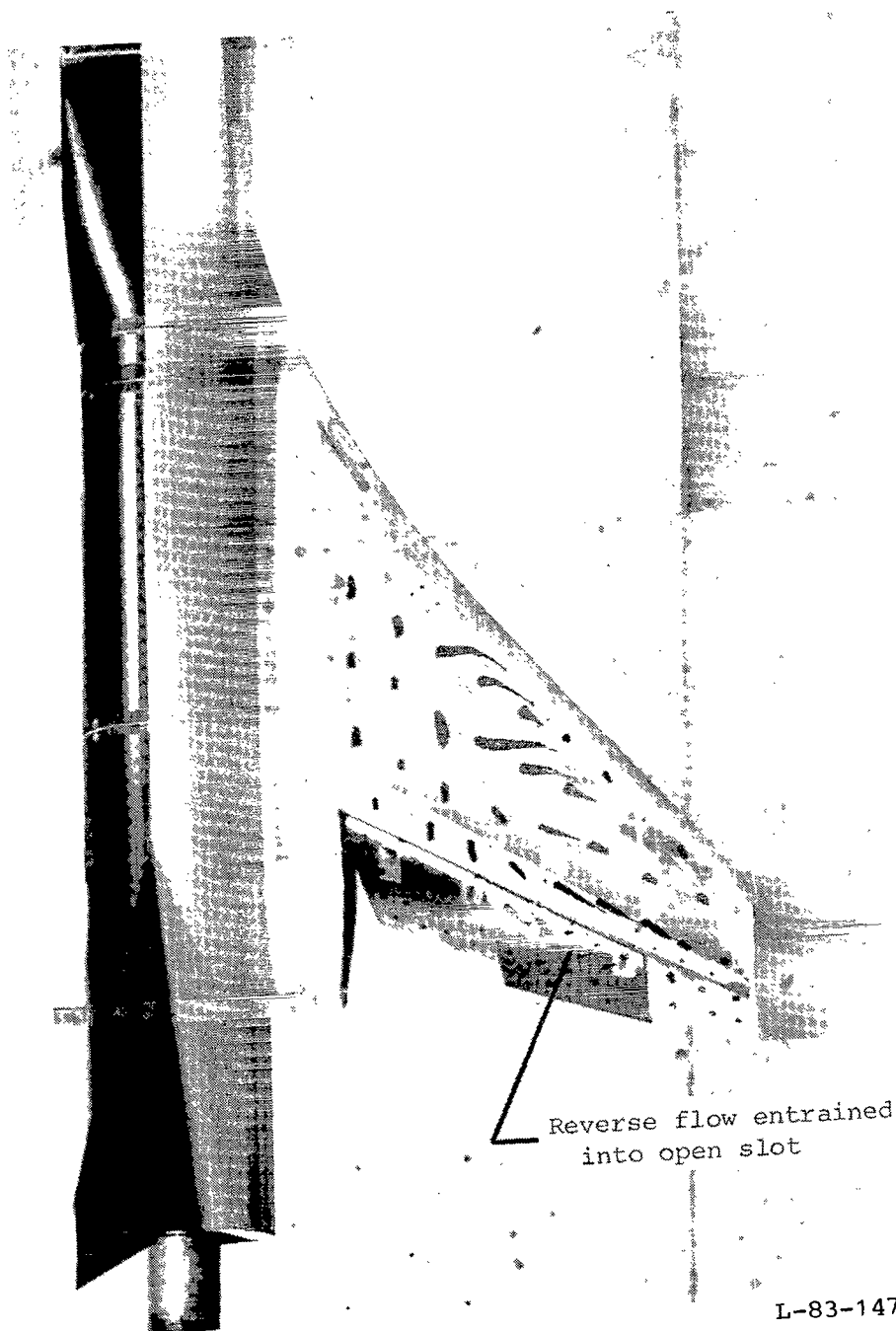


(a) $\delta_f = 45^\circ/26^\circ$.



(b) $\delta_f = 45^\circ/45^\circ$.

Figure 43.- Effect of slotted flap on induced lift. Cascade 9; $C_{\mu,PR1} = 0$.



Reverse flow entrained
into open slot

L-83-147

Figure 44.- Wing upper-surface oil-flow photograph with cascade 9 alone. $\delta_f = 45^\circ/26^\circ$; $C_{\mu,C} = 0.2$.

1. Report No. NASA TP-2250		2. Government Accession No.		3. Recipient's Catalog No.	
4. Title and Subtitle INVESTIGATION OF TRAILING-EDGE-FLAP SPANWISE-BLOWING CONCEPTS ON AN ADVANCED FIGHTER CONFIGURATION				5. Report Date March 1984	
7. Author(s) John W. Paulson, Jr., P. Frank Quinto, and Daniel W. Banks				6. Performing Organization Code 505-43-23-04	
9. Performing Organization Name and Address NASA Langley Research Center Hampton, VA 23665				8. Performing Organization Report No. L-15627	
12. Sponsoring Agency Name and Address National Aeronautics and Space Administration Washington, DC 20546				10. Work Unit No.	
15. Supplementary Notes				11. Contract or Grant No.	
16. Abstract An investigation was conducted in the Langley 4- by 7-Meter Tunnel to determine the aerodynamic effects of spanwise blowing on the trailing-edge flap of an advanced fighter-aircraft configuration. A series of tests were conducted with variations in spanwise-blowing vector angle, nozzle exit area, nozzle location, thrust coefficient, and flap deflection in order to determine a superior configuration for both an underwing cascade concept and an overwing port concept. This screening phase of the testing was conducted at a nominal-approach angle of attack from 12° to 16°; and then the superior configurations were tested over a more complete angle-of-attack range from 0° to 20° at tunnel free-stream dynamic pressures from 20 to 40 lbf/ft ² at thrust coefficients from 0 to 2.				13. Type of Report and Period Covered Technical Paper	
17. Key Words (Suggested by Author(s)) Trailing-edge spanwise blowing Induced aerodynamics Advanced fighter aircraft Port nozzles Cascade nozzles				14. Sponsoring Agency Code	
18. Distribution Statement Unclassified - Unlimited Subject Category 02					
19. Security Classif. (of this report) Unclassified	20. Security Classif. (of this page) Unclassified	21. No. of Pages 105	22. Price A06		

National Aeronautics and
Space Administration

Washington, D.C.
20546

Official Business

Penalty for Private Use, \$300

THIRD-CLASS BULK RATE

Postage and Fees Paid
National Aeronautics and
Space Administration
NASA-451



S

1 1 10, A, 840222 S00903DS
DEPT OF THE AIR FORCE
AF WEAPONS LABORATORY
ATTN: TECHNICAL LIBRARY (SUL)
KIRTLAND AFB NM 87117

NASA

POSTMASTER:

If Undeliverable (Section 158
Postal Manual) Do Not Return